P-194

NASA Contractor Report 179518

Analysis of Mixed-Mode Crack Propagation Using the Boundary Integral Method

Alexander Mendelson and Louis J. Ghosn
Case Western Reserve University
Cleveland, Ohio

September 1986

Prepared for
Lewis Research Center
Under Grant NAG3-396

National Aeronautics and
Space Administration

TABLE OF CONTENTS

CHAPTER ONE

INTRODUCTION

The problem of failure in rolling and sliding contacts goes back to the period when roller bearings, gear, and railroad wheels were first used. Even though many failure modes had been analyzed and empirical rules were formulated to guide designers against these failures, a new catastrophic failure for bearings was recently detected in test rigs for high speed engines. This failure mode can be described as a fast growing crack that initiates from the surface of an inner raceway of a high speed bearing. Fig. 1.1 shows a typical split ring ball bearing used in such high speed tests. This type of failure was encountered at DN values of three million (where D is the bearing bore in millimeters and N is the shaft speed in RPM). These high DN values are needed to meet the future requirements of high performance aircraft engines. This research investigates this failure mode using fracture mechanics theories and numerical stress analysis techniques.

1.1 Failure in Bearings

Rolling contact devices such as rolling bearings may have various causes for failure. The most common causes are plastic

ORIGINAL PAGE IS
OF POOR QUALITY

Fig. 1.1 Typical High Speed Bearing for Aircraft Engine Support, Ref. [51]

indentation, heat imbalance, wear and rolling contact fatigue, see Ref. [1].

Plastic Indentation :

The raceway under a rolling or even under a stationary contact undergoes plastic deformation when solid debris is caught in the contact region or when the system is overloaded. This case produces surface defects that can initiate a fatigue crack failure. Fig. 1.2.a shows some typical plastic indentations grooves on inner raceway of bearings.

Heat Imbalance :

Since all loaded moving contacts generate heat, and on some occasion heat is brought into a bearing from the outside, this can evaporate the lubricant and soften the contact material, which can lead to the gross failure of the bearing. Thermal energy must be removed by cooling the bearing to avoid excessive temperatures.

Wear :

All machined surfaces have asperities that are large compared with molecular dimensions. When two surfaces slide over each other, the softer asperities either fracture or deform. The rate at which these asperities are removed is known as the wear rate which usually depend on the initial surface roughness, the

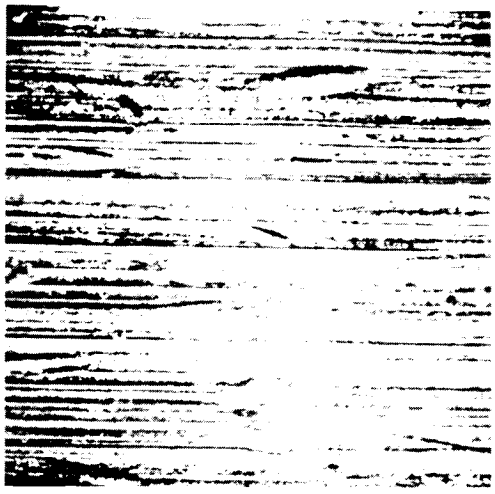

a) Plastic Indentation

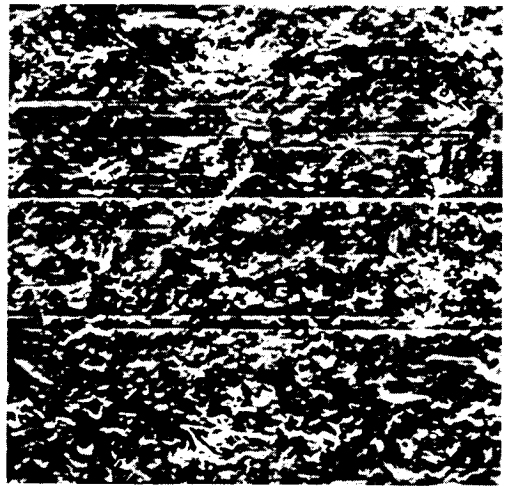

b) Wear

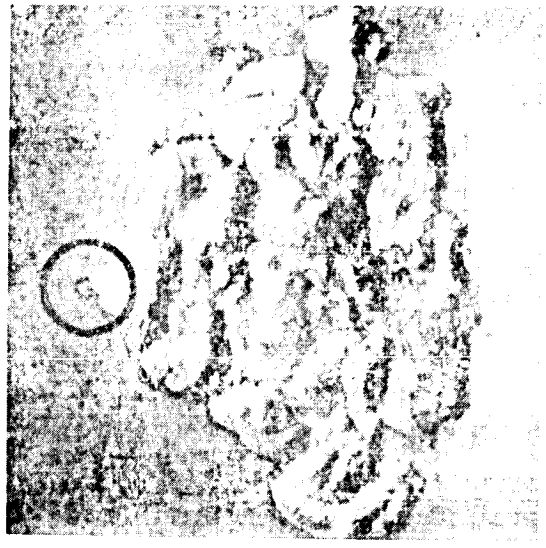

c) Contact Fatigue

Fig. 1.2 Typical Surface Defects

applied load, the lubricant and the mechanical properties of the asperities. Typical surface wear is seen in Fig. 1.2.b.

Contact Fatigue (Spalling) :

It is well known that many metals, among them steel, some non-metals (ceramics) react to repeated application of the same load by gradually building up a fatigue crack. In this failure mode a small crack forms in the subsurface, normally associated with stress raiser such as void, non-metallic inclusion, or carbide. The crack after repeated loading propagates outward to form a spall. But with advances in bearing materials and processing techniques, subsurface initiated fatigue is rarely encountered. Instead a surface initiated fatigue spalling is more likely, where a small crack develops from a debris dent or an oxidation pit and propagates inward. These cracks that originate at the surface propagate at an acute angle toward the bore of the raceway until they meet deformation bands. Here they are diverted back toward the surface in the direction the ball travels forming a spall. In Fig. 1.2.c, a typical spall, which was initiated around a surface furrow is shown.

While spalling is undesirable, it is a relatively gradual fatigue process that can be detected by vibration monitors, chip detectors and other oil system monitors. Consequenly the affected components can usually be removed before more serious secondary damage is incurred. However, at increased rotational

speed, (a high DN value), rapid fracture occurs prior to significant spalling, and consequently no warning is received before the complete failure of the bearing, causing extensive damage to the engine. At high DN values, a crack will develop from the surface defect of the inner raceway and propagate inward at a rate higher than the spalling rate and to a greater depth than regular spalling, causing a catastrophic failure.

1.2 Literature Review

A large number of investigations have been carried out to clarify the mechanism of rolling contact fatigue. However, contradiction still persist on the driving force that causes a contact fatigue crack.

From the metallurgical viewpoint it may be considered that the process of fatigue consists of two stages; crack initiation and crack propagation. The propagation stage has been explained so far by two different mechanism. The first mechanism takes into consideration the pressure of the lubricant seepage into the crack. This mechanism is based on experiments presented by Way in 1935, Ref. [2], where he demonstrated that lubricants must be present if fatigue crack propagation is to take place. The second mechanism is just due to surface traction, where no lubricant is present. Fleming and Suh, Ref. [3], were the first to analyze crack propagation in sliding contact, under an

asperity contact. The tangential hoop stresses due to the centrifugal load were completely ignored. Linear fracture mechanics was applied using approximate solution for the stress intensity factors. Recently, Rosenfield [4] did the same analysis with an added feature. He included in his model the effect of the friction on the two crack faces under shear, due to the high compressive normal stresses. Keer and his coworkers , [5] [6] [7], analysed the surface crack as well as the subsurface crack, under general Hertzian loadings. They also determined the crack propagation angles using the maximum tangential stress around the crack tip. They determined that the edge crack will most likelly grow in a direction of -69 degrees from the horizental. In a preceding paper, [6], Keer added extra features in modelling the crack propagation of an edge crack inclined at 65 degrees from the horizontal. In that analysis, the friction effect for the cracked faces and the lubricant effect were included. A uniform pressure on the open part of the crack faces was applied to model the lubricant effect. The variations of the stress intensity factors and the angles of maximum tangential stresses were described in great detail. But, the investigation was not carried further to see what will happen to the angle of propagation after the first kink (i.e. crack tip change in direction of propagation). All the above investigations were based on a two dimensional model of a semi infinite region, and not until Murakami et al., Ref. [8] was a three dimensional model

presented. The friction effect on the crack surfaces was ignored. It was determined that fatigue crack propagation is accelerated predominatly by the hydraulic pressure effect, and the direction of crack growth is fixed by the direction of the initial crack formed.

Not until recently were the hoop stresses due to rotational speed taken into consideration in the fatigue crack growth. Clark, Ref. [9], was the first to suggest that at high rotational speed the driving force for crack propagation is the alternating mode I stress intensity factor, due to the significant tensile hoop stresses. He qualitatively stated that the superposition of the Hertzian stress field upon the tensile hoop stress field causes an alternating mode I stress intensity factor which leads to a rapid crack growth in the raceway. He basically ignored the high alternating shear stresses introduced by the Hertzian loading as the roller passes from one side of the crack to the other.

Experimental investigations on the endurance and failure characteristic of high speed bearings at three million DN values were performed by Bamberger, Zaretsky and Signer, [10]. Groups of 30, 120 mm bore ball bearings, made of M50 high speed steel, were endurance tested at two speeds (12,000 and 25,000 RPM) corredponding to 1.44×10^6 and 3.00×10^6 DN, respectivally. Initial bearing failure at 12,000 RPM was by classical surface rolling element fatigue of the inner race. However, continuous running

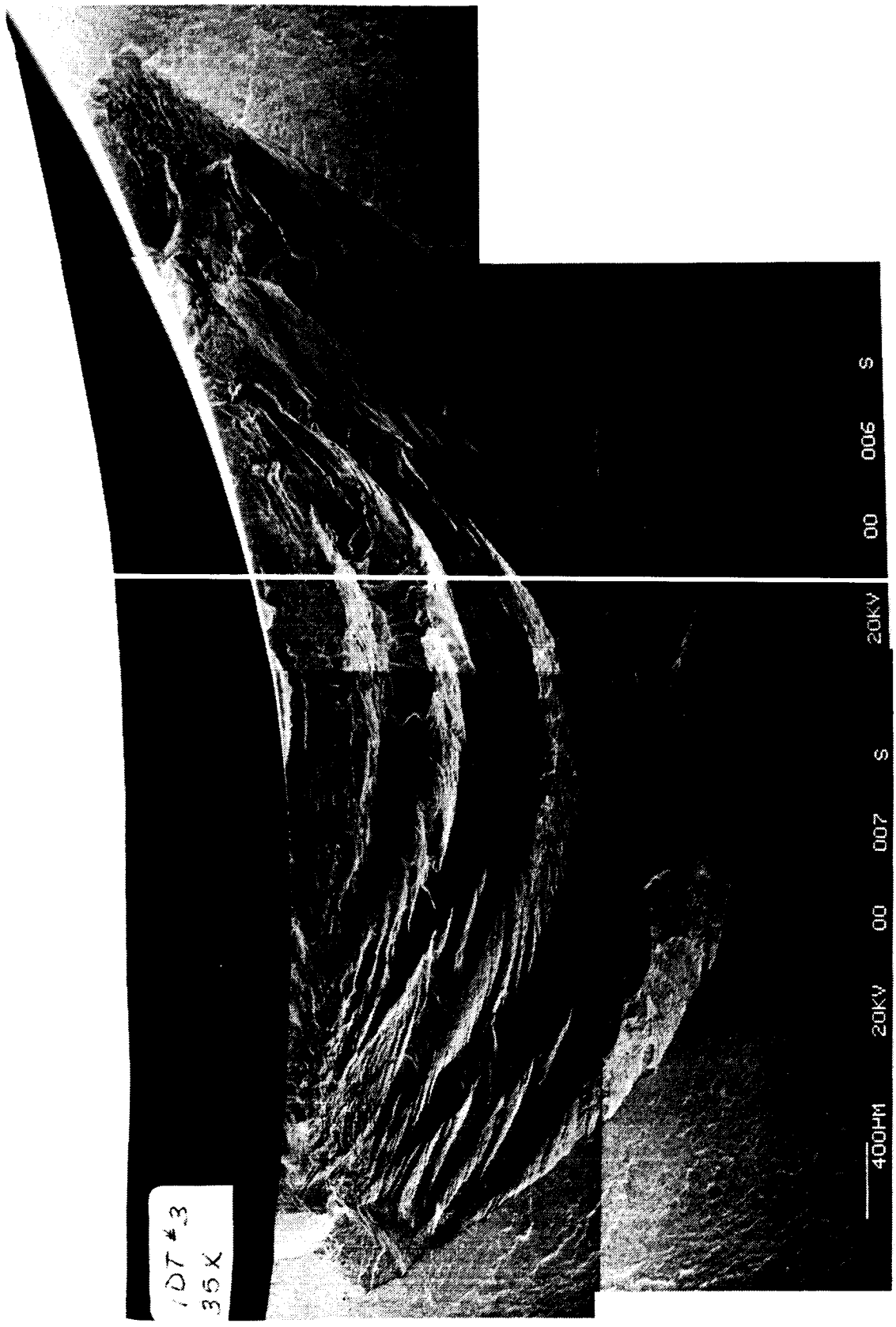

Fig. 1.3 Typical Step-Like Surface Fracture of a Ball Bearing after Failure for a DN Value of Three Million, Ref. [51]

after a small surface crack had occurred at $3.0X10^6$ DN resulted in a destructive fracture of the bearing because of the high hoop stresses present due to centrifugal forces. Closer investigation of the fracture surfaces showed that the fracture had several distinct steps. The initial fracture was normal to the surface until it reached the first plateau where it changed direction and propagated parallel to the surface in the direction of the ball travel. It then, once more, changed direction and propagated radially inward until it changed direction for the third time. This pattern was observed on several bearings tested, Fig. 1.3. This experimental evidence basically contradicts the earlier conclusions of Murakami assuming that the crack growth direction is fixed by the initial crack direction.

With the above experimental evidence, one is forced to analyze the fatigue crack propagation under the combined tangential hoop stress due to rotation and the Hertzian load that introduces a high alternating shear stresses, as well as high compressive stresses as the roller crosses the crack plane. This loading condition introduces a complex stress state that leads to a mixed mode stress intensity factor. But very little information on mixed-mode fatigue crack growth under mixed loading conditions is available. The early research on the crack propagation direction and time to failure was confined to one dimensional loadings. In 1980, Sih, Ref. [11], proposed an expression for the mixed mode fatigue according to his strain

energy density factor theory:

$$\Delta S_{min} = 2(a_{11}\bar{K}_I\Delta K_I + a_{12}(\bar{K}_I\Delta K_{II} + \bar{K}_{II}\Delta K_I) + a_{22}\bar{K}_{II}\Delta K_{II})$$

$$\frac{\Delta a}{\Delta N} = C\,(\Delta S_{min})^n$$

Where a_{ij} = functions of the angle , θ

$\bar{K}_j$ = mean stress intensity factor

ΔK_j = stress intensity factor range

C,n = material constants

$\Delta S_{min} = S_{min}^{max} - S_{min}^{min}$

S_{min}^{max} = Maximum Strain Energy Density Factor

S_{min}^{min} = Minimum Strain Energy Density Factor

in the Direction , θ

S_{min} = Strain Energy Density Factor = r dW/dV

dW/dV= Strain Energy Density

If one considers the crack propagation rate versus the cylic stress intensity factor range in a double logarithmic presentation, three well known regions of crack growth rate are observed, Fig. 1.4, [12]. If the stress intensity range is below the threshold range, ΔK_{th}, crack growth is not observed. In region II, the rate of crack propagation varies linearly with the

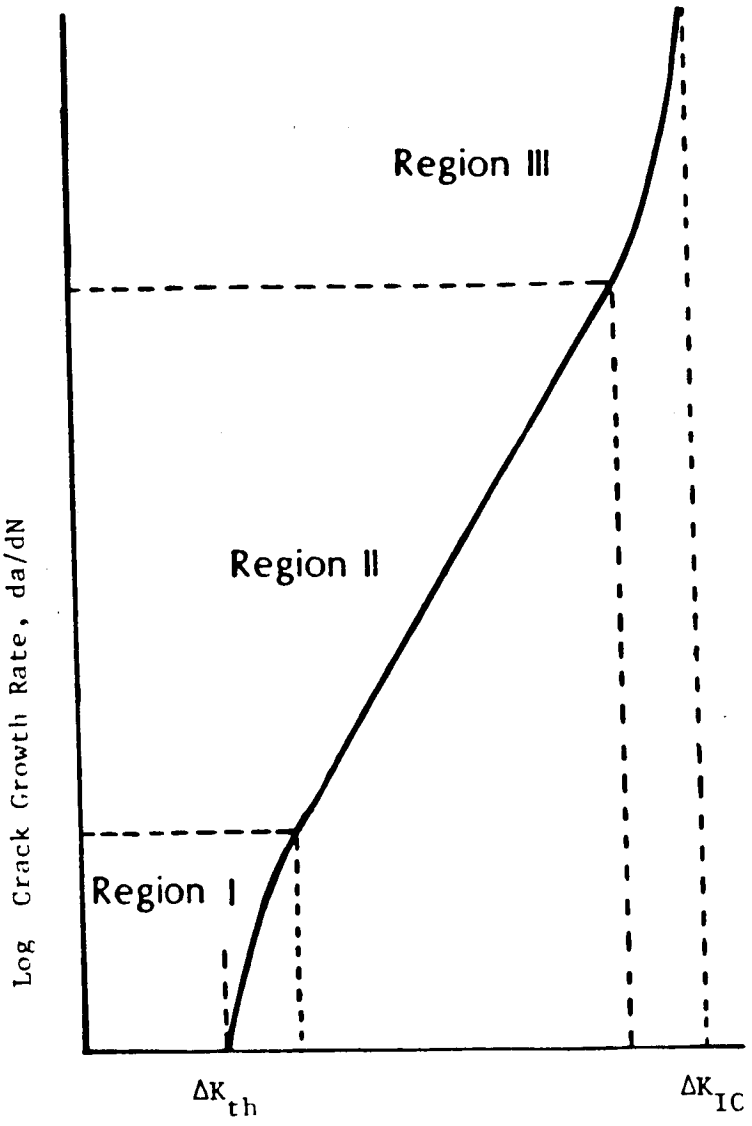

Fig. 1.4 Crack Growth Rate versus Stress Intensity Range

stress intensity range on a logarithmic scale. In region III, the crack growth rate reaches a very high speed since the maximum stress intensity factor is approaching the critical stress intensity factor for unstable crack growth K_{Ic}. The most general analytical equation for mode I fatigue crack growth rate is due to Forman and coworkers [13], where they took into consideration all the ranges of the experimental curve, refer to Fig. 1.4:

$$\frac{da}{dN} = C \frac{[\Delta K_I - \Delta K_{th}]^{n_1}}{[(1-R)K_{IC} - \Delta K_I]^{n_2}}$$

where $R = K_{Imin}/K_{Imax}$

There are only a few papers in the literature dealing with stable crack propagation under mixed loading. One reason is that crack growth in the second region apparently occurs under mode I conditions, (Fisher [12]), and the main regime for mixed mode occurence is region I. This region is the most important for fatigue crack initiation and propagation in rolling contact fatigue. This may explain why Murakami had to include the influence of the lubricant to increase the stress intensity range above the threshold range for mode I.

1.3 Dissertation Outline

The aim of this study is to analyze the causes that lead to the brittle failure of high speed bearings. The object is to

provide bearing designers with the tools necessary to cross this new barrier for future engines operating at DN values of three million and above.

In order to accomplish this aim, the loadings that are significant for the creation of the fast growing cracks should be quantified. Aside from the obvious normal Hertzian load across the contact interfaces, surface parallel forces also arise from friction at the contacts. Also, the centrifugal forces of the inner raceway cannot be ignored since they can play an important role in the propagation of fast cracks.

With the external loading being defined, the stresses in the inner raceway of a bearing will be calculated numerically using the boundary integral equation method (BIEM). The first objective of this research is to describe the interaction between the Hertz stress field and the centrifugal hoop stress in the presence of a surface defect like a pit or a crack in terms of stress intensity factors, K_I and K_{II}. The parameters which determine the stress fields generated by the rolling contact loads are the elastic constants of the bearing materials, the design geometries of the raceway and the roller , the microgeometry of the surface roughness, the film forming parameters of the lubricant, and the geometry of the crack.

The second objective is to determine the crack growth rate and its orientation under this complex loading condition. To accomplish this, the major driving forces for fast growing cracks

should be identified. It is assumed that combined alternating mode I and mode II loadings are behind the step like crack growth observed at 3 million DN value. The alternating mode I (crack faces moving normal to the crack plane) is associated primarily with the oscillation of the high tangential stress due to the centrifugal loads from each passage of a heavily compressive loaded roller. The alternating mode II (crack faces moving parallel to the crack plane) is associated with the change in the direction of the shear stress when the roller moves from one side of the crack to the other.

In Chapter Two, the different mixed-mode crack growth criteria, for static and dynamic loadings, are presented and compared. The crack extension forces are divided into two parts: first the region for shear mode growth governed by the shear crack extension forces, $G_{r\theta}$, second the tensile mode growth region governed by the tangential crack extension forces, $G_{\theta\theta}$. This crack extension criteria will be used in the analysis of the mixed-mode failure of the inner raceway of high speed bearings.

Chapter Three is dedicated to the derivation and the implementation of the boundary integral equation method in fracture mechanics.

In chapter Four, the loadings applied on the inner raceway of a high speed bearing are quantified. The tangential stresses due to the rotational speed and press fit are calculated as a function of the DN value. The Hertzian pressure distribution are

estimated with and without lubrication.

Chapter Five gives the variation of the mixed-mode stress intensity factors as function of the Hertzian load, crack length, and roller position. Crack extension forces along the crack tip are presented as well as the angles of crack propagation, which are determined along the direction of the maximum change of the crack extension forces. Finally, the life to failure of the inner raceway is estimated from crack propagation rate data of M50 bearing steel.

Chapter Six reviews the results and conclusions of the study and outlines needs for future research on the mixed-mode failure in general and the inner raceway of high speed bearings in particular.

CHAPTER TWO

MIXED-MODE CRACK GROWTH

The bulk of fracture mechanics work to date has been concerned with single-mode loading. Many practical situations are mixed-mode, but pure mode I loading is usually assumed in order to obtain easy solutions. This assumption often leads to unsafe design. Conversely, neglecting the effects of mixed-modes may lead the designer to be over-conservative in an attempt to compensate for his lack of knowledge. In this chapter different mixed-mode crack growth criteria will be presented and compared and the appropriate analysis will be used for the crack propagation studies of the inner raceway of the high speed engine bearings.

2.1 Linear Elastic Fracture Mechanics

Linear elastic fracture mechanics theory is based on an analytical procedure that relates the stress and displacement fields in the vicinity of a crack tip to the applied load, to the structure, to the size, shape and orientation of the crack, and to material properties. To determine the stress and displacement fields in a cracked body, it is important to define the three basic modes of crack-surface displacements, see Fig. 2.1. Mode

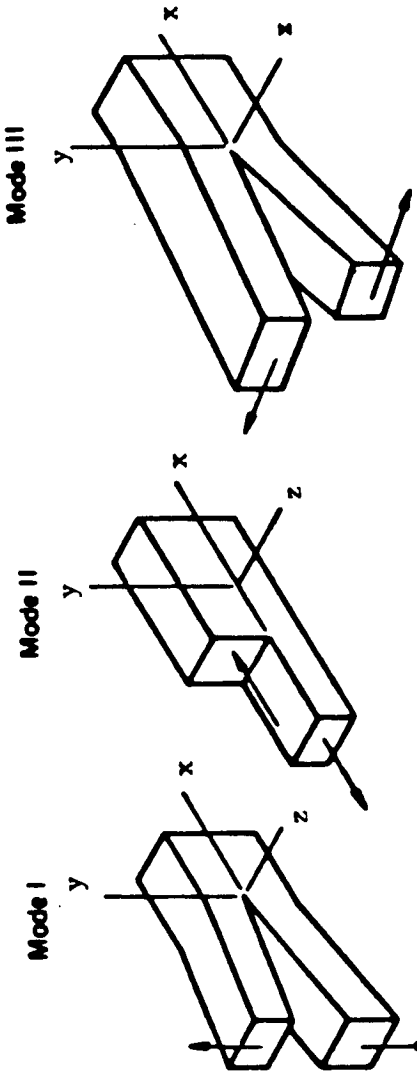

Fig. 2.1 The Basic Loading Modes

I, opening mode, corresponds to normal separation of the crack surfaces under the action of the remote applied tensile stresses. Mode II, in-plane sliding mode, corresponds to the crack faces moving parallel to the crack plane and normal to the crack bottom. Mode III, tearing mode is the out-of-plane shear mode. Of the three modes, mode I is technically the most important to crack propagation in brittle solids, and has the largest fracture tests reported on it for different materials. In this investigation, the mixed-mode fracture considered is a result of mode I and mode II. This is an in-plane loading condition, and the out-of-plane loading, mode III, will be ignored.

The stress and displacement fields for a semi-infinite region containing a sharp crack, as given in Ref. [14], have the following forms, see Fig. 2.2:

Mode I:

$$\begin{bmatrix} \sigma_{rr} \\ \sigma_{\theta\theta} \\ \sigma_{r\theta} \end{bmatrix} = \frac{K_I}{(2\pi r)^{\frac{1}{2}}} \begin{bmatrix} \cos\frac{\theta}{2}\left(1+\sin^2\frac{\theta}{2}\right) \\ \cos^3\frac{\theta}{2} \\ \sin\frac{\theta}{2}\cos^2\frac{\theta}{2} \end{bmatrix} \qquad 2.1\text{-a}$$

$$\begin{bmatrix} u_r \\ \\ u_\theta \end{bmatrix} = \frac{K_I}{2E}\left(\frac{r}{2\pi}\right)^{\frac{1}{2}} \begin{bmatrix} (1+\nu)\left((2\kappa-1)\cos\frac{\theta}{2} - \cos\frac{3}{2}\theta\right) \\ \\ (1+\nu)\left(-(2\kappa+1)\sin\frac{\theta}{2} + \sin\frac{3}{2}\theta\right) \end{bmatrix} \qquad 2.1.b$$

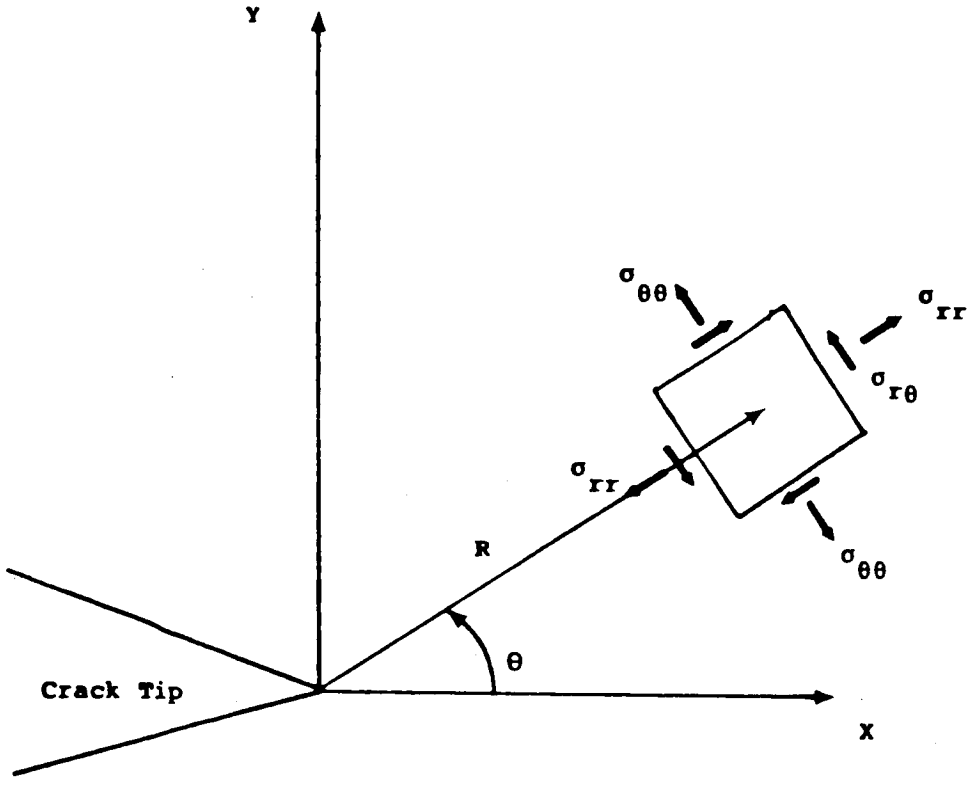

Fig. 2.2 Polar Coordinates and Stress Element with respect to the crack tip.

Mode II:

$$\begin{bmatrix} \sigma_{rr} \\ \sigma_{\theta\theta} \\ \sigma_{r\theta} \end{bmatrix} = \frac{K_{II}}{(2\pi r)^{\frac{1}{2}}} \begin{bmatrix} \sin\frac{\theta}{2}(1-3\sin^2\frac{\theta}{2}) \\ -3\sin\frac{\theta}{2}\cos^2\frac{\theta}{2} \\ \cos\frac{\theta}{2}(1-3\sin^2\frac{\theta}{2}) \end{bmatrix} \qquad 2.2.a$$

$$\begin{bmatrix} u_r \\ u_\theta \end{bmatrix} = \frac{K_{II}}{2E}\left(\frac{r}{2\pi}\right)^{\frac{1}{2}} \begin{bmatrix} (1+\nu)(-(2\kappa-1)\sin\frac{\theta}{2} + 3\sin\frac{3}{2}\theta) \\ (1+\nu)(-(2\kappa+1)\cos\frac{\theta}{2} + 3\cos\frac{3}{2}\theta) \end{bmatrix} \qquad 2.2.b$$

Where E is young's modulus, ν is poisson' s ratio, and

$\kappa = (3-\nu)/(1+\nu)$ for plane stress

$\kappa = (3-4\nu)$ for plane strain

K_I and K_{II} are defined as the stress intensity factors, for mode I and mode II loadings respectively.

The above field equations show that the stress and displacement fields in the vicinity of the crack tip are functions only of the stress intensity factors and material properties. Consequently, the stress intensity factors are parameters that represent a measure of the applied stress, crack

shape and size, and structural geometry. One should be made aware that the above solutions are valid only for small distances from the crack tip. For larger distances from the crack tip higher order terms should be included to match the outer boundary conditions.

Since the principle of superposition applies to linear stress and displacement fields, Eq. 2.1 and 2.2 are added together to determine the mixed-mode stress and displacement fields.

As seen from the above stress fields, the stresses tend to infinity as r goes to zero, but the tangential stress and the shear stress multiplied by the square root of r go to constant values K_I and K_{II}, respectively, for $\theta = 0$:

$$\lim_{r \to 0} \sigma_{\theta\theta} \sqrt{2\pi r} = K_I$$

$$\lim_{r \to 0} \sigma_{r\theta} \sqrt{2\pi r} = K_{II} \qquad 2.3$$

As a result the stress intensity factors are measures of the intensity of the elastic stress fields ahead of the crack tip. Therefore, the stress intensity factors, K_I and K_{II}, quantify the intensity of the stresses for brittle materials, such as the high strength steel used in bearings, under mixed-mode loading conditions.

2.2 Crack Extension Force

The crack extension force, also known as the "Energy Release Rate", G, is basically derived from the change in the work of external loads and the strain energy as the crack grows by an amount da, see Fig. 2.3.

$$G = d\,(-U_E + W_L)\,/\,d\,a \qquad 2.4$$

where U_E is the elastic energy and W_L is the work performed by the external forces. This definition is based on the Griffith Energy criterion for fracture.

The above criterion assumes self-similar crack growth, the crack extends in the same direction as the main crack. For mixed-mode loadings, the possibility for the crack to change direction is more likely, as seen in most mixed-mode experiments [18], [19]. Therefore, the formulation for crack extension under mixed-mode loadings, should be able to measure the crack extension force at any angle θ around the crack tip. An alternative definition is shown next based on the mechanical energy required to close a small crack tip extension along an angle θ measured from the original direction of the main crack.

The crack extension force, G, can be derived from the energy required to open an increment CC' of the crack tip, see Fig. 2.4. This definition is taken from Ref. [14] for a self-similar crack,

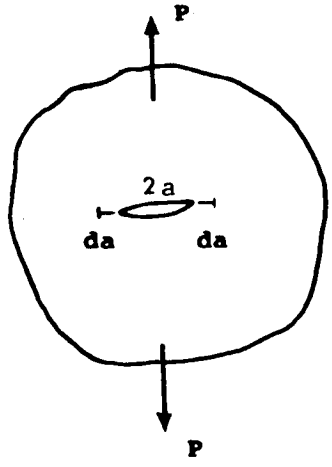

Fig. 2.3 Body with Incremental Crack Extension da.

but here it is extended for any kinked crack, to account for the possibility that the crack can change direction under mixed-mode conditions. The crack extension force is equal to the work that would be done by the forces along CC' to close the crack increment along any angle θ.

Therefore:

$$G = \lim_{\delta \to 0} 2/\delta \int_0^{\delta} \tfrac{1}{2}\{(\sigma_{\theta\theta}(r)\ u\ (\delta-r)+\sigma_{r\theta}(r)\ u_r(\delta-r)\}\ dr \qquad 2.5$$

The 2 is necessary because of the upper and lower surfaces. The 1/2 accounts for the proportionality between tractions and displacements. In this equation only mode I and mode II are considered; mode III can be easily added as $1/2\ \sigma_{z\theta}\ u_z$. The relevant stresses to be considered from Eq. 2.1.a and 2.2.a, are those across CC' prior to crack extension but in opposite direction since a negative force is required to close the crack extension CC'.

$$\sigma_{\theta\theta} = -\frac{K_I}{(2\pi r)^{\frac{1}{2}}} \cos^3\frac{\theta}{2} + \frac{K_{II}}{(2\pi r)^{\frac{1}{2}}} 3 \sin\frac{\theta}{2}\cos^2\frac{\theta}{2}$$

$$\sigma_{r\theta} = -\frac{K_I}{(2\pi r)^{\frac{1}{2}}} \sin\frac{\theta}{2}\cos^2\frac{\theta}{2} - \frac{K_{II}}{(2\pi r)^{\frac{1}{2}}} \cos\frac{\theta}{2}\left(1-3\sin^2\frac{\theta}{2}\right) \qquad 2.6$$

The displacements are those across C'C prior to crack closure and are based on the new geometry of the crack. As an

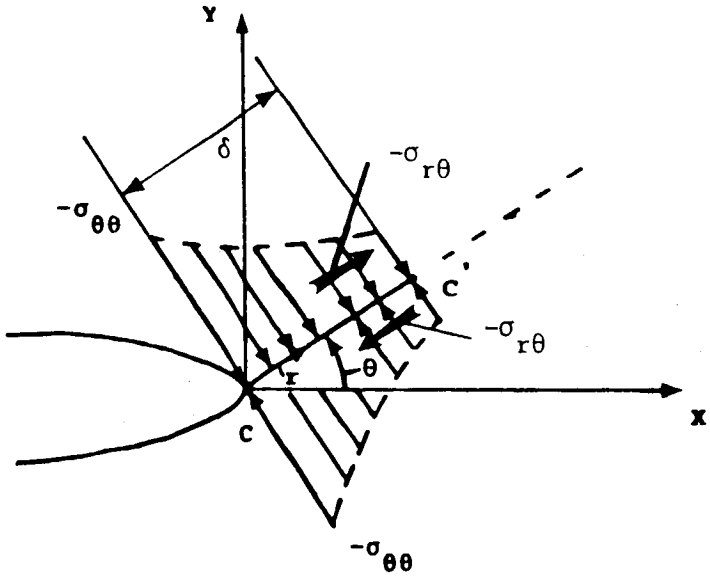

a) Load needed to close a crack extension CC'

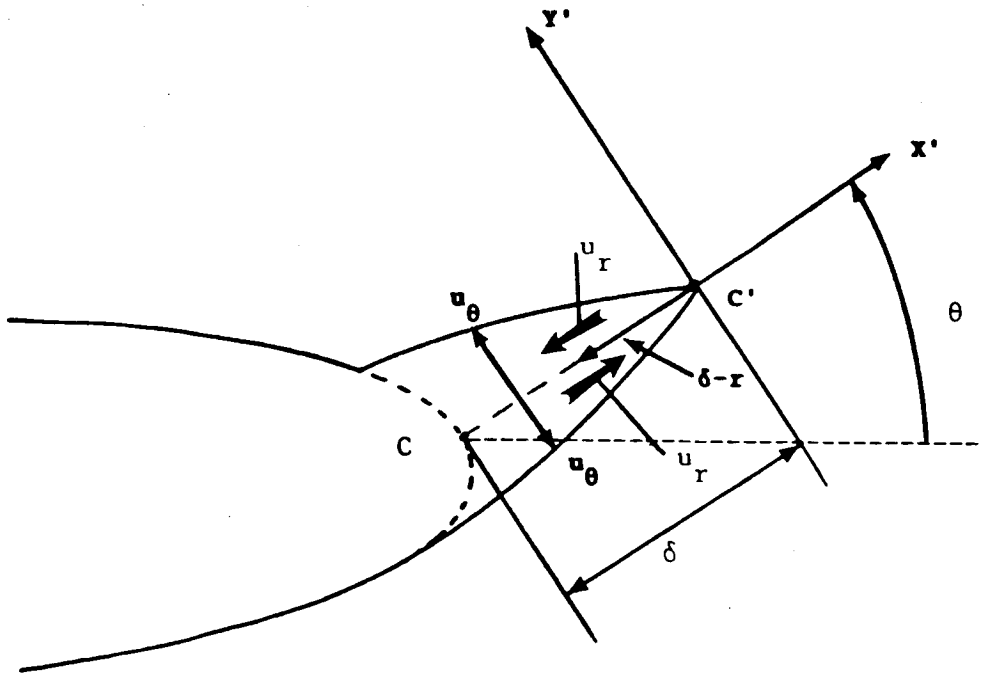

b) Displacement along the the crack extension C'C

Fig. 2.4 Load and displacement along a crack extension CC'

approximation, it is assumed that the displacements for the kinked crack have the same general solution as for a straight crack, which correspond to the new crack tip C'; therefore the displacements for the kinked crack have the following form, based on relations in Eq. 2.1.b and 2.2.b for θ equal to π :

$$u_r = K'_{II} /(2E)\left(\frac{\delta - r}{2\pi} \right)^{\frac{1}{2}} (1+\nu)(2\kappa+2)$$

$$u_\theta = K'_{I} /(2E)\left(\frac{\delta - r}{2\pi} \right)^{\frac{1}{2}} (1+\nu)(2\kappa+2) \qquad 2.7.a$$

where K'_I and K'_{II} are the new stress intensity factors for the kinked crack.

To find K'_I and K'_{II} above, a large number of investigators tried to determine the stress intensity factors for a kinked crack as function of the stress intensity factors of the main crack with no kink. Some of those investigations include the works of Hussian, Pu and Underwood [15], Wu [16], and Hayashi and Nemat-Nasser [17]. Hussian et al., Ref. [15], found a discountinuity in the solution as the kinked crack length goes to zero. Wu [16] and Hayashi's [17] results were in agreement with each other and they concluded that by taking the limiting case, where CC' goes to zero, the corresponding relation for K'_I and K'_{II} are as follows, (see Ref. [17]):

$$K_I' = K_I \cos^3 \frac{\theta}{2} - 3 K_{II} \sin \frac{\theta}{2} \cos^2 \frac{\theta}{2}$$

$$K_{II}' = K_I \sin \frac{\theta}{2} \cos^2 \frac{\theta}{2} + K_{II} \cos \frac{\theta}{2} \left(1 - 3 \sin^2 \frac{\theta}{2} \right) \qquad 2.7.b$$

Substituting Eq. 2.6 and 2.7.a into Eq. 2.5, by making use of relations 2.7.b, the crack extension force will have the following form:

$$G = \frac{(1+\nu)(\kappa+1)}{4E} \left\{ \left(K_I \cos^3 \frac{\theta}{2} - 3K_{II} \sin \frac{\theta}{2} \cos^2 \frac{\theta}{2} \right)^2 + \left(K_I \sin \frac{\theta}{2} \cos^2 \frac{\theta}{2} + K_{II} \cos \frac{\theta}{2} \left(1-3\sin^2 \frac{\theta}{2}\right) \right)^2 \right\} * \lim_{\delta \to 0} 1/\delta \int_0^{\delta} \sqrt{\frac{1- r/\delta}{r/\delta}}\, dr \qquad 2.8$$

Evaluating the integral by making the following substitution $\frac{r}{\delta} = \sin^2\phi$; then $dr = 2\,\delta \sin\phi \cos\phi \, d\phi$, gives

$$\frac{1}{\delta} \int_0^{\delta} \sqrt{\frac{1- r/\delta}{r/\delta}}\, dr = \int_0^{\frac{\pi}{2}} 2 \cos^2 \phi \, d\phi$$

$$= 2 \left(\frac{\phi}{2} + \frac{\sin 2\phi}{4} \right) \Big|_0^{\pi/2}$$

$$= \frac{\pi}{2}$$

Substituting the value of the integral into Eq. 2.8, one gets the crack extension force for mixed-mode loadings at any arbitrary angle θ measured from the original crack direction:

$$G = \frac{(1+\nu)(\kappa+1)}{4E} \left\{ \left(K_I \cos^3 \frac{\theta}{2} - 3K_{II} \sin \frac{\theta}{2} \cos^2 \frac{\theta}{2}\right)^2 + \left(K_I \sin \frac{\theta}{2} \cos^2 \frac{\theta}{2} + K_{II} \cos \frac{\theta}{2} \left(1-3\sin^2 \frac{\theta}{2}\right)\right)^2 \right\} \qquad 2.9$$

Equation 2.9 is divided here into two parts: first, the crack extension force due to the tensile opening displacement mode, $\int u_\theta \sigma_{\theta\theta}\, dr$, called herein the "tangential crack extension force": $G_{\theta\theta}$; and second, the crack extension force due to shear opening displacement mode, $\int u_r \sigma_{\theta r}\, dr$, called herein the "shear crack extension force": $G_{r\theta}$. This separation of the energy release rate, G, is based on the fact that there are fractographically two types of crack growth, i.e. the shear mode growth and the tensile mode growth (Ref. [19]), which are controlled by two different driving forces, i.e. $G_{r\theta}$ and $G_{\theta\theta}$, respectively.

The separation of the two driving forces for the crack growth is given in the following equation for the crack extension forces, $G_{\theta\theta}$ and $G_{r\theta}$:

$$\begin{Bmatrix} G_{\theta\theta} \\ G_{r\theta} \end{Bmatrix} = \frac{(1+\nu)(\kappa+1)}{4E} \begin{Bmatrix} \left(K_I \cos^3 \frac{\theta}{2} - 3K_{II} \sin \frac{\theta}{2} \cos^2 \frac{\theta}{2}\right)^2 \\ \left(K_I \sin \frac{\theta}{2} \cos^2 \frac{\theta}{2} + K_{II} \cos \frac{\theta}{2} \left(1-3\sin^2 \frac{\theta}{2}\right)\right)^2 \end{Bmatrix} \qquad 2.10$$

When θ is zero, i.e. looking at the extension forces ahead of the crack tip in the direction of the main crack, Eq. 2.10 reduces to:

$$\begin{Bmatrix} G_{\theta\theta} \\ G_{r\theta} \end{Bmatrix} = \frac{(1+\nu)(\kappa+1)}{4E} \begin{Bmatrix} K_I^2 \\ K_{II}^2 \end{Bmatrix} \qquad 2.11$$

Taking a closer look at the tangential crack extension force due to the tensile opening mode, $G_{\theta\theta}$, it can be shown that it is similar to the maximum tangential stress theory proposed by Erdogan and Sih [18] for determining the angle of crack propagation under mixed-mode loadings.

Otsuka et al. [19] ran experiments on fatigue crack growth under mixed-mode conditions and observed two different fratographical modes of failures; the shear mode growth region (controlled by $G_{r\theta}$) and the tensile mode growth region (controlled by $G_{\theta\theta}$), as seen in Fig. 2.5. For given stress intensity factors, K_I and K_{II}, the dominant mode of failure can be determined from the crack extension forces. For very low values of the stress intensity factors, i.e. low values of K_I and K_{II}, there is no crack growth. The experimental data points of no crack growth are shown as hollow circles. For intermediate values of K_I and K_{II}, the crack growth is governed by the shear crack extension force, $G_{r\theta}$. The experimental data points of shear mode growth are shown as triangles. For high values of K_I and K_{II}, the crack growth is governed by the tensile crack extension force, $G_{\theta\theta}$. The experimental data points of tensile mode growth are shown as solid circles.

Therefore, below a threshold value of the shear crack extension force, $G_{r\theta\,th}$, there is no crack growth. Above this

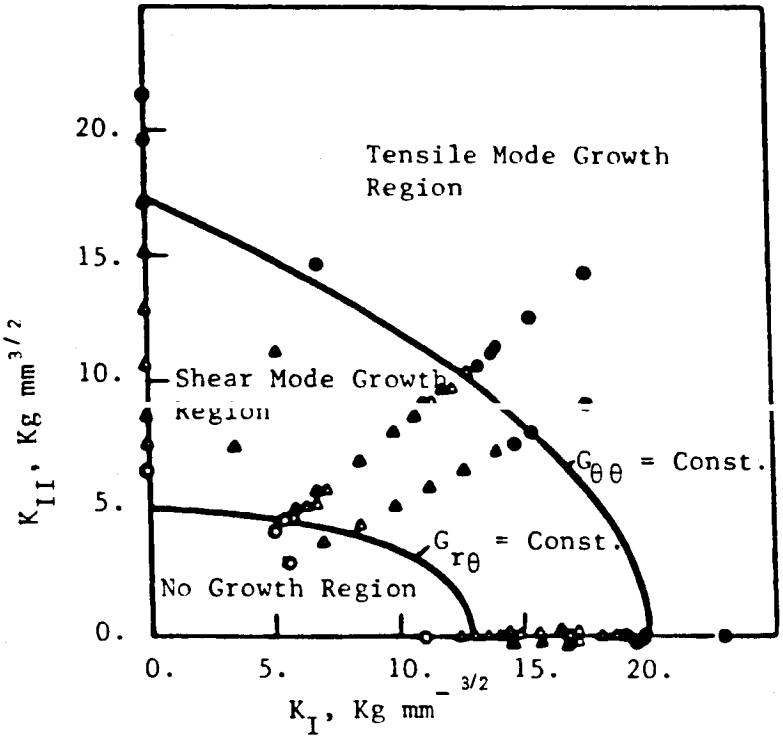

Fig. 2.5 Experimental Observation of Different Crack Growth Modes, Ref. [19]

threshold value, the shear mode growth is observed. Above a critical tensile crack extension force, $G_{\theta\theta th}$, tensile mode growth is observed.

Another method to account for the crack extension force is through the path independent integral, known as the J integral. As will be seen in the next section, the J integral is defined for self-similar crack extension, i.e. crack extension in its original direction.

2.3 The J integral

The J integral is often used as an alternative form to the energy release rate, G, when the nonlinear material ahead of the crack tip cannot be ignored. As first defined by Rice [20], the J integral has the form:

$$J = \int_s (W n_1 - t_i u_{i,1}) \, ds \qquad 2.12$$

where s is a path surrounding the crack tip, W is the strain energy density, and t_i is the traction conponent on s, and ds is an element of s, see Fig. 2.6. Since Rice, theoretical studies have been undertaken to investigate the fundamental mathematical characteristics of the J integral, and Sternberg [21] has shown that the J integral is a vector of path-independent integrals, defined as follows:

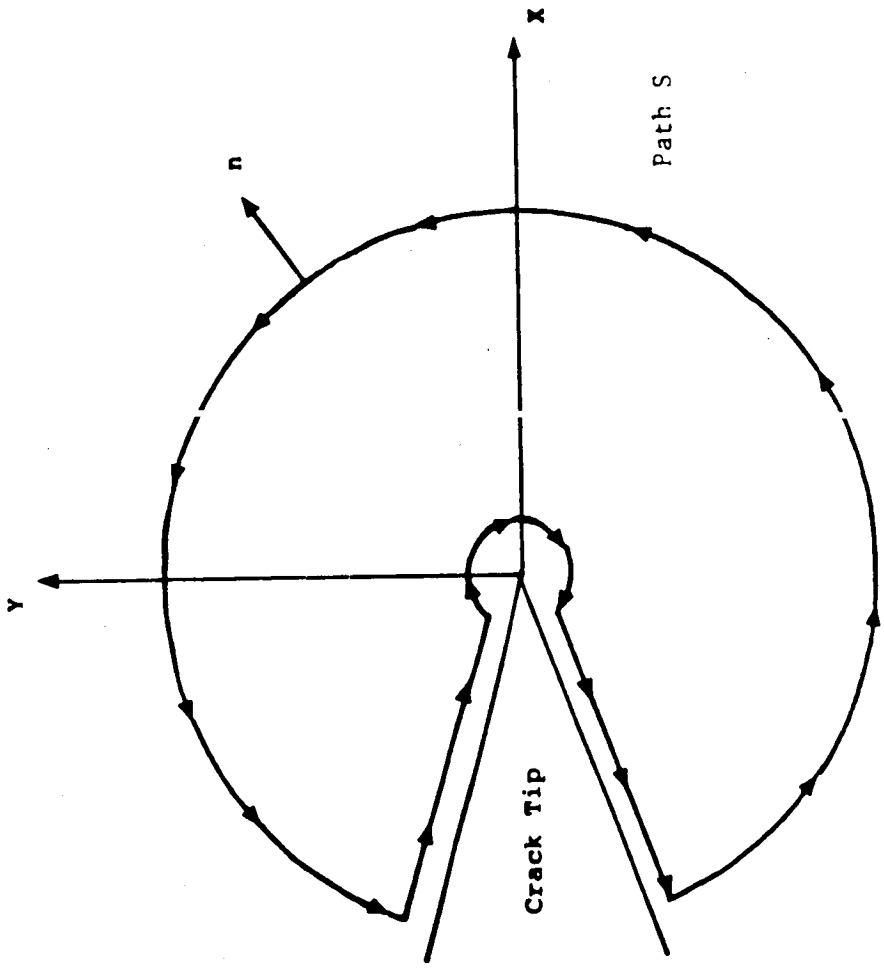

Fig. 2.6 Path S around the crack tip for J integral Calculation

$$J_k = \int_s (W n_k - t_i U_{i,k}) \; ds \qquad 2.13$$

This concept of the J integral may show much promise for mixed-mode loadings. Eq. 2.13 defines the extension forces in three different directions. Substituting the solution of the stress and displacement fields from 2.1 and 2.2 into the J integral, one gets, for mode I and mode II only:

$$\begin{Bmatrix} J_1 \\ J_2 \end{Bmatrix} = \frac{(1+\nu)(\kappa+1)}{4E} \begin{Bmatrix} K_I^2 + K_{II}^2 \\ -2 K_I K_{II} \end{Bmatrix} \qquad 2.14$$

To determine the crack extension at any arbitrary angle, a simple trigonometric relation is used to give:

$$J_{\theta\theta} = J_1 \cos\theta + J_2 \sin\theta$$

$$J_{\theta\theta} = \frac{(1+\nu)(\kappa+1)}{4E} ((K_I^2 + K_{II}^2) \cos\theta - 2 K_I K_{II} \sin\theta) \qquad 2.15$$

Note that for pure mode I or mode II, ($K_I = 0$ or $K_{II} = 0$), the maximum crack driving force is in the direction of self-similar crack growth. This observation contradicts some basic pure mode II tests where the angle of crack propagation was observed at 70 degrees from the original crack plane.

Bui, Ref. [22], showed that J_2 defined in Eq. 2.13 is not

path independent and that Eq. 2.13 is incorrect. He proposed a new approach to calculate the integral by dividing the stress and displacement fields into symmetric and antisymmetric parts:

$$J = J_I + J_{II} \qquad 2.16.a$$

where: $$J_I = \int_s \{ W^I n_1 - t_i^I u_{i,1}^I \} \, ds \qquad 2.16.b$$

and $$J_{II} = \int_s \{ W^{II} n_1 - t_i^{II} u_{i,1}^{II} \} \, ds \qquad 2.16.c$$

where u_i^I and t_i^I are the symmetric displacement and traction fields and u_i^{II} and t_i^{II} are the antisymmetric displacement and traction fields. Substituting into Eq. 2.16, the closed form solutions of the stress and displacement fields around a crack tip, one gets:

$$\begin{Bmatrix} J_I \\ \\ J_{II} \end{Bmatrix} = \frac{(1+\nu)(\kappa+1)}{4E} \begin{Bmatrix} K_I^2 \\ \\ K_{II}^2 \end{Bmatrix} \qquad 2.17$$

which correspond to the crack extension force for $\theta = 0$, in Eq. 2.11. As seen from the above definition of the new approach to the J integral, only self-similar crack extension is measured, and the J integral is an alternative method to determine the

stress intensity factors using far away stresses and displacements, and not as a crack extension force for any arbitrary angle.

2.4 Mixed-Mode Crack Propagation Criteria

Many theories had been proposed to predict the angle of initial crack growth under mixed-mode loading conditions. The most important criteria are the maximum tangential stress [18], the minimum strain energy density factor [23], the J integral approach [24], the pure mode I theory [25], and the crack extension forces, as defined earlier. All the methods predict almost the same direction of crack propagation for near mode I loadings, but when mode II become dominant each method points to a different direction. A brief description of each of the above methods is given next with a comparison of the first three and the crack extension forces over a wide range of mixed-mode loadings.

Maximum tangential stress:

This criterion is based on the direction of the maximum tangential stress around a crack tip [18], which also corresponds to the maximum tangential crack extension force, $G_{\theta\theta}$ in Eq. 2.11. It can be seen that when $\sigma_{\theta\theta}$ in Eq. 2.1.a is maximum, $\sigma_{r\theta}$ is equal to zero. This criterion is based on the observation that the crack will grow in the radial direction from the crack tip and

perpendicular to the maximum tangential stress when the shear stress is zero. The direction of crack propagation based on this criterion is given by [26]:

$$\tan(\theta/2) = 1/4\ K_I/K_{II} + 1/4\ \sqrt{(K_I/K_{II})^2 + 8} \qquad 2.18$$

Minimum Strain Energy Release Rate:

Sih [24] has advocated the idea that the local strain energy density factor, S = r dW/dV, should be the governing quantity for the fracture process direction, (where r is the distance from the crack tip and dW/dV is the strain energy density). The strain energy density factor is given by:

$$S = a_{11} K_I^2 + 2\ a_{12} K_I K_{II} + a_{22} K_{II}^2 \qquad 2.19$$

$$a_{11} = \frac{\mu}{16}\ ((1 + \cos\theta)\ (\kappa - \cos\theta))$$

$$a_{12} = \frac{\mu}{16}((\sin\theta\,(2\cos\theta - \kappa + 1))$$

$$a_{22} = \frac{\mu}{16}((\kappa + 1)\ (1 - \cos\theta) + (1 + \cos\theta)(3\cos\theta - 1))$$

where μ is the shear modulus, equals $E/(2(1+\nu))$ and κ is as defined earlier equals $(3-4\nu)$ for plane strain condition.

The crack will propagate in the direction of the minimum

strain energy density factor given by: $dS/d\theta = 0$. It can be seen that the angle of crack propagation will depend on the poisson's ratio, ν, in this theory as opposed to the rest of the criteria.

J Integral Theory:

This theory is based on the generalized J integral developed by Sternberg [21], and the crack will propagate in the direction of the maximum J as defined in Eq. 2.15. The direction of the crack propagation based on the J integral theory is given by:

$$\tan\theta = -2\, K_I K_{II} / (K_I^2 + K_{II}^2) \qquad 2.20$$

Pure Mode I Theory:

The pure mode I criterion, from [25], is based on the idea that material separation in the process region ahead of the crack tip takes place in pure mode I, the opening mode. When this criterion is applied, a number of tentative extensions of the crack in different directions have to be studied. The direction to be chosen has to fulfill the criterion, $K_{II} = 0$. This criterion corresponds, to some extent, to the maximum tangential stress, where $\sigma_{\theta\theta}$ is maximum and $\sigma_{r\theta}$ is zero. The maximum tangential stress criterion tries to predict the new stress intensity factors for the kinked crack from the original crack (crack with no kink), while the pure mode I case actually extends the crack in the direction for which K_{II} equals zero. The pure mode I theory is more accurate, but needs a large number of

trials before the direction of $K_{II} = 0$ is known.

Crack Extension Forces Criterion:

The crack growth direction based on the crack extension forces criterion depends on the direction along which the crack extension forces are maximum. When the value of the tangential crack extension force is less than a threshold value $G_{\theta\theta th}$, the shear crack extension force is the crack driving force. The direction of the crack propagation will be governed by the direction of the maximum shear crack extension force, $G_{r\theta}$. For values of the tangential crack extension force greater than the threshold value, the direction along which the maximum tangential crack extension force acts, is the direction of propagation, (see Fig. 2.5).

A comparison of the direction of crack propagation for the first three criteria and the crack extension forces criterion is given in Fig. 2.7 for different ratios of mixed-mode loadings. The arc-tangent of the ratio of the stress intensity factors, K_I/K_{II}, is plotted versus the predicted crack propagation angle for the above criteria. For near pure mode I loadings, $\tan^{-1} K_I/K_{II}$ greater than 60 degrees, good agreement of the three methods is observed, but for near pure mode II loadings a huge discrepancy is observed.

For pure mode II, the maximum tagential stress theory as well as the maximum tangential crack extension force criterion predict an angle of 70.53 degrees, the minimum strain energy

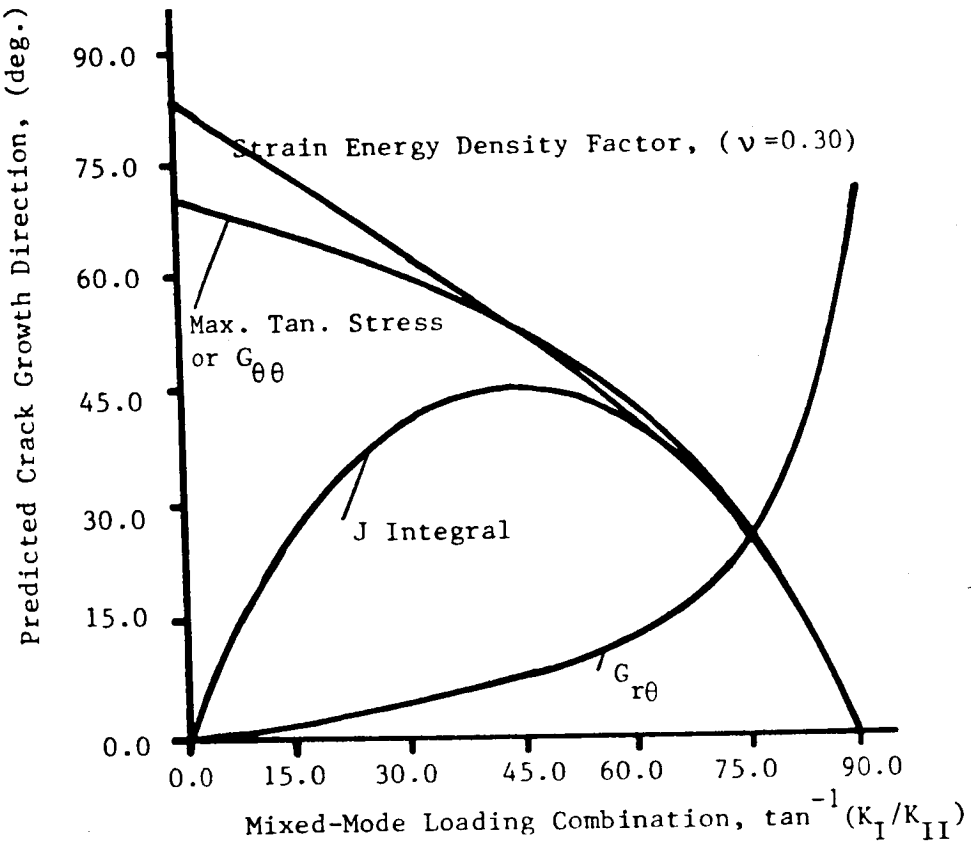

Fig. 2.7 Prediction of the Crack Growth Direction for Different Criterions

density factor theory gives an angle of 83.61, while the J integral approach gives a zero angle. The difference between the J integral and the other criteria can be explained from the wrong J_2 definition as seen earlier in section 2.3.

For pure mode II, based on the crack extension force criteria, the propagation direction will be zero degree if the shear crack extension force is governing and 70.53 degrees if the tangential crack extension force is dominant.

The crack extension force criteria will be used to determine the crack growth rate and direction in the failure analysis of the inner raceway of high speed bearings.

Knowing the crack extension forces and the fracture criteria, a crack propagation law can be formulated to predict the crack propagation rate under mixed-mode loadings.

2.5 Fatigue Crack Propagation Law for Mixed-Mode

Under cyclic loading the crack propagation occurs at lower stresses than it does for static loading. For typical fatigue fracture of brittle materials, macroscopic plastic deformation is not involved. Instead, submicroscopic slip lines developed ahead of the crack tip, that can intensify and broaden with each cycle. Those slip lines are developed along unfavorable oriented grains. But these slip bands cannot cause fracture in themselves, since their effect is to harden the material. When a material work-

hardens, it will be vulnerable to the tangential stresses around the crack tip, which try to open up the defects causing the increase in microcrackings with increasing number of cycles. The formation and the growth of these microscopic cracks ahead of the crack tip represent the damage accumulation. This damage accumulation is the cause of the weakening of the material ahead of the crack tip, and the decrease of the crack resistance force. The crack resistance force should be a decreasing function with increasing number of cycles, and how fast the crack resistance force decays is a function of the maximum range of G or K. But the crack growth is not continuous since experimental evidence has shown that the crack growth stops or slows down to a level where no crack growth is observed. After N numbers of cycles when the crack resistance ahead of the crack tip is decreased, the crack will grow instantaneously a distance ℓ, and then stop. At this position the crack tip has reached a region where the damage accumulation is non-existent or is so low that more cycles are required before the crack can grow. This explaine the experimental observed jump like growth of fatigue cracks.

Generally, one can find the formulation of the fatigue crack growth as follows, Ref. [27]:

$$d\,a(t) = \mathbf{F}\,(\,a(t),\, P(t),\, d(t),\, t)\;\; d\,t \qquad 2.21$$

where a(t) is the length of the dominating crack, p(t) is the

stress load and d(t) includes the damage accumulation and material properties.

A simplified version of Eq. 2.21 was given by Paris [28], where the damage accumulation was ignored and the load and crack length were combined together as a function of the stress intensity factor. Thus, Eq. 2.21 reduces to, [28]:

$$da / dN = C (\Delta K)^{n} \qquad 2.22$$

Eq. 2.22 is based on experimental results, for mode I loading condition, and basically describe region II, in Fig. 1.4. But more careful experiments had shown that the mean stress has an effect on the fatigue crack growth, and Eq. 2.22 was therefore modified to the following form, Ref. [29]:

$$da / dN = C (\Delta K)^{n_1} (K_{max})^{n_2} \qquad 2.23$$

Recently, Forman et al., Ref. [13], have provided a general expression which takes into account all the regions of Fig. 1.4;

$$da / dN = C (\Delta K - \Delta K_{th})^{n_1} / ((1-R) K_{Ic} - \Delta K)^{n_2} \qquad 2.24$$

where R is the stress ratio, and equals to K_{min}/K_{max}.

All the above equations are based on pure mode I loadings, and must be generalized to include the mixed-mode loading

conditions and the damage accumulation.

The first mixed-mode fatigue crack growth equation was derived by Sih [11], based on his strain energy density factor, where fatigue crack growth occurs in the direction of the maximum change in the strain energy factor, and the fatigue growth equation becomes:

$$da / dN = C (\Delta S_{min})^n \qquad 2.25$$

where ΔS_{min} is given by [11]:

$$\Delta S_{min} = 2(a_{11} \bar{K}_I \Delta K_I + a_{12}(\bar{K}_{II} \Delta K_I + \bar{K}_I \Delta K_{II}) + a_{22} \bar{K}_{II} \Delta K_{II}) \qquad 2.26$$

where $\bar{K}_J$ is the mean stress intensity factor, ΔK_J is the stress intensity factor range, the a_{ij}'s are functions of the angle of crack propagation for which ΔS_{min} is a maximum and are given in Eq. 2.19.

Alternatively, one can easily extend the crack propagation to the mixed-mode loadings, by making use of the crack extension forces along any angle θ, instead of the mode I stress intensity factor in the equations on page 43. By substituting relations 2.10, for the crack extension forces in Forman's equation, the crack growth rate will be equal to:

For Tensile Mode of Crack Growth:

$$\frac{da}{dN} = C \frac{(\Delta G_{\theta\theta} - \Delta G_{\theta\theta th})^{n_1}}{((1-R)G_{\theta\theta c} - \Delta G_{\theta\theta})^{n_2}} \qquad 2.27$$

For Shear Mode of Crack Growth:

$$\frac{da}{dN} = C \frac{(\Delta G_{r\theta} - \Delta G_{r\theta th})^{n_1}}{((1-R)G_{r\theta c} - \Delta G_{r\theta})^{n_2}} \qquad 2.28$$

Therefore, depending on the mixed-mode loading conditions, one must choose the proper mode of failure. Eq. 2.27 would be valid for the tensile mode of fatigue crack growth while Eq. 2.28 would be valid for the shear mode of fatigue crack propagation. The ΔG_{ijth} is the threshold crack extension below which no crack propagation is observed.

To determine the dominant crack growth mode, the values of the maximum changes of the crack extension forces are compared with the threshold values. Fig. 2.8 represents the boundary for different crack growth modes. For values of $\Delta G_{\theta\theta}$ greater than $\Delta G_{\theta\theta th}$ tension mode is observed and Eq. 2.27 is valid. For values of $\Delta G_{\theta\theta}$ less, two regions are observed; a) no crack growth region for $\Delta G_{r\theta}$ less than $\Delta G_{r\theta th}$, b) shear mode growth for value of $\Delta G_{r\theta}$ greater, and Eq. 2.28 is valid.

This separation of the growth modes can easily explain the different crack growth directions observed in pure mode II tests ran by Buzzard et al., Ref. [52]. For very small cracks the

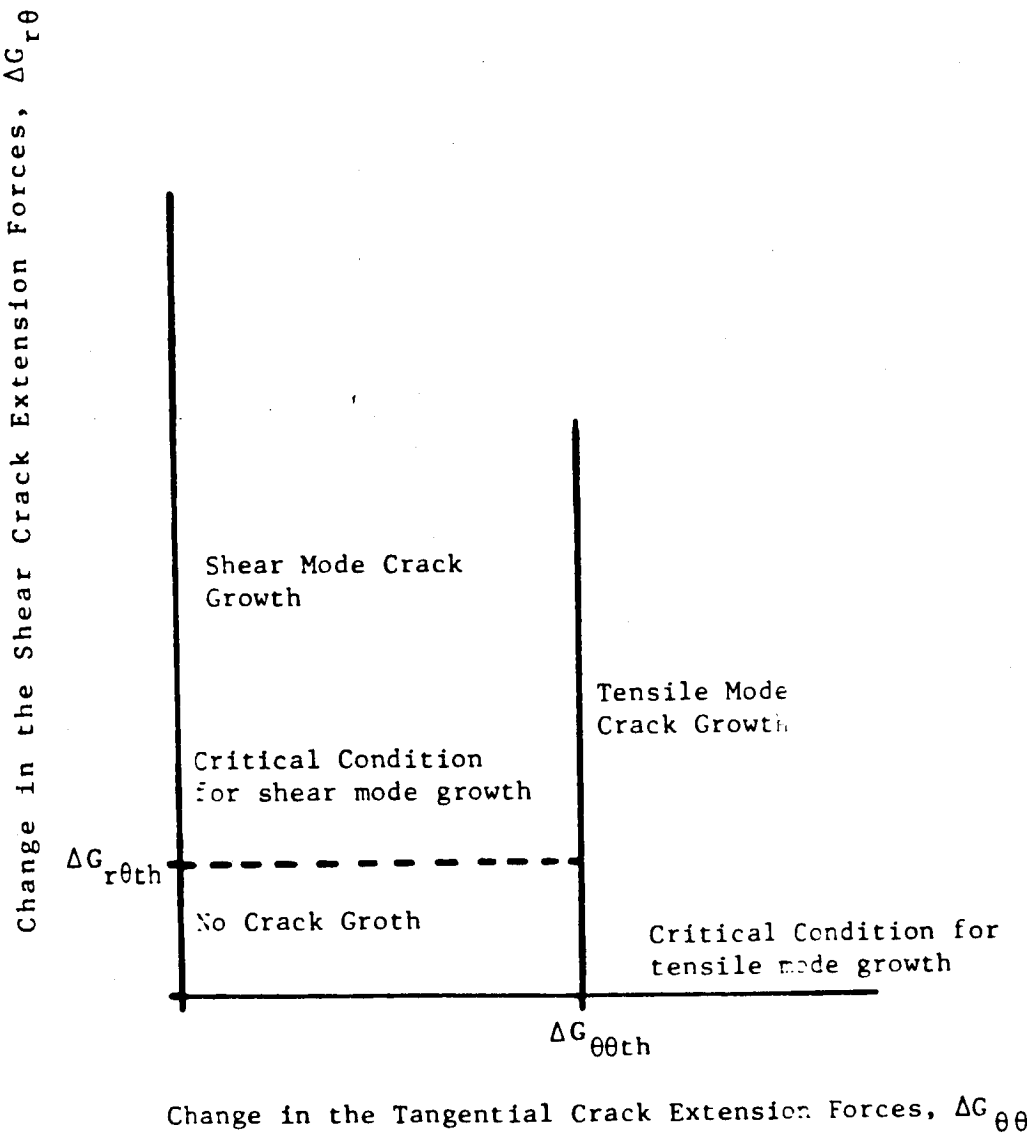

Fig. 2.8 The Condition of the Initiation of Fatigue Crack Growth in Shear Mode and Tensile Mode

crack extension forces are so small that the shear mode is dominant causing the crack to extend in the original direction. For larger cracks, where the tangential crack extension are higher than the threshold $\Delta G_{\theta\theta\,th}$, the crack changes direction, and propagates along 70.53 degrees, in the direction of the maximum change in $G_{\theta\theta}$, indicating a tensile growth mode.

Thus, the crack growth direction will be determined from the angle θ along which the change in the crack extension forces are maximum. The crack will keep on growing in this direction until a new loading combination changes the direction of the maximum change of G_{ii}.

The crack extension forces criteria will be used in analyzing the mixed-mode failure of the inner raceway of the high speed bearings. But before determining the crack growth direction and rate under mixed-mode loadings, the stress and displacement fields have to be determined first using the boundary integral equation method for any arbitrary crack geometry and orientation, and loading conditions as will be seen in the next chapter.

CHAPTER THREE

Boundary Integral Equation Method

3.1 Introduction

Methods of analysis in elasticity, and in most other scientific and engineering fields, have been revolutionized with the advance of computers. Most of the solutions, two dimensional or three dimensional, had been obtained for infinite or semi-infinite bodies using the stress functions techniques, which satisfy the desired boundary conditions near the origin and have the properties that the stress and/or displacement vanish or remain bounded as the boundary at infinity is approached. With the advance of computers, solutions for finite geometries and mixed boundary conditions were attainable by numerical techniques. First, the finite difference method was used, by replacing the differential equations by their classical finite difference equivalent. More recently, the finite element method, which makes use of the variational statement of the original differential equations to obtain solutions, has gained popularity. In both methods, finite difference and finite element, the continuum is discretized, making the accuracy of the solution a function of the fineness of the discretization. Another method of analysis, recently rediscovered by Rizzo in

1967, Ref. [31], the boundary integral equations method, BIEM, offers an attractive alternative. The boundary integral method involves the transformation of the partial differential equations describing the behavior of the unknowns inside and on the boundary of the domain to integral equations over the boundary, i.e. the integrals are functions of the boundary data only; thus enabling the reduction of the dimensionality of the problem. Closed form solutions can be obtained for simple finite geometries and loading conditions, when the integral equations are solvable. The resulting solution is the exact solution of the differential equation for the given boundary conditions. For complicated geometries and loadings conditions, the integral cannot be solved analytically and approximations have to be introduced. Therefore, in the BIEM, inaccuracies arise from numerical integration procedures, which means that by refining these approximations any degree of precision is theoretically achievable. By the approximation of the integration, the integral equation will be transformed to a set of linear algebraic equations. The resulting system of equations is smaller by an order of magnitude than those for the finite difference or the finite element methods, but are fully-populated, whereas in other methods the matrices are symmetric and most of the time banded.

The boundary integral equation method has seen increasing popularity in recent years because of the some of the advantages

listed below, Ref. [32], [33]:
i) a smaller set of algebraic equations to solve, ii) simple data preparation to run the problem, only boundary discretization is needed, iii) infinite and semi-infinite problems are properly modelled, iv) accurate solution of selective internal stresses and displacements, and v) good resolution for stress concentration problems.

In view of the above advantages, the boundary integral equation method was used herein to analyze the stress and displacement fields around a surface crack of the inner raceway of the high speed bearing.

A review of the two dimensional plane strain elastostatic solution by the boundary integral equation method is given next, with its implimentation in a general computer program. The three dimensional derivation is similar to the two dimensional and its implimentation can be found in Ref. [34].

3.2 Mathematical Derivation

The most direct derivation of the boundary integral equations is based on a singular solution of the Navier equations. The Navier equations of equilibrium (in terms of displacements) for two dimensional problems in elasticity are, Ref. [32]:

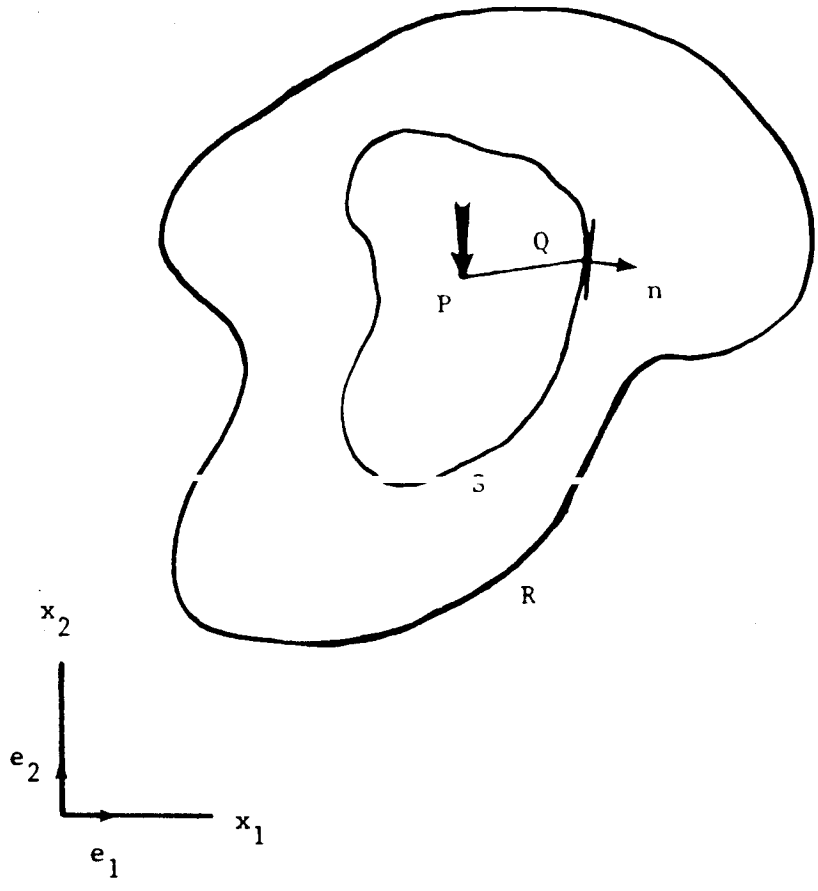

Fig. 3.1 Displacement Field along a Surface S, due to a Point Load P in an Infinite Region R

$$\nabla^2 u_i + 1/(1-2\nu)\ \theta_{,i} = 0 \qquad 3.1.a$$

$$\theta = u_{j,j} \qquad i,j = 1,2$$

where u_j are the displacements, ν is Poisson's ratio and the usual tensor notation is used, where a repeated subscript indicates summation over its range and a comma indicates partial differentiation. The Navier equations can be written in another form as:

$$u_{i,jj} + 1/(1-2\nu)\ u_{k,ki} = 0 \qquad 3.1.b$$

A solution to these equations can be obtained by making use of Kelvin's singular solution due to a single unit concentrated force acting in the interior of an infinite body [35] (see Fig. 3.1).

The displacement field at any point Q at distance r from the point P, where the force is applied is given by Ref. [35] :

$$u_i = \left\{-1/[8\pi G(1-\nu)]\right\}\left\{(3-4\nu)\ \ln r\ \delta_{ij} - r_{,i}\ r_{,j}\right\}\ e_j \qquad 3.2.a$$

or

$$u_i = U_{ij}\ e_j \qquad 3.2.b$$

where e_j are the unit base vectors, and

$$U_{ij} = \left\{-1/[8\pi G(1-\nu)]\right\}\left\{(3-4\nu)\ \ln r\ \delta_{ij} - r_{,i}\ r_{,j}\right. \qquad 3.2.c$$

where r is the distance between a field point Q with coordinates (x_i^Q) and the point of load application P with coordinates (x_i^P);

$$r = \left\{ (x_i^Q - x_i^P)\ (x_i^Q - x_i^P) \right\}^{\frac{1}{2}} \qquad 3.3$$

For plane stress, poisson's ratio ν is replaced by $\nu/(1+\nu)$, in all the equations, Ref. [32].

If we consider the field point Q to be on the boundary of a body cut out of the infinite region, then the traction forces can be determined on this boundary by

$$t_i = \sigma_{ij}\ n_j \qquad 3.4$$

where n_j is the component of the outward normal in the j direction at the surface of the body. Expressing the stress tensor in terms of displacements [35]

$$\sigma_{ij} = \left\{ 2G\nu/(1-2\nu) \right\}\ \delta_{ij}\ u_{m,m} + G\ (u_{j,i} + u_{i,j}) \qquad 3.5$$

where G is the shear modulus, differentiating Eq. 3.2 and substituting in Eq. 3.5, Eq. 3.4 becomes:

$$t_i = \left\{ -(1-2\nu)/[4\pi(1-\nu)r] \right\}\ \left\{ dr/dn\ \left[\delta_{ij} + [2/(1-2\nu)]\ r_{,i}\ r_{,j} \right] \right.$$
$$\left. - r_{,i}\ n_j + r_{,j}\ n_i \right\}\ e_j \qquad 3.6.a$$

or

$$t_i = T_{ij}\ e_j \qquad 3.6.b$$

where

$$T_{ij} = \left\{-(1-2\nu)/[4\pi(1-\nu)r]\right\}\left\{dr/dn\left[\delta_{ij} + [2/(1-2\nu)]\, r_{,i}\, r_{,j}\right] - r_{,i}\, n_j + r_{,j}\, n_i\right\} \qquad 3.6.c$$

We now make use of Betti's reciprocal theorem [36] which states: If an elastic body is subjected to two systems of surface tractions t_j and t^*_j, then the work that would be done by the first system t_j in acting through the displacement u^*_j of the second system is equal to the work that would be done by the second system t^*_j acting through the displacement u_j of the first system, i.e.;

$$\int_s t_j\, u^*_j\, ds = \int_s t^*_j\, u_j\, ds \qquad 3.7$$

where s is the boundary surface of the body, and ds is an element of surface area.

Suppose we now choose the second system of traction and displacement (t^*_j and u^*_j) to be the one produced by a single unit concentrated load, and the system u_j , t_j to correspond to the solution we are seeking. Since we know the solution to the unit concentrated load (Kelvin solution), we can solve for any of the unknown traction and displacement (t_j, u_j) by substituting Eq. 3.6 and 3.2 for t^*_j and u^*_j, respectively and solving the integral, Eq. 3.7. Because of the singular nature of U_{ij} and T_{ij} at r = 0, it is necessary to employ a limiting process as shown in Appendix A, resulting in the following equation, known as the

boundary integral equation:

$$\int_s t_j U_{ji} e_i \, ds = \int_s u_j T_{ji} e_i \, ds - C_{ji} u_i e_i \qquad 3.8.a$$

or in another form

$$C_{ij} u_j = \int_s U_{ij} t_j \, ds - \int_s T_{ij} u_j \, ds \qquad 3.8.b$$

where $C_{ij} = \delta_{ij}$ for interior points and $C_{ij} = \delta_{ij}/2$ for boundary points with smooth tangents. Eq. 3.8 is also known as Somigliana's identity. For very simple geometries and boundary conditions Somigliana's identity is satisfactory for obtaining analytical solutions, but for complex bodies a numerical solution is necessary and is discussed in the next section.

Once the unknown traction and displacement are determined on the boundary, internal displacements and stresses can be calculated as functions of the boundary displacements and tractions. For internal displacement, Eq. 3.8 is used with $C_{ij} = \delta_{ij}$, however for internal stresses Eq. 3.8 is differentiated and substituted in Eq. 3.5, to get [32]:

$$\sigma_{ij} = \int_s U_{ijk} t_k - T_{ijk} u_k \, ds \qquad 3.9$$

where

$$U_{ijk} = \{(1-2\nu)/[4\pi(1-\nu)r]\}\{\delta_{ik} r_{,j} + \delta_{jk} r_{,i} - \delta_{ij} r_{,k} + 2 r_{,i} r_{,j} r_{,k}/(1-2\nu)$$

$$T_{ijk} = \{G/[2\pi(1-\nu)r^2]\}\{2\,dr/dn\,[(1-2\nu)\,\delta_{ij}r_{,k} + \delta_{ik}\,r_{,j} + \delta_{jk}\,r_{,i} - 4\,r_{,i}\,r_{,j}\,r_{,k}] + n_i\,(2\nu r_{,j}\,r_{,k} + (1-2\nu)\,\delta_{jk}) + n_j\,(2\nu r_{,i}\,r_{,k} + (1-2\nu)\,\delta_{ik}) + n_k\,[2(1-2\nu)\,r_{,i}\,r_{,j} - (1-4\nu)\,\delta_{ij}]\}$$

Thus, the displacements and stresses at any interior point, if needed can be obtained by integrating numerically the boundary equations, Eq. 3.8 and Eq. 3.9, respectively with $c_{ij} = \delta_{ij}$, from the solutions of the stresses and displacements at the boundary.

3.3 Reduction of the Integral Equation to a set of linear Simultaneous Equations

The first step in solving the boundary integral equations is to reduce them to a set of linear simultaneous algebraic equations, if the integral are unsolvable in closed form. The boundary of a body to be analyzed is divided into M surface elements. Those elements can be linear or curved to map the boundary geometries, as seen in Fig. 3.2. Eq. 3.8 can then be rewritten as:

$$C_{ij}\,u_j = \sum_{b=1}^{M} \int_{sm} U_{ij}\,t_j\,dsm - \sum_{b=1}^{M} \int_{sm} T_{ij}\,u_j\,dsm \qquad 3.10$$

As an approximation the traction, t_j and displacement, u_j are

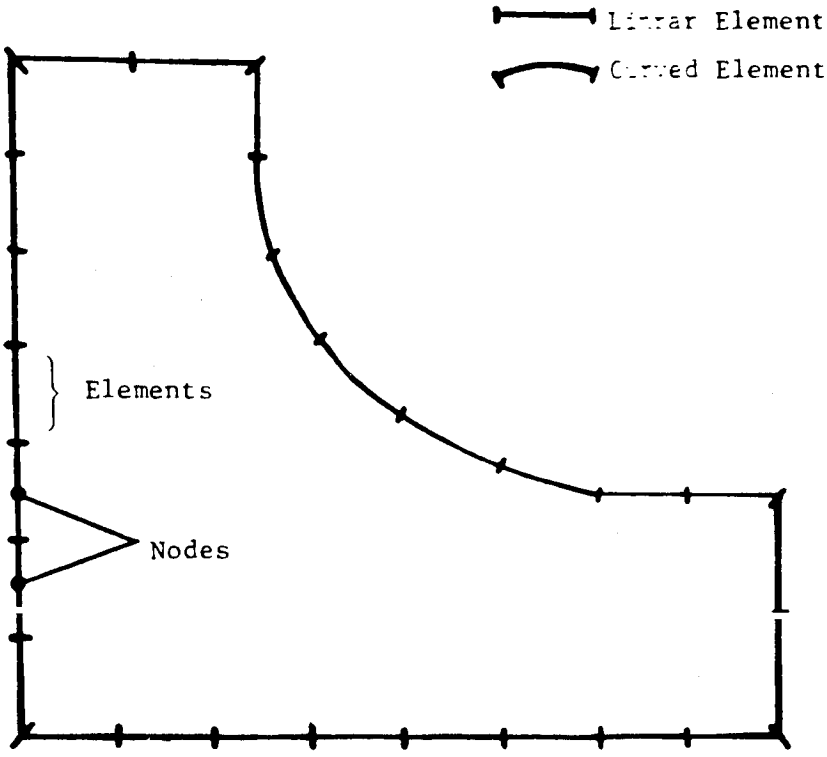

Fig. 3.2 Typical Two Dimensional Boundary Discretization

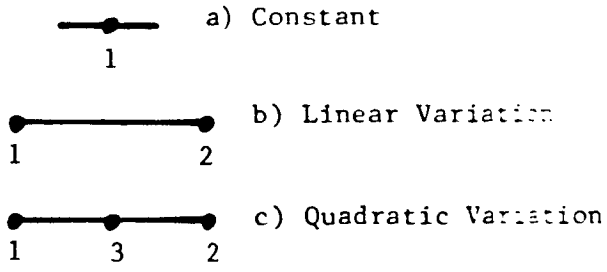

Fig. 3.3 Different Element Types

assumed constant or to vary linearly or quadraticaly over each element, as seen in Fig. 3.3. Thus, the tractions and displacements in each element can be approximated by:

$$t_i(x) = N^k(x)\, t_i$$

$$u_i(x) = N^k(x)\, u_i \qquad 3.11$$

For constant elements:

$$k = 1 \text{ and } N=1 \qquad 3.12$$

Here the traction and displacement are approximated as a constant having the values at the mid-point.

For linear elements, Ref. [37]:

$$k = 1,2$$

$$N^1 = (1-x)/2 \qquad N^2 = (1+x)/2 \qquad 3.13$$

$$J(x) = (x2-x1)/2$$

where J(x) is the Jacobian that transfers the integral from the global to the local coordinate system, where x1 and x2 are the in-plane coordinates of the nodes.

For quadratic elements, Ref. [37]:

$$k = 1,2,3$$

$$N^1 = x(x-1)/2 \qquad N^2 = x(x+1)/2 \qquad N^3 = (x+1)(1-x)$$

$$J(x) = (x2-x1)/2 + x(x1+x2 - 2\ x3) \qquad 3.14$$

If the surface is represented by M elements, then the integral equations become:

$$C_{ij}\, u_j(P) + \sum_{b=1}^{M} \sum_{k=1}^{n^b} u_j(Q^{bk}) \int T_{ij}(P,Q^{bk})\, N^k(x)\, J^b(x)\, dx = \sum_{b=1}^{M} \sum_{k=1}^{n^b} t_j(Q^{bk}) \int U_{ij}(P,Q^{bk})\, N^k(x)\, J^b(x)\, dx \qquad 3.15$$

where n^b is the total number of nodes in element b. J^b is the jacobian function for the bth element. The terms, $u_j(Q^{bk})$ or $t_j(Q^{bk})$, are the nodal values of the displacements and tractions, respectively, for the kth node within the bth element. Eq. 3.15 should be repeated N times, corresponding to the total number of nodal points. The total integral equations can be written as:

$$\sum_{a=1}^{N} \left\{ C_{ij}(P^a)\, u_j(P^a) + \sum_{b=1}^{M} \sum_{k=1}^{n^b} u_j(Q^{bk}) \int T_{ij}(P^a,Q^{bk})\, N^k(x)\, J^b(x)\, dx \right\} - \sum_{a=1}^{N} \sum_{b=1}^{M} \sum_{k=1}^{n^b} t_j(Q^{bk}) \int U_{ij}(P^a,Q^{bk})\, N^k(x)\, J^b(x)\, dx \qquad 3.16$$

The expression in Eq. 3.16 represents a set of 2N equations which can be written in matrix form as:

$$\left[C_{ij}{}^a + \Sigma\, \Sigma \int T_{ij}{}^{abk}\, N^k\, J^b\, dx \right] \left\{ u_j{}^a \right\} = \left[\Sigma\, \Sigma \int U_{ij}{}^{abk}\, N^k\, J^b\, dx \right] \left\{ t_j{}^a \right\} \qquad 3.17$$

where $i,j = 1,2$, $a = 1,N$, $b = 1,M$, and $k = 1,n^b$

or in general form

$$[\, A \,] \left\{ u \right\} = [\, B \,] \left\{ t \right\} \qquad 3.18$$

The integrals in Eq. 3.17 are easily solved numerically or in closed form over the domain of each element. For $Q^{bk} \neq P^{a}$, an eight point gaussian quadrature formula is implimented in the computer program, while for $Q^{bk} = P^{a}$, closed form solution for the lnr singularity is calculated.

For the case of a traction problem where the t's are known, or the case of a displacement problem where the u's are known, Eq. 3.18 reduces to the form

$$[\ A\ ]\ \{X\} = \{C\} \qquad 3.19$$

Eq. 3.19 represents a set of 2N linear algebraic equations which are to be solved by Gauss Elimination method. In case of mixed boundary value problem, where some values of both t and u are specified, it is necessary to interchange the columns of matrices A and B (in Eq. 3.18), so that all the unknown quantities are contained in the column vector u and the known values are contained in t, before reducing the equation to the form of Eq. 3.19.

By placing the nodes at the corners of elements two difficulties become apparent:

1) The possibility exists for nodes to be placed at sharp edges of the body rather than at flat surfaces. C_{ij}, in Eq. 3.16, is equal to $1/2\ \delta_{ij}$ for flat surfaces. For nodes at edge discountinuities C_{ij} can be computed in two ways. One uses a limiting process as derived in Appendix A. The second method is based on rigid body motion, as explained in Ref. [38], and is

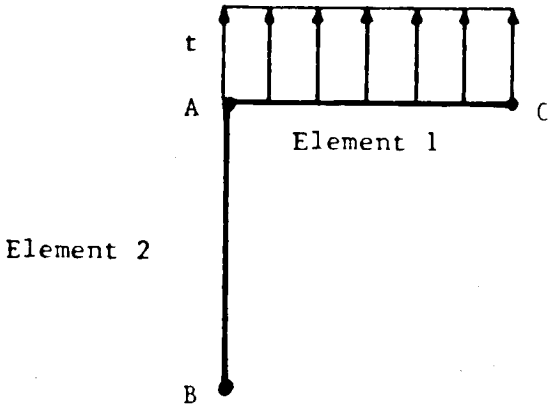

a) Different Loading Assigned to Node A

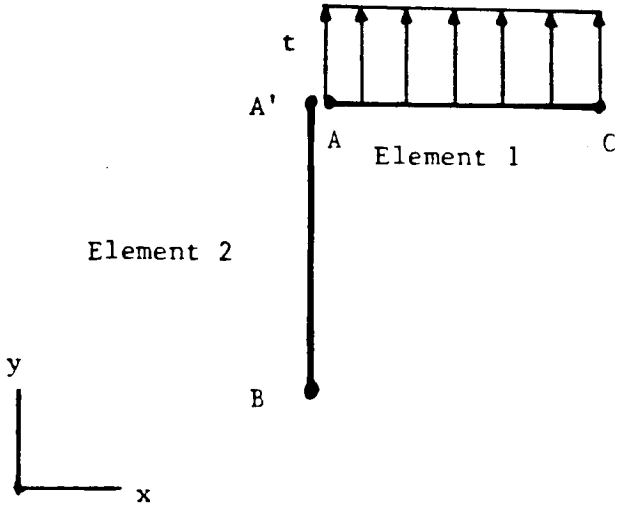

b) Two Distinct Nodes Placed at Loading Discontinuity

Fig. 3.4 Traction Discontinuity Models

given below:

$$C_{ij}(P,Q) = -\sum_{b=1}^{N} \int T_{ij}(P,Q)\ dx \qquad \text{for } P \neq Q^{b} \qquad 3.20$$

In the computer program, all C_{ij} terms are computed using Eq. 3.20. The value for C_{ij} on flat surfaces was computed by the above equation and it was found to be exactly equal to $1/2\ \delta_{ij}$ as predicted by the analytical formulation of Appendix A. The second method was implimented in the computer program merely as a check to the numerical integrations.

2) Placing nodes at corners of elements assures the continuity of displacements and tractions. However, in modelling real problems a step change in traction may exist. To assure discontinuity of applied tractions, the input values of traction are associated with the element they act on instead of the nodes. As an example, consider two adjacent elements which lie in two different planes (see Fig. 3.4). Element 1 is under uniform tension t while Element 2 is traction free. If the traction is associated with node A directly, an extra shearing traction exists in Element 2 varying from zero at node C to t at node A. By assigning the traction to a node of a specific element, in this example to node A of Element 1, the problem of adding extra traction is avoided. Alternatively, one can place two distinct nodes between elements 1 and 2, Fig. 3.4.b, but this method is not implemented here.

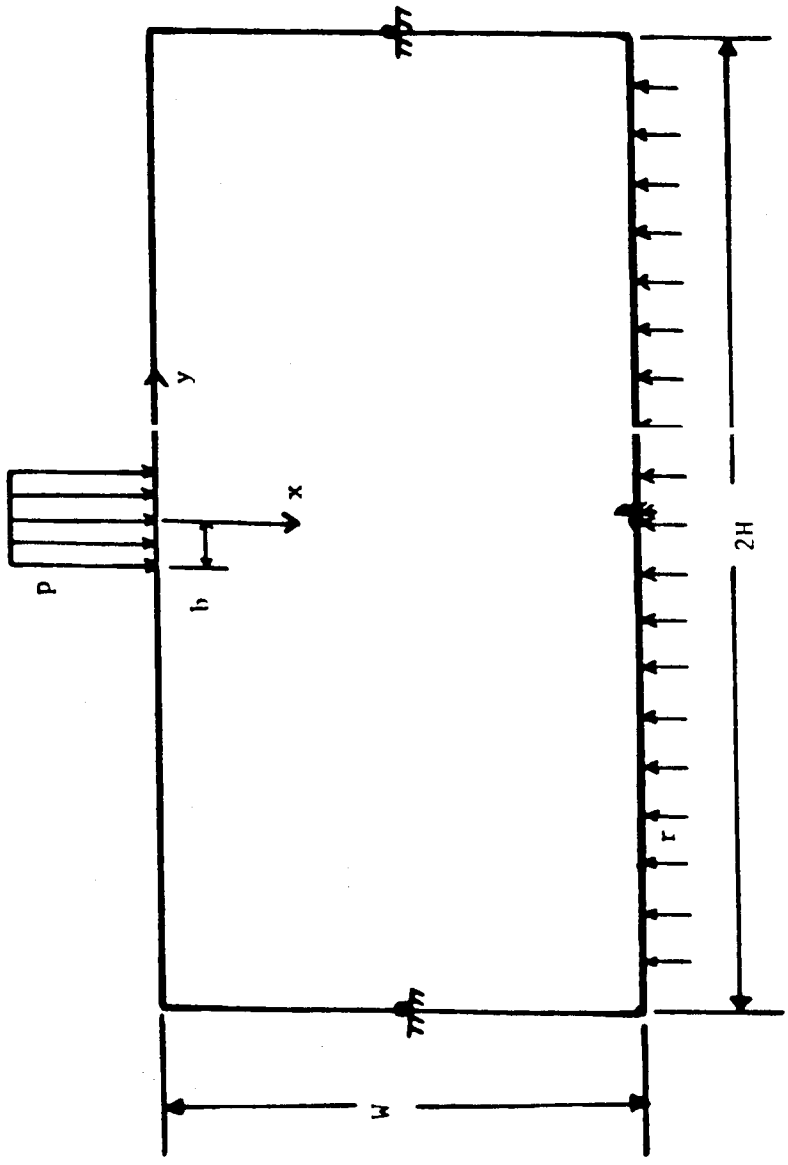

Fig. 3.5 Finite Plate with Uniformly Distributed Vertical Pressure on Part of the Boundary, with Dimension W/b = H/b = 30.

Some simple examples are shown next to test the boundary integral equation computer program written for the CRAY-XMP at NASA Lewis Research Center.

3.4 Uniform Distributed Load

The computer program of the two dimensional Boundary integral equation method (BIEM2), is first applied to a rectangular body with uniformly distributed vertical pressure on part of the boundary, under plane strain conditions, see Fig. 3.5. To simulate the semi-infinite region a uniform reaction force was applied to the bottom part of the plate. The dimensions of the body are $W/b = H/b = 30$, where H is the height, W is the width and b is half the length of the pressure applied. The poisson's ratio is equal to 0.3, and the applied pressure load is normalized with the modulus of elasticity, $p/E = 1$.

Two different sets of runs are studied. In the first set linear elements are used, while in the second set the quadratic elements are implimented. Different number of nodes are used in each set to analyze the order of convergence of the specific element type. A mesh generating program was written to facilitate the input data for the boundary discritazation. The required inputs are the material properties, the number of major subdivisions with the number of nodes desired in each one of them, and finally the coordinates of these major subdivisions.

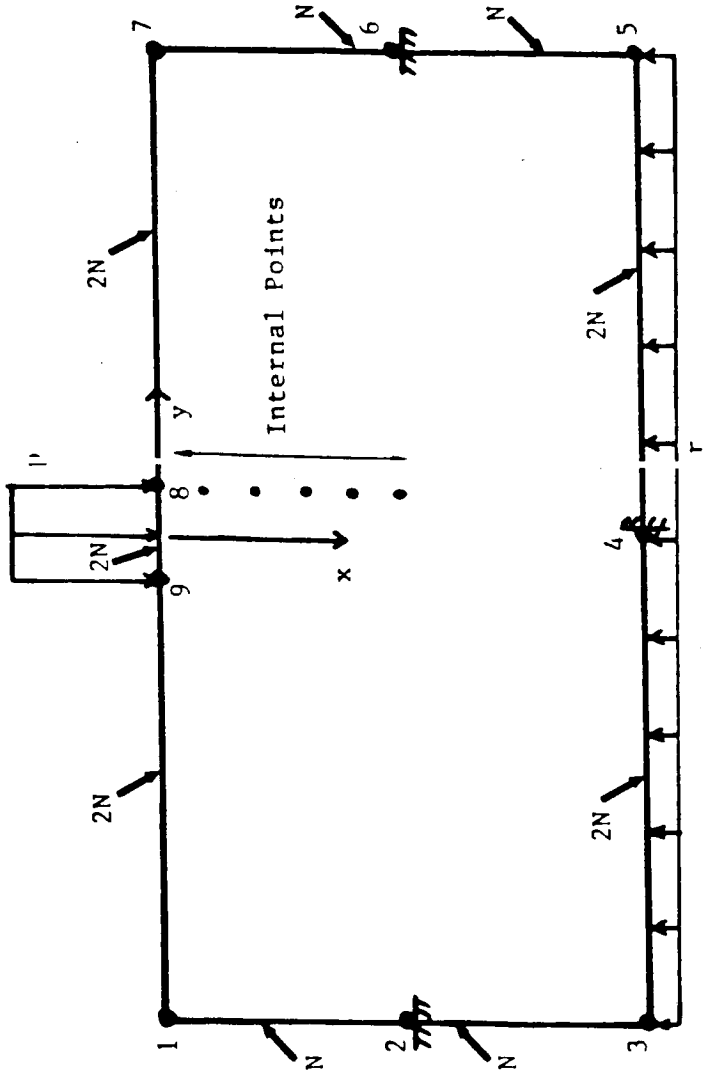

Fig. 3.6 Major Subdivisions for the Boundary Discretization, with the Number of Nodes in Each Subdivision.

The computer program (GENE1) will then generates the coordinates of the nodes and the element formations, with the proper fixities and loading conditions. Any loading condition can be implimented by just changing the loading function in the program. Coordinates of internal points, if desired, are also generated. For the above example, nine major subdivisions are chosen, (see Fig. 3.6), with fixities in the y-direction at coordinates 2 and 6, and in the x-direction at coordinate 4. A uniform traction is applied between coordinates 8 and 9, and along the bottom plate from coordinate 3 to 5. The numbers of nodes used in each subdivision is shown in Fig. 3.6. For the convergence analysis N in each mesh was 2, 4, 8, 16, 24, and 32 respectively.

To study the convergence of each element type, the values of the stresses at five internal points, picked below the edge of the uniform load, at distances y = b, and x = b, 2b, 3b, 4b, 5b, respectively, were compared, (see Fig. 3.6). Table 3.1 shows the values of the stresses for different mesh size at x = b and y = 2b. Good agreement with the closed form solution is observed for N = 32, for σ_{xy} and σ_{y}, but for σ_{x} the error is much higher because of truncation error.

A plot of the average error for the stresses (σ_{x}, σ_{y}, σ_{xy}), as function of the number of nodes, for the two type of elements is shown in Fig. 3.7. The average error of all the stresses for those five points is obtained from the elastic solution of a semi-infinite region and the analytical results from the BIEM

Table 3.1 Variations of the Stresses σ_x, σ_y, and σ_{xy}, as a Function of the Mesh Sizes, for an internal point at x = b and y = 2b of the uniform loaded plate.

	σ_x/p		σ_y/p		σ_{xy}/p	
N	linear	Quad.	Linear	Quad.	Linear	Quad.
2	-0.1142	-0.1195	-0.3718	-0.3840	0.1205	0.1326
4	-0.1088	-0.1063	-0.4020	-0.4117	0.1338	0.1412
8	-0.1002	-0.0980	-0.4138	-0.4165	0.1479	0.1531
16	-0.0972	-0.0963	-0.4128	-0.4124	0.1561	0.1588
24	-0.0969	-0.0964	-0.4120	-0.4112	0.1573	0.1593
32	-0.0967	-0.0966	-0.4105	-0.4098	0.1586	0.1595
exact	-0.0908		-0.4092		0.1592	

program. As seen in the figure, the difference between the linear and the quadratic elements is very small for the same number of nodes, and both methods converge to the same answer. This shows that for this problem, the converged solution does not depend on the element type. The advantage of the quadratic elements over the linear elements comes into consideration in the CPU time required to set up the integral equations. Since the integrals are evaluated over each element, and the number of elements for the quadratic type is half the number of elements for the linear one, the time needed is cut in half.

Fig. 3.8 shows the CPU time in seconds required on the CRAY XMP, for the linear and quadratic elements as a function of the number of nodes. As seen in the figure the average saving in CPU time between the quadratic and linear elements is about 33%. The reduction is only 33% because the CPU time reported is the total CPU time needed to set up and solve the system of algebraic equations, and both element types need the same solving time, for the same number of nodes. Considering the saving in CPU time, quadratic elements were used in the application of the BIEM to the mixed-mode failure of the inner raceway of the high speed bearings, and in the following examples on the stress intensity factor calculations.

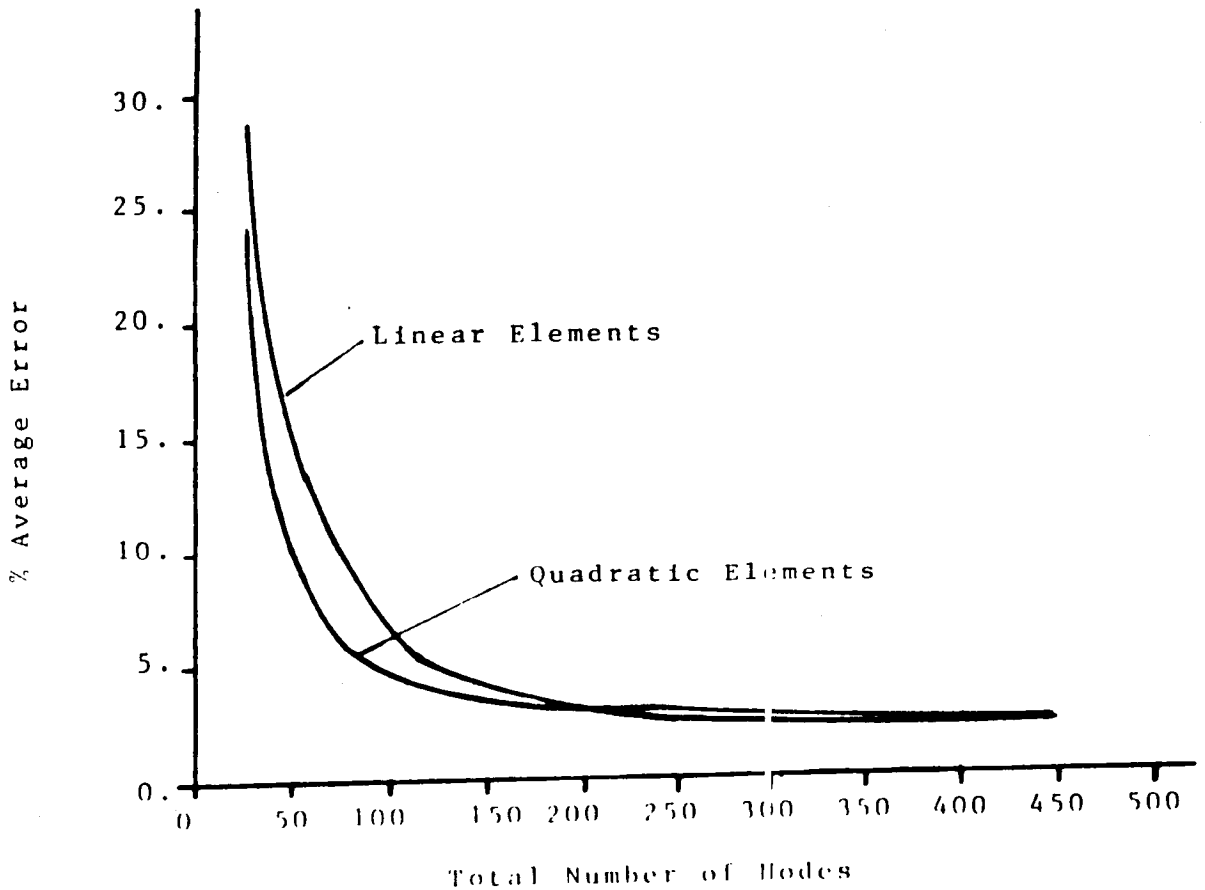

Fig. 3.7 Variation of the Average Error of the Five Internal Points, as a Function of the Total Number of Nodes

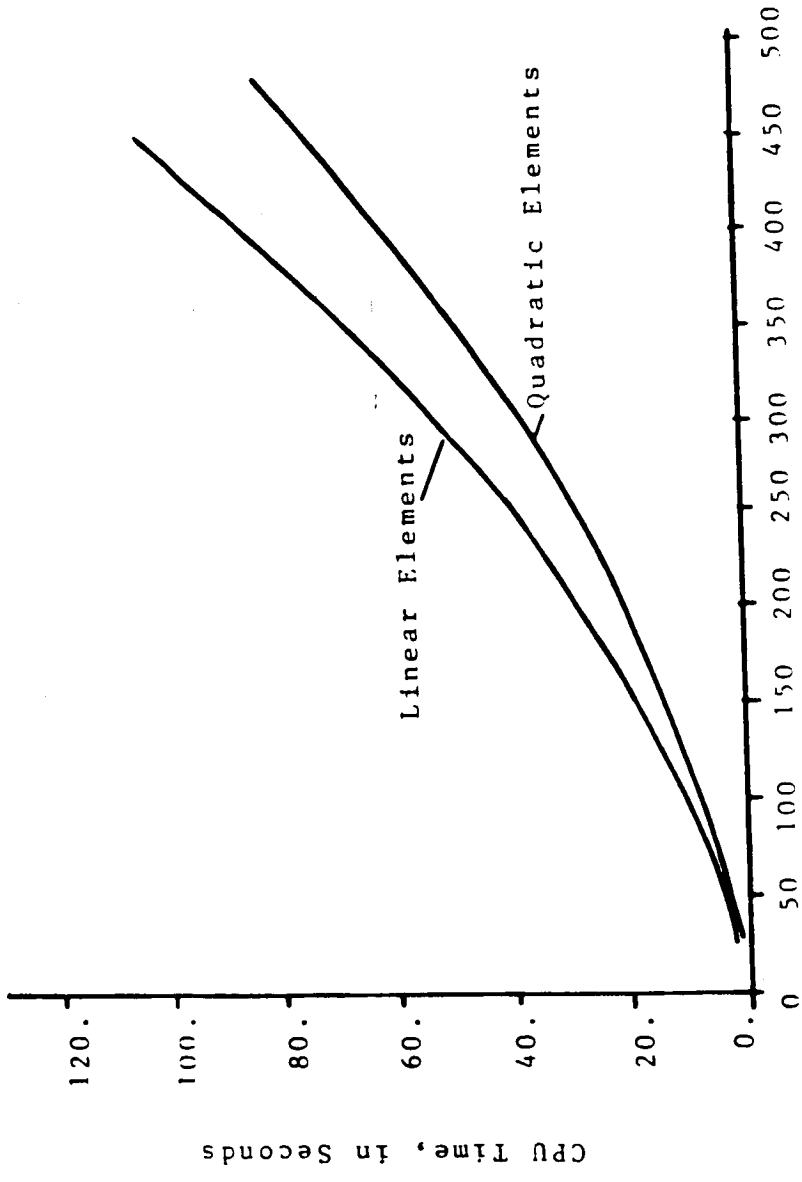

Fig. 3.8 Variation of the CPU Time Required for the Solution on the Cray XMP as a Function of the Total Number of Nodes

3.5 Determination of the Stress Intensity Factors

The next examples relate to the determination of the stress intensity factors for bodies with cracks using the BIEM. There is extensive literature on the numerical determination of the stress intensity factors. One of the methods which was adopted from finite elements is the use of a singularity element at the crack tip, Ref. [39]. The simplest crack singularity element is the quarter point element, where the mid-point of the quadratic element at the crack tip is moved to the quater point position, Ref. [39]. The disadvantage of these elements is that a transition element is needed and the crack tip should be fixed to give accurate results for the stress intensity factors. A second disadvantage is that the length of the crack tip element affects the result. Therefore, the length of the quarter point element has to be adjusted until the desired accuracy is achieved. Due to these disadvantages, this method is not implemented here.

The second method to determine the stress intensity factors is based on their basic definitions; as the limit of the stress multiplied by the square root of the distance to the crack tip, for the stress ahead of the crack tip, at a distance of 0.2 of the crack length to 0.5 of the crack length, (See Eq. 2.3). In this method the stresses ahead of the crack tip, the tangential stresses and the shear stresses, are multiplied by the square root of $2\pi r$ and plotted versus r. Curves are then fitted

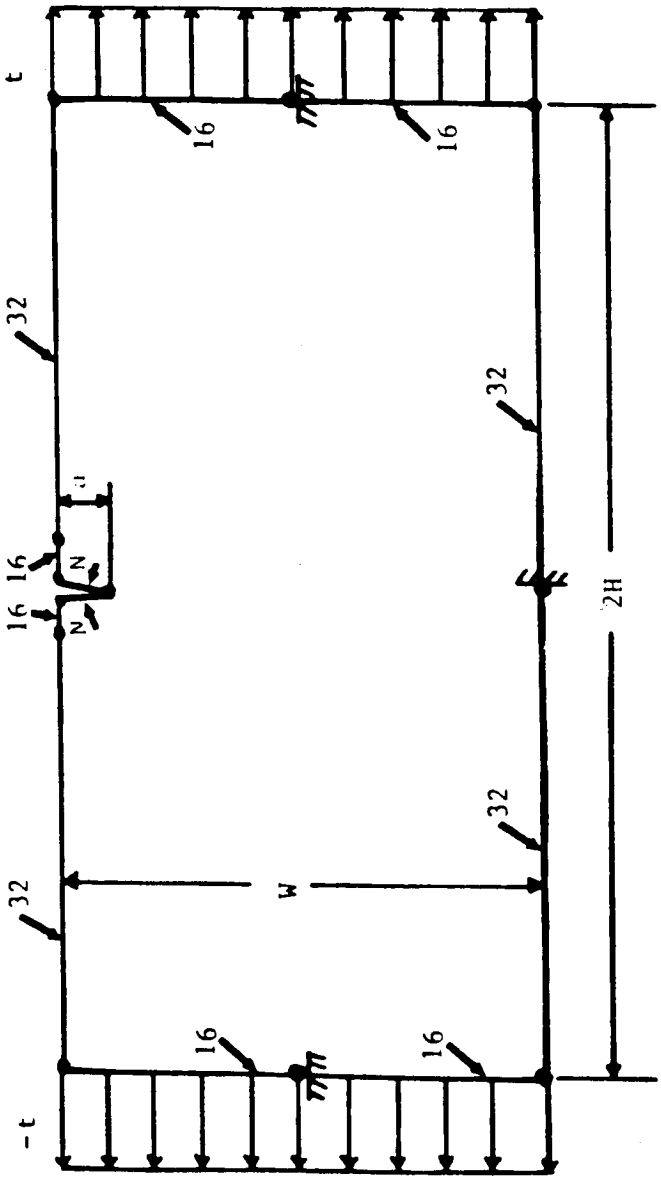

Fig. 3.9 Edge Crack in a Plate Under Uniform Tension t, with the Number of Nodes in Each Subdivision.

throught those points and the values at r = 0, equal the stress intensity factors, K_I and K_{II} respectively. This method is also known as the extrapolation method for determining the stress intensity factors.

Finally the J integral as defined in section 2.3 can be evaluated along any path around the crack tip, and the values of the resulting integrals are proportional to the stress intensity factors. The extrapolation method and the J integral method are compared next for a single edge crack under mixed-mode loading condition.

The single edge crack under uniform tensile load is analyzed first, with dimensions a/H = 1/15 and W/H = 1, where a is the crack length see Fig. 3.9. The tensile stress, t, is normalized with the modulus of elasticity E, t/E = 1. The number of nodes in each subdivision are shown in Fig. 3.9. The number of nodes, N, along the crack, is varied between 20 and 140. The mode I stress intensity factor, K_I, was calculated using the extrapolation method using internal points ahead of the crack tip between 0.2a and 0.5a. For points closer than 0.2a, the values of the stresses are not accurate. The variation of K_I with the number of nodes along the crack front is shown in Fig. 3.10. An asymptotic value for the stress intensity factor is reached for values of N greater than 100. Comparing the asymptotic value with the published solutions, Ref. [40], the difference between the two values is less than 1%. The J integral was also

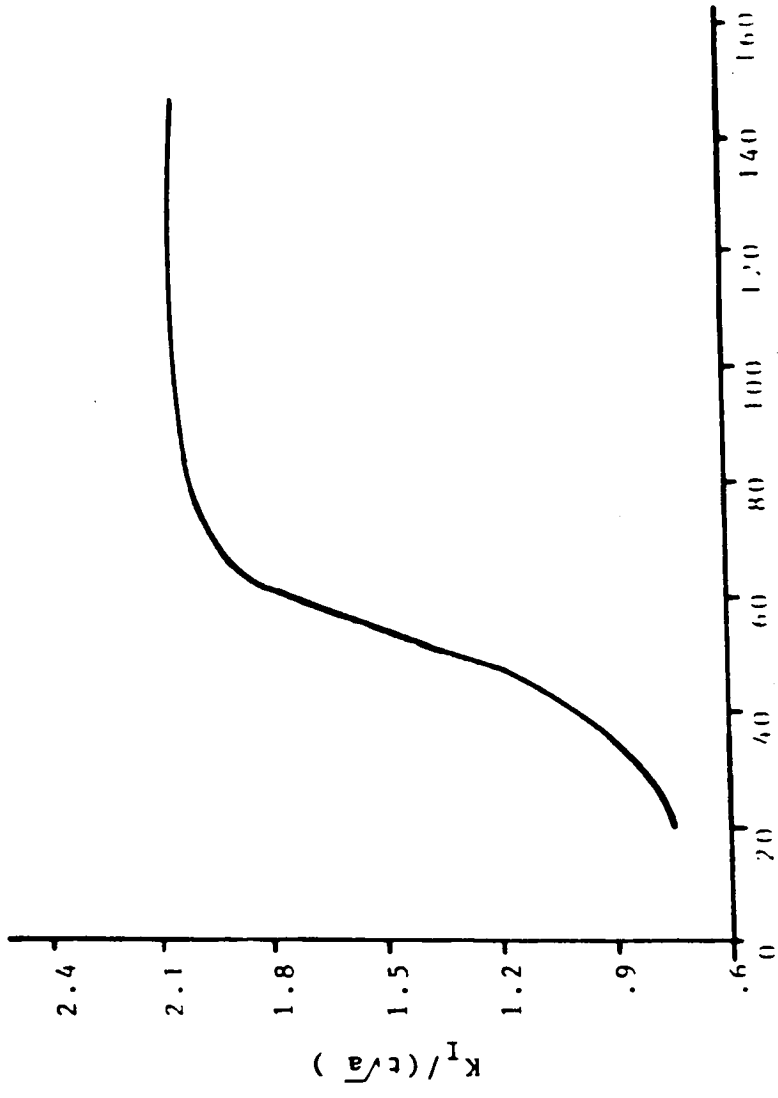

Fig. 3.10 Variation of the Mode I Stress Intensity Factor as a Function of the Number of Nodes, N, Along the Crack Front

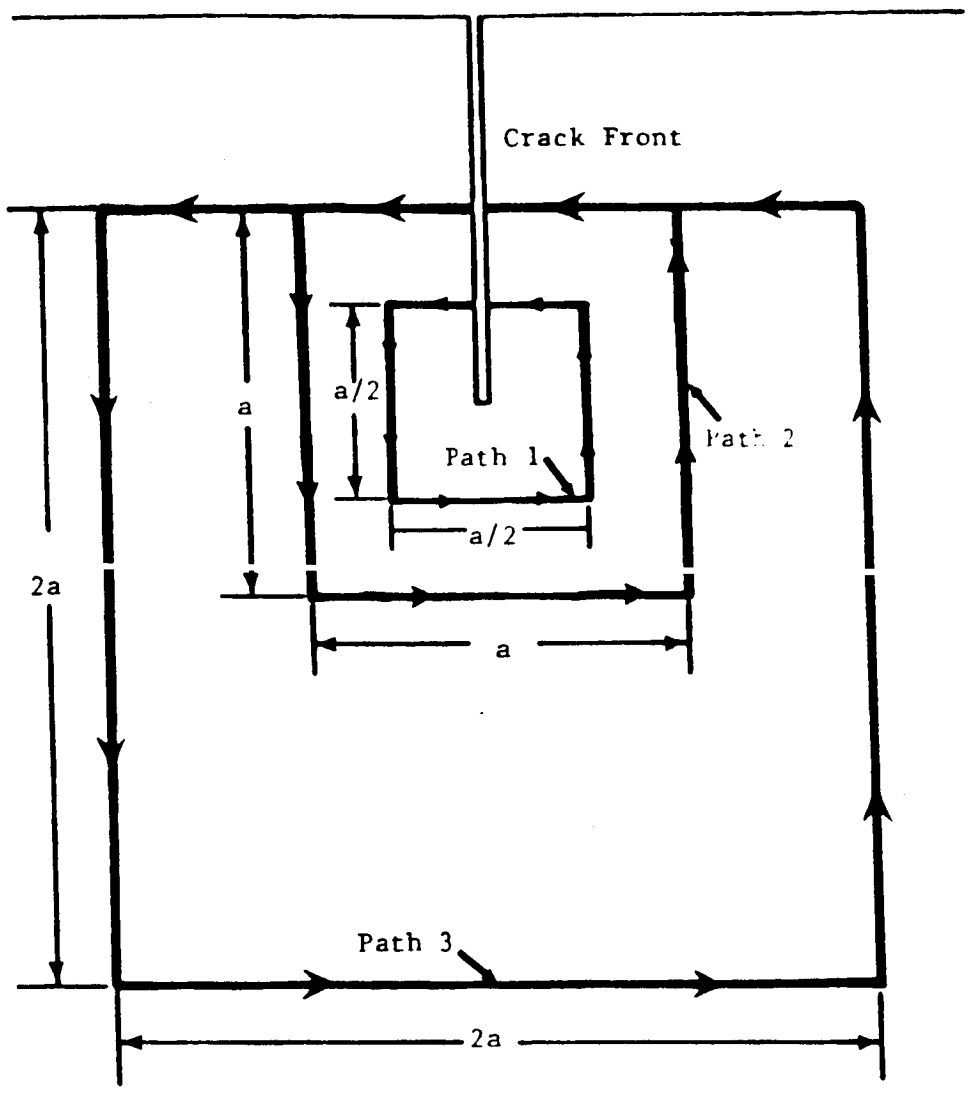

Fig. 3.11 The Three Paths Considered for the J Integral Calculations.

Table 3.2 Variation of the J integral and the Corresponding stress Intensity factor for different paths, for the Pure Mode I Loading Condition.

Path	$\frac{J_1 E}{t^2 a}$	$\frac{K_I}{t\sqrt{a}}$
	Eq. 2.13	Eq. 2.14
1	3.8052	2.045
2	3.8115	2.046
3	3.8146	2.047
extrapolation		2.045
Ref. [40]		2.032

calculated for N equals 100. Three different rectangular paths were chosen as shown in Fig. 3.11. To determine the values of $u_{i,1}$ in the J integral formulation, neighboring points were also used to determine numerically the values of the derivative of the displacement. The values of J integral for the corresponding paths are shown in Table 3.2, based on Eq. 2.13. Also shown is the corresponding mode I stress intensity factor using Eq. 2.14, and the results using the extrapolation method as well as the published solutions from Ref. [40]. As seen from Table 3.2, the results of the three different paths agree well with each other and also give the same result as the extrapolation method. Thus, the J integral and the extrapolation method give the same value for the stress intensity factor for this pure mode I case.

The second example is for a plate with a crack under shear mode loading, pure mode II, see Fig. 3.12. The dimensions of the plate are the same as for the mode I case; a/H = 1/15, W/H = 1. Two antisymmetric uniform applied pressure loads are located at equal distance from the crack plane. The distance y_0 of the mid-positions of the pressure load to the crack plane equals 0.25a. The magnitude of the pressure P applied equals 50E, and acts on a segment of length equals 0.01a. The variations of the mode II stress intensity factor as a function of the number of nodes along the crack front, using the extrapolation method, is shown in Fig. 3.13. An asymptotic value for the mode II stress intensity factor is reached at values of N greater than 100. The

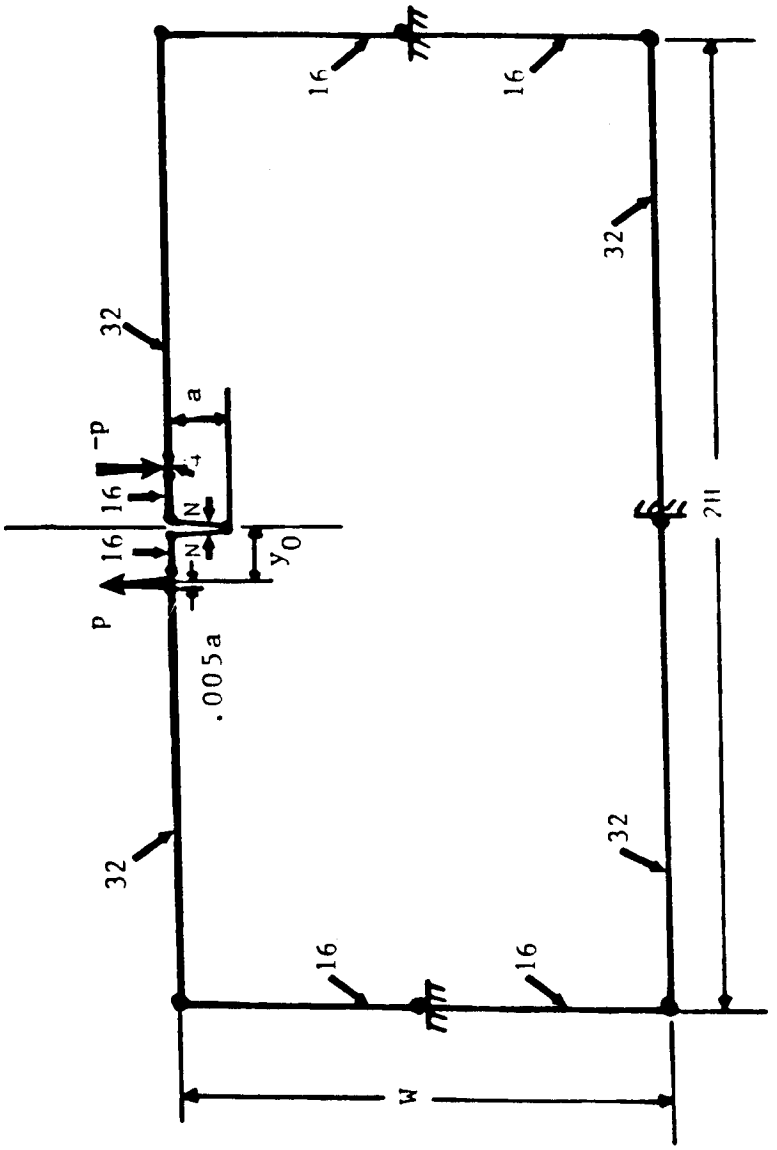

Fig. 3.12 Edge Crack in a Plate Under Pure Mode II Loading Condition.

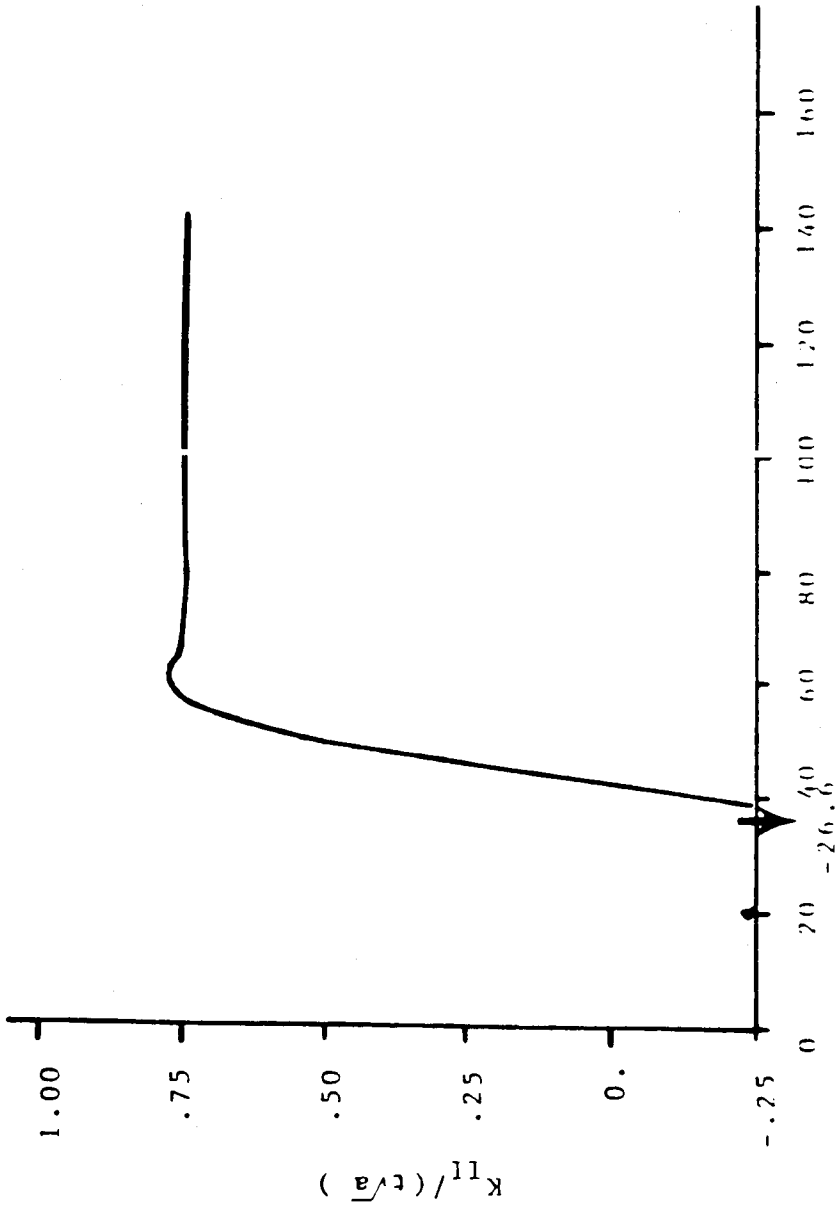

Fig. 3.13 Variation of the Mode II Stress Intensity Factor as a Function of the Number of Nodes N, Along the Crack Front, (p/t=50)

J integral method was also calculated using both formulations as describe in section 2.3, Rice formulation Eq. 2.13 and Bui formulation Eq. 2.16, for N = 100. For Bui's formulation the stresses and the displacements along any path had to be devided into symmetric and antisymmetric parts:

Displacements:

$$\begin{bmatrix} u^{I}_{x} \\ u^{I}_{y} \end{bmatrix} = 1/2 \begin{bmatrix} u_x + u'_x \\ u_y - u'_y \end{bmatrix} \quad \text{Symmetric}$$

$$\begin{bmatrix} u^{II}_{x} \\ u^{II}_{y} \end{bmatrix} = 1/2 \begin{bmatrix} u_x - u'_x \\ u_y + u'_y \end{bmatrix} \quad \text{Antisymmetric}$$

Stresses:

$$\begin{bmatrix} \sigma^{I}_{xx} \\ \sigma^{I}_{yy} \\ \sigma^{I}_{xy} \end{bmatrix} = 1/2 \begin{bmatrix} \sigma_{xx} + \sigma'_{xx} \\ \sigma_{yy} + \sigma'_{yy} \\ \sigma_{xy} - \sigma'_{xy} \end{bmatrix} \quad \text{Symmetric}$$

$$\begin{bmatrix} \sigma^{II}_{xx} \\ \sigma^{II}_{yy} \\ \sigma^{II}_{xy} \end{bmatrix} = 1/2 \begin{bmatrix} \sigma_{xx} - \sigma'_{xx} \\ \sigma_{yy} - \sigma'_{yy} \\ \sigma_{xy} + \sigma'_{xy} \end{bmatrix} \quad \text{Antisymmetric}$$

where the ' indicates the component of the stress or the displacement at the opposite position, with respect to the crack plane, of the point under considreration, see Fig. 3.11. Table 3.3 represents the values of the J integrals for the two formulations: Rice (J_1, J_2) and Bui (J_I, J_{II}), along the three paths given in Fig. 3.11 for the pure mode II example.

Table 3.3 Values of the J integral for the Three Paths, for the Pure Mode II loading Condition, (p/t = 50).

	Rice		Bui	
Path	$\frac{J_1 E}{t^2 a}$	$\frac{J_2 E}{t^2 a}$	$\frac{J_I E}{t^2 a}$	$\frac{J_{II} E}{t^2 a}$
	Eq. 2.13		Eq. 2.16	
1	0.40877	0.00	0.00525	0.40353
2	0.44304	0.00	0.00168	0.44217
3	0.39522	0.00	0.00074	0.39449

Table 3.4 Values of The Corresponding Mode II Stress Intensity from the J Integral Calculations, and the Value from Extrapolation method, (p/t = 50).

	Rice		Bui	
Path	$\frac{K_I}{t\sqrt{a}}$	$\frac{K_{II}}{t\sqrt{a}}$	$\frac{K_I}{t\sqrt{a}}$	$\frac{K_{II}}{t\sqrt{a}}$
	Eq. 3.23		Eq. 3.24	
1	0.00	0.6702	0.07596	0.6659
2	0.00	0.6978	0.04297	0.6971
3	0.00	0.6590	0.02852	0.6584
extrapolation			0.00	0.7414

The values of the corresponding stress intensity factors are determined using the following relations:

For Rice J integral:

$$K_I^2 = 2\,E\,\left(J_1 + \sqrt{J_1^2 - J_2^2}\right) / \{(1+\nu)(\kappa+1)\}$$

$$K_{II}^2 = 4\,E\,J_1 / \{(1+\nu)(\kappa+1)\} - K_I^2 \qquad 3.23$$

For Bui J integral:

$$K_I^2 = 4\,E\,J_I / \{(1+\nu)(\kappa+1)\}$$

$$K_{II}^2 = 4\,E\,J_{II} / \{(1+\nu)(\kappa+1)\} \qquad 3.24$$

where ν is the poisson's ratio and κ is as defined earlier equals $(3-4\nu)$ for plane strain condition.

The corresponding values of the stress intensity factors from the J integral results are shown in Table 3.4, using relations 3.23 and 3.24, for Rice and Bui formulation, respectively. Also shown, the mode II stress intensity factor using the extrapolation technique. Both J integral formulations gave consistent results, which are on the average 9% below the extrapolation result. But looking at the results for different paths, the value of K_{II} changes by almost 5% between each path. The difference between the two J integral formulations is not yet

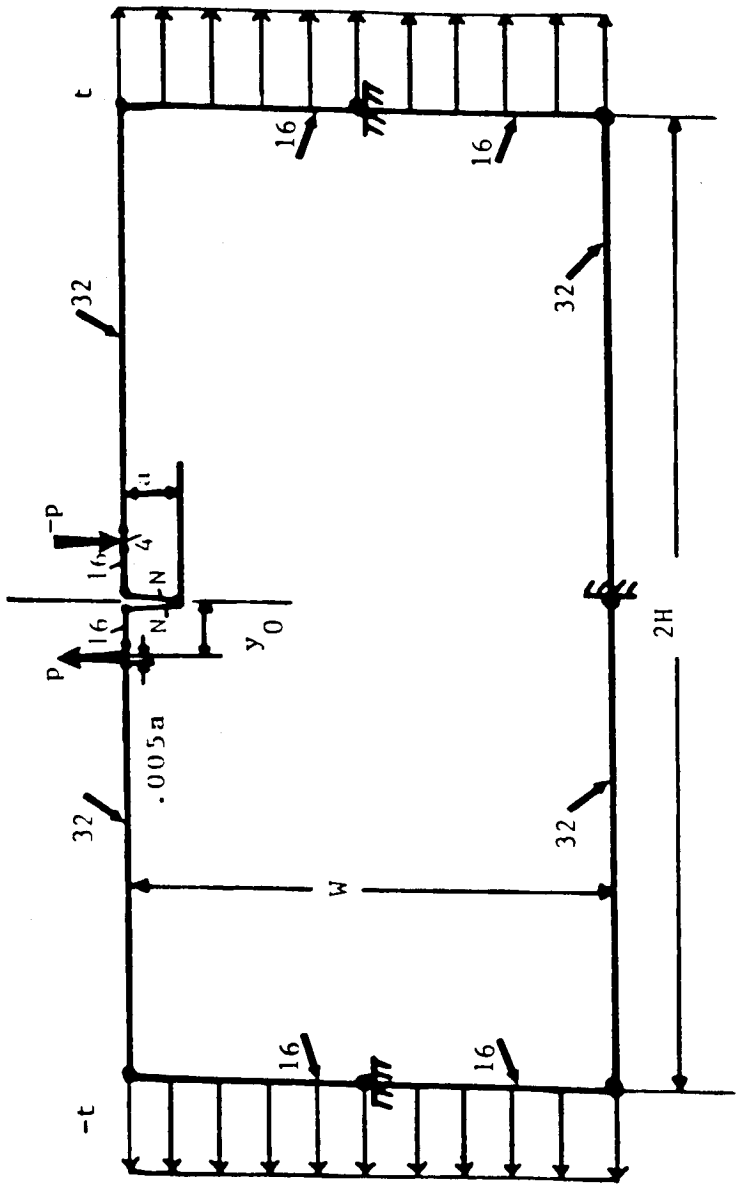

Fig. 3.14 Mixed Mode Loading Condition for an Edge Crack in a Plate, (P/t = 50).

obvious until the mixed-mode loading condition is analyzed.

For the mixed-mode loading condition, both cases analyzed above are combined together, see Fig. 3.14. The same dimensions and loading conditions are implimented in this example. Table 3.5 summurizes the values of the J integrals from both formulations for this mixed-mode loading condition. Also shown are the corresponding stress intensity factors using Eq. 3.23 and Eq. 3.24 for Rice and Bui formulations, respectively, along the same three paths described above, see Fig. 3.11. While Bui's formulation gives consistent results with the pure mode cases, Rice's formulation gives completely different answers, especially for the K_{II} stress intensity factor. A 33% difference in the value of the mode II stress intensity factor is observed, between the pure mode II and the mixed-mode case. This drop in the value of K_{II} is due to the incorrect J_2 integral formulation as discussed by Bui, Ref. [22]. Comparing the values of the mode II stress intensity factor between different paths, there is a 11% change in the J_2 between path 1 and path 3. The values of the stress intensity factors, K_I and K_{II}, from the extrapolation method are exactly equal to the pure mode results.

Due to the above controversy, the extrapolation method is used in the application of the BIEM to mixed-mode failure of the inner raceway of the high speed bearings.

Table 3.5 Values of The J Integral Results with the Corresponding Stress Intensity Factors, for the Mixed-Mode Loading Condition, (p/t = 50).

	Rice		Bui	
Path	$\frac{J_1 E}{t^2 a}$	$\frac{J_2 E}{t^2 a}$	$\frac{J_I E}{t^2 a}$	$\frac{J_{II} E}{t^2 a}$
	Eq. 2.13		Eq. 2.16	
1	4.1986	1.8082	3.7951	0.4135
2	4.2400	1.7836	3.7979	0.4422
3	4.1938	1.6154	3.7993	0.3945
	$\frac{K_I}{t\sqrt{a}}$	$\frac{K_{II}}{t\sqrt{a}}$	$\frac{K_I}{t\sqrt{a}}$	$\frac{K_{II}}{t\sqrt{a}}$
	Eq. 3.23		Eq. 3.24	
1	2.0950	0.4742	2.0422	0.6659
2	2.1079	0.4649	2.0429	0.6971
3	2.1049	0.4217	2.0433	0.6584
extrapolation			2.0450	0.7414

CHAPTER FOUR

APPLIED LOADINGS ON THE INNER RACEWAY OF BEARINGS

As a first step towards attempting to determine the crack propagation rate and the time to failure of the high speed bearings, the loading acting on the inner raceway should be determined. The most important loadings are the tangential stresses due to the rotational speed and the press fit, and the next important loadings are the Hertzian stresses, which alter the tangential stresses with each passage of the heavily loaded roller.

4.1 Tangential Stresses

The tangential stresses in the inner raceway are due to the rotational speed and the press fit of the inner raceway on to the shaft. Fig. 4.1 shows a simplified bearing configuration mounted on a hollow shaft. The solutions of the tangential stress in the inner raceway, modelled as a rotating disk is found to be, from Ref. [41]:

$$\sigma_{\theta\theta}=\left\{(3+\nu)/8\right\}\ \rho\omega^2[r_i^2+r_o^2+r_i^2r_o^2/r^2-\left\{(1+3\nu)/(3+\nu)\right\}\ r^2] \quad 4.1$$

where ρ is the density of the material, ω is the rotational speed

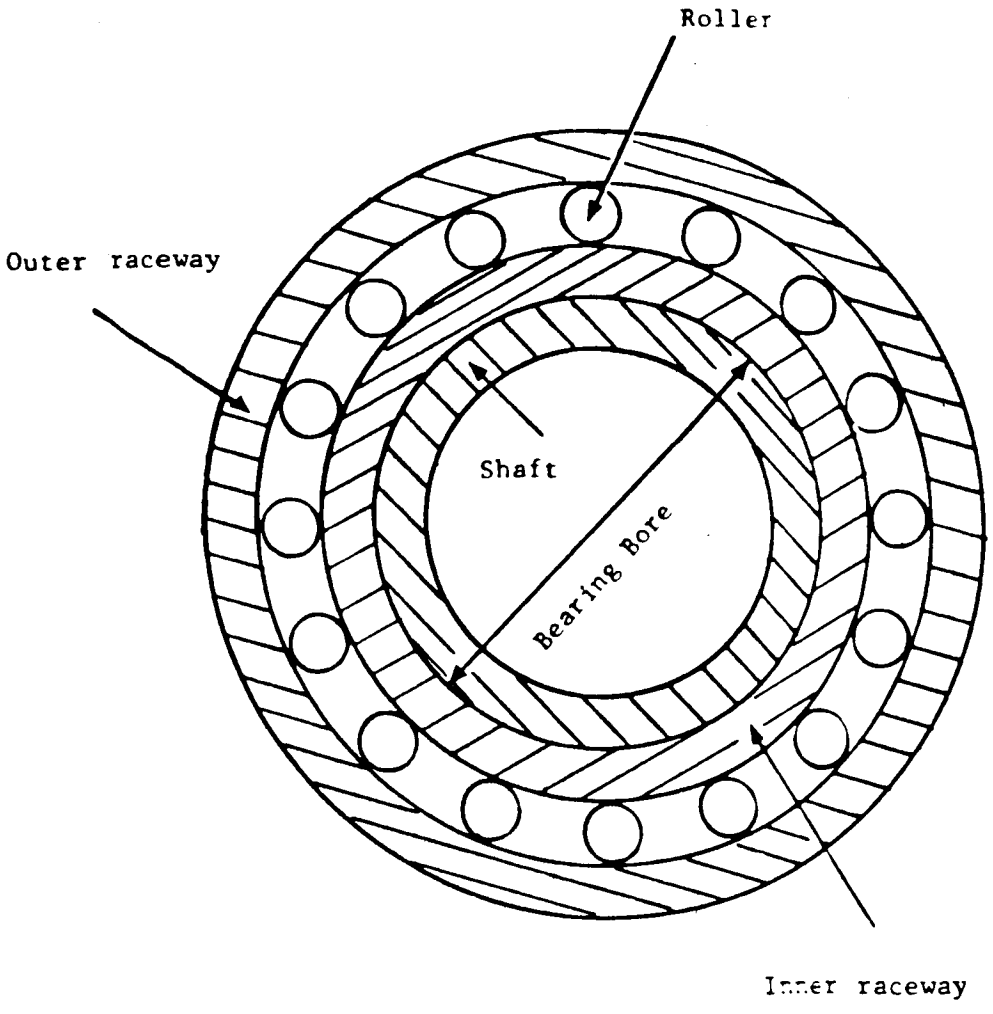

Fig. 4.1 A Simplified Bearing Configuration.

and r is the radial distance, and r_i and r_0 are the inner and outer radii of the rotating disk. The most critical point for surface initiated crack propagation is at the outer radius of the raceway, $r = r_o$. Substituting the value of r_0 for r in Eq. 4.1, the tangential stress at $r = r_o$ equals:

$$\sigma_{\theta\theta} = \left\{(3+\nu)/4\right\} \rho\omega^2 [r_i^2 + \left\{(1-\nu)/(3+\nu)\right\} r_o^2] \qquad 4.2$$

For typical aircraft engine bearings the ratio between the outer radius to the inner radius of the inner raceway equals 1.13, Ref. [42]. Subtituting the value of r_0 as a function of the inner radius of the raceway, r_i, and making use of the DN value, which is the product of the bearing bore in millimeter times the shaft rotating speed in RPM. The tangential stress at the outer radius will have the following relation assuming a poisson's ratio of 0.3:

$$\sigma_{\theta\theta} = 3.32075 \times 10^{-9} (DN)^2 \qquad \text{(psi)} \qquad 4.3$$

where the density ρ is assumed to equal 0.288 lb/in^3. A plot of the tangential stress versus the DN value is shown in Fig. 4.2. Also shown is an estimated critical crack length required for unstable crack growth. This estimate is derived for an edge crack in a semi-infinite plate with an applied normal stress equal to the tangential stress at the outer radius of the inner

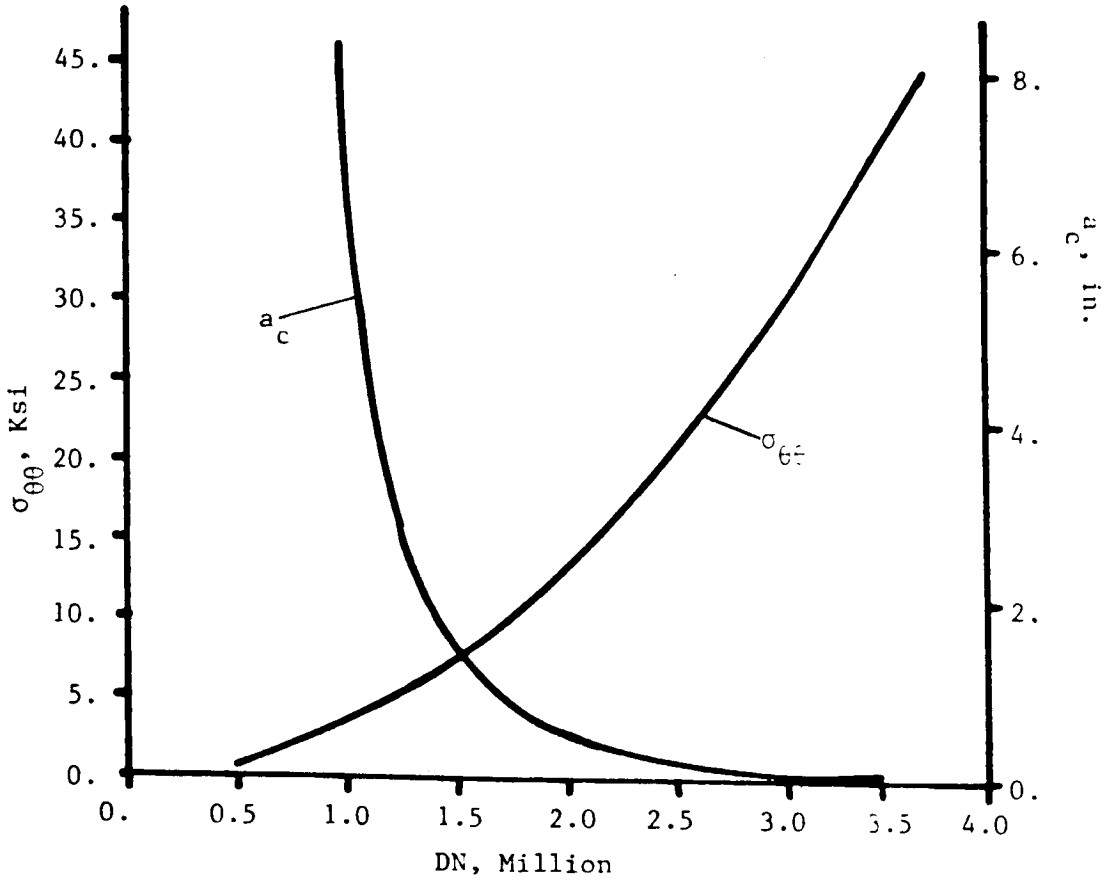

Fig. 4.2 Tangential Stress in the Inner Raceway and Critical Crack Length versus DN Value in Million

raceway.

$$K_{Ic} = 1.12\ \sigma_{\theta\theta}\sqrt{a_c \pi} \qquad 4.4$$

where the value of K_{Ic} is the critical stress intensity factor for unstable crack growth. The value of K_{Ic} used is equal to 17.5 Ksi$\sqrt{in}$, which is a typical critical stress intensity factor for M50 bearing steel. As seen from the equation, the critical crack length is inversly proportional to the fourth power of the DN value:

$$a_c = 7.047 \times 10^{24}\ (DN)^{-4} \qquad (in) \qquad 4.5$$

The critical crack length required for unstable crack growth decreases rapidly for DN values greater than 1.5 million. For a DN value equals 3 million, the critical crack length is almost 1/3 of the total raceway thickness. However, the effect on this critical crack length due to the press fit of the inner raceway onto the shaft ring should be estimated.

The effect of the press fit is to increase the tangential stresses in the inner raceway causing the critical crack length to decrease. A typical interference fit of the inner raceway on the shaft is 0.00233 in (0.059 mm) at 0 RPM, Ref. [42], causing a uniform pressure p = 1,974 psi along the interference radius, for two cylinders having the following dimensions; r_o = 2.6 in, r_i =

2.3 in and $r'_o = 2.3023$ in, $r'_i = 2.0$ in. The tangential stress due to a uniform pressure distribution is given in Ref. [41]:

$$\sigma_{\theta\theta} = p\{ r_i^2/(r_o^2-r_i^2) \}[\ 1 + r_o^2/r^2\ ] \qquad 4.6$$

For $r_i = 2.3$ in and $r_o = 2.6$ in the tangential stress is equal to 16.178 ksi at $r = r_o$, the outer radius of the inner raceway. But at increasing RPM the interference fit is reduced due to the radial displacement caused by the centripetal acceleration. Thus, a reduced pressure will develop between the inner raceway and the shaft which causes the interference fit to decrease with increasing speed:

$$\delta_{new} = 0.00233 - 1.0463 \times 10^{-16} (DN)^2 \quad (in) \qquad 4.7$$

where δ_{new} is the new interference fit at a given DN value. The pressure that develops from this new interference fit, will cause a tangential stress at the outer radius of the inner raceway which is given as:

$$\sigma_{\theta\theta} = 16{,}178 - 7.265 \times 10^{-10} (DN)^2 \quad (psi) \qquad 4.8$$

The net tangential stress at the outer radius of the inner raceway of the bearing, will be the sum of the two stresses due to the rotational speed and the press fit at a given DN value,

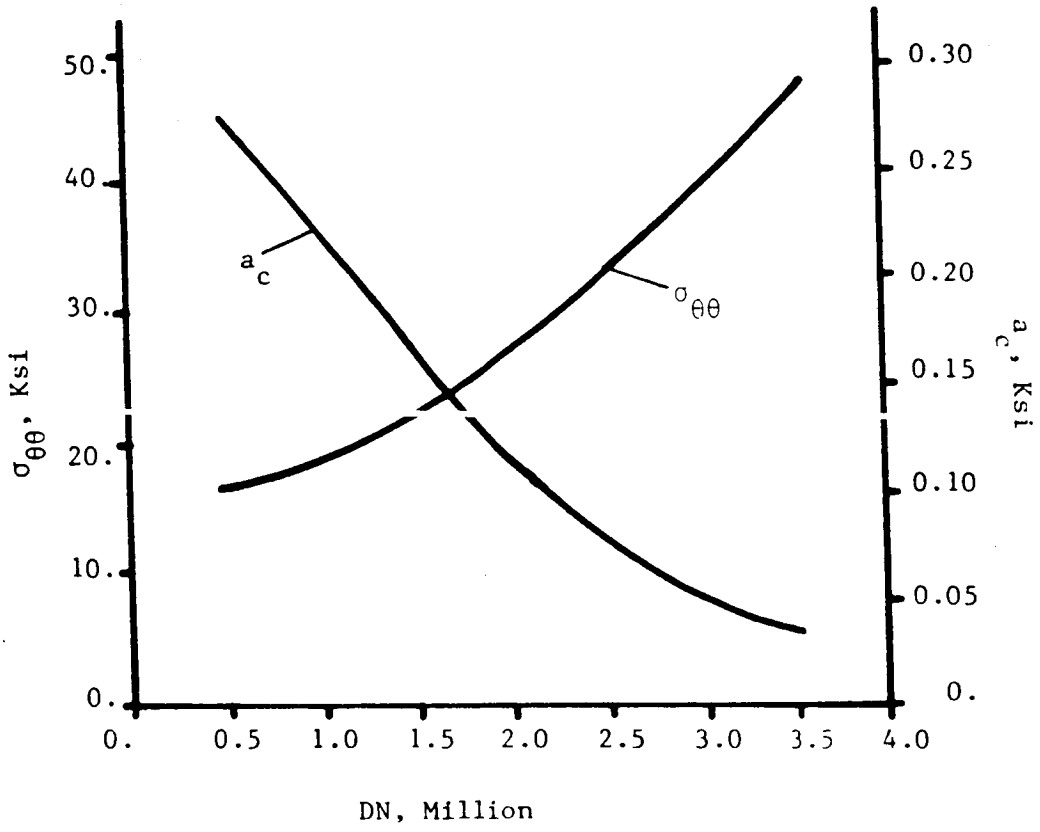

Fig. 4.3 Tangential Stress in the Inner Raceway due to the Press Fit and the Rotational Speed and Critical Crack Length versus DN Value in Million

given as the sum of Eq. 4.3 and 4.8:

$$\sigma_{\theta\theta} = 16,178 + 2.59425 \times 10^{-9} (DN)^2 \quad (psi) \qquad 4.9$$

and the critical crack length for the combined tangential stresses will be:

$$a_c = 7.77 \times 10^7 / (16,178 + 2.59425 \times 10^{-9} DN^2)^2 \qquad 4.10$$

A plot of the net tangential stress and the corresponding critical crack length acting at the outer radius of the inner raceway is shown in Fig. 4.3. The critical crack length calculated for a DN value of 3×10^6 is much than the defect depths which are of the order of 0.004 in. Thus, the only cause for the crack to grow from a small surface furrow or a debris dent is through a fatigue process developed by the alternating Hertzian stress.

4.2 Hertzian Pressure

When two bodies are in contact, special attention must be paid to the deformation in the contact region. The original analysis of elastic contact stresses under static loadings was published by Hertz in 1882 [43]. In his honor, the stresses at mating surfaces of curved bodies are commonly called Hertzian

stresses. The actual load-carrying capacity of bodies in contact depends upon more than the elastic stress computed from Hertz equations. Surface sliding, lubricating fluid films and surface roughness should also be considered. In this section only the elastic solution under ideal surface conditions is assumed.

Hertz's analysis showed that for two spherical bodies in contact the pressure distribution, which causes a uniform displacement field in the contact region, is represented by an elliptic pressure distribution, see Fig. 4.4, having the following equation:

$$p = p_0 \sqrt{1 - x^2/a^2 - y^2/b^2} \qquad 4.11$$

where p_0 is the maximum pressure at the center of the contact region, and a and b denote the major and minor semiaxes of the contact surface for two spherical bodies in contact. The total load applied will be equal to:

$$P = (2/3)\ \pi\ a\ b\ p_0 \qquad 4.12$$

For two cylindrical bodies in contact, (roller bearings), the major semi-axis, a, goes to infinity and the pressure distribution will have the following form, see Fig. 4.5:

$$p = p_0 \sqrt{1 - y^2/b^2} \qquad 4.13$$

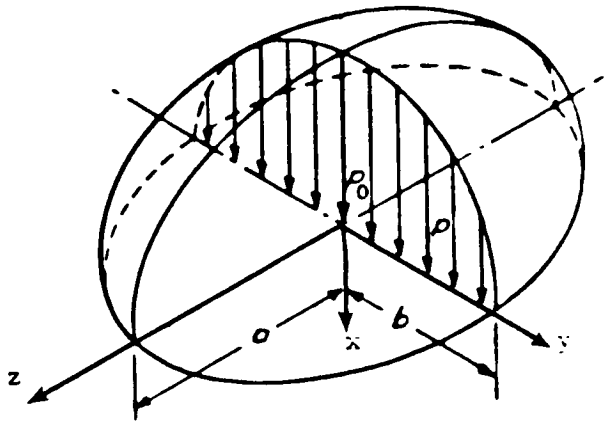

Fig. 4.4 Elliptic Pressure Loading for two Spheres in Contact.

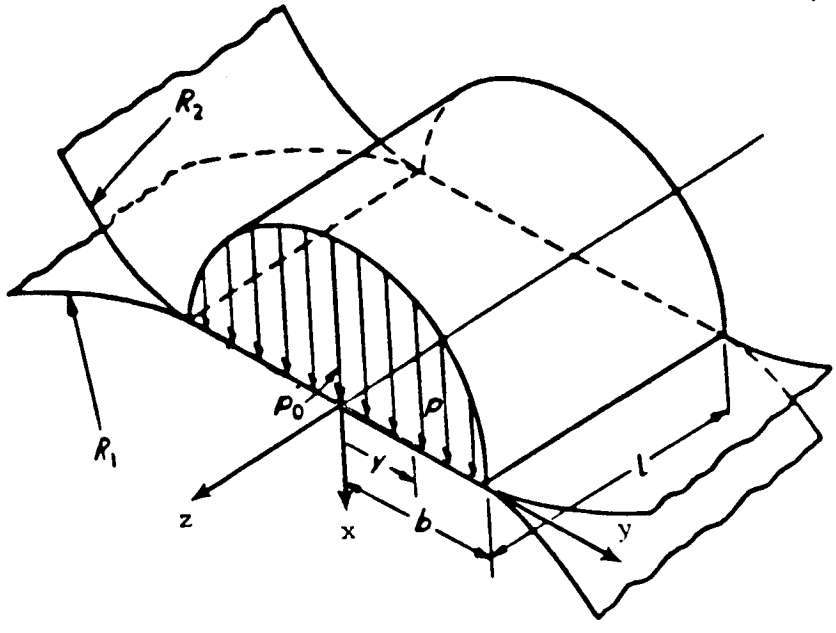

Fig. 4.5 Pressure Loading for Two Cylinders in Contact.

resulting in an applied total load which equals:

$$P = (1/2)\ \pi\, b\, L\, p_0 \qquad 4.14$$

where b is the minor semi-axis and L is the length of the roller bearing.

To determine the dimension of the minor semi-axis, b, of the contact region, the curvature and the material properties of the two cylinders in contact should be taken into consideration. Following Ref. [44], b equals:

$$b = 2\sqrt{\frac{P\,\left((1-\nu_1^2)\,/\,E_1 \;+\; (1-\nu_2^2)\,/\,E_2 \right)}{\pi\; L\;\left(1/r_1 + 1/r_2 \right)}} \qquad 4.15$$

where r_i, ν_i, and E_i are the radius of curvature, the poisson's ratio and the modulus of elasticity, respectively, for the two cylindrical bodies in contact.

When the applied load for a given bearing configuration is known, the Hertzian stresses in the bodies can be easily determined analytically or numerically. Smith and Liu, Ref. [44] solved for the stresses for a semi-infinite plate under a Hertzian pressure distribution using the integral equation technique. The stress distributions σ_x, σ_y, and σ_{xy} are given in Fig. 4.6, 4.7 and 4.8, respectively. Fig. 4.7 shows the variation of the tangential stresses with roller position. As the roller gets closer to the line under considerations, the

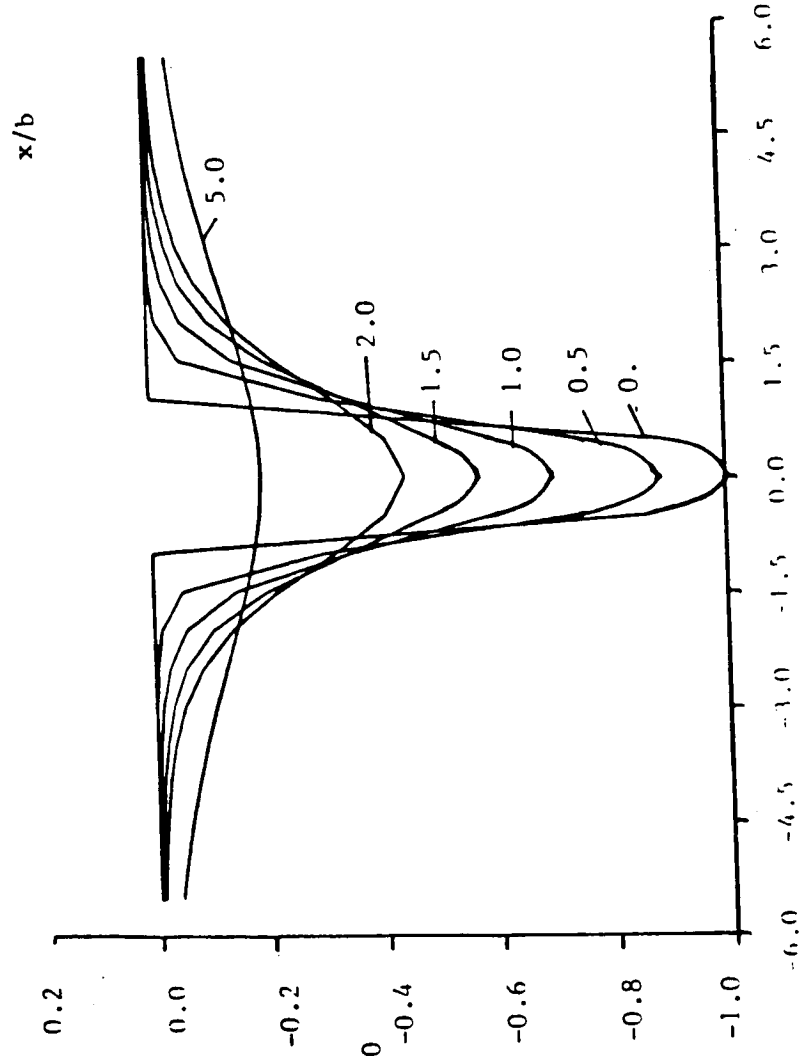

Fig. 4.6 Variation of σ_x as a function of the Roller Position for Different Depths x/b

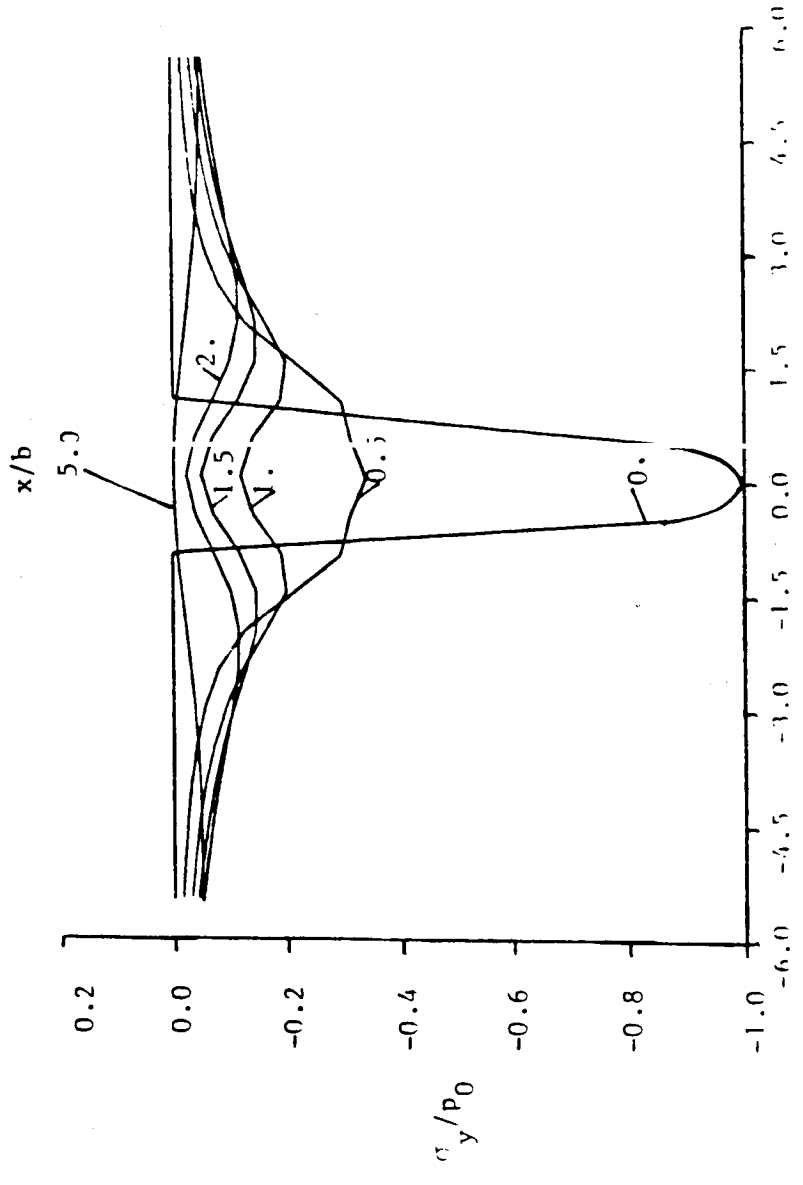

Fig. 4.7 Variation of σ_y as a Function of the Roller Position for Different Depths x/b

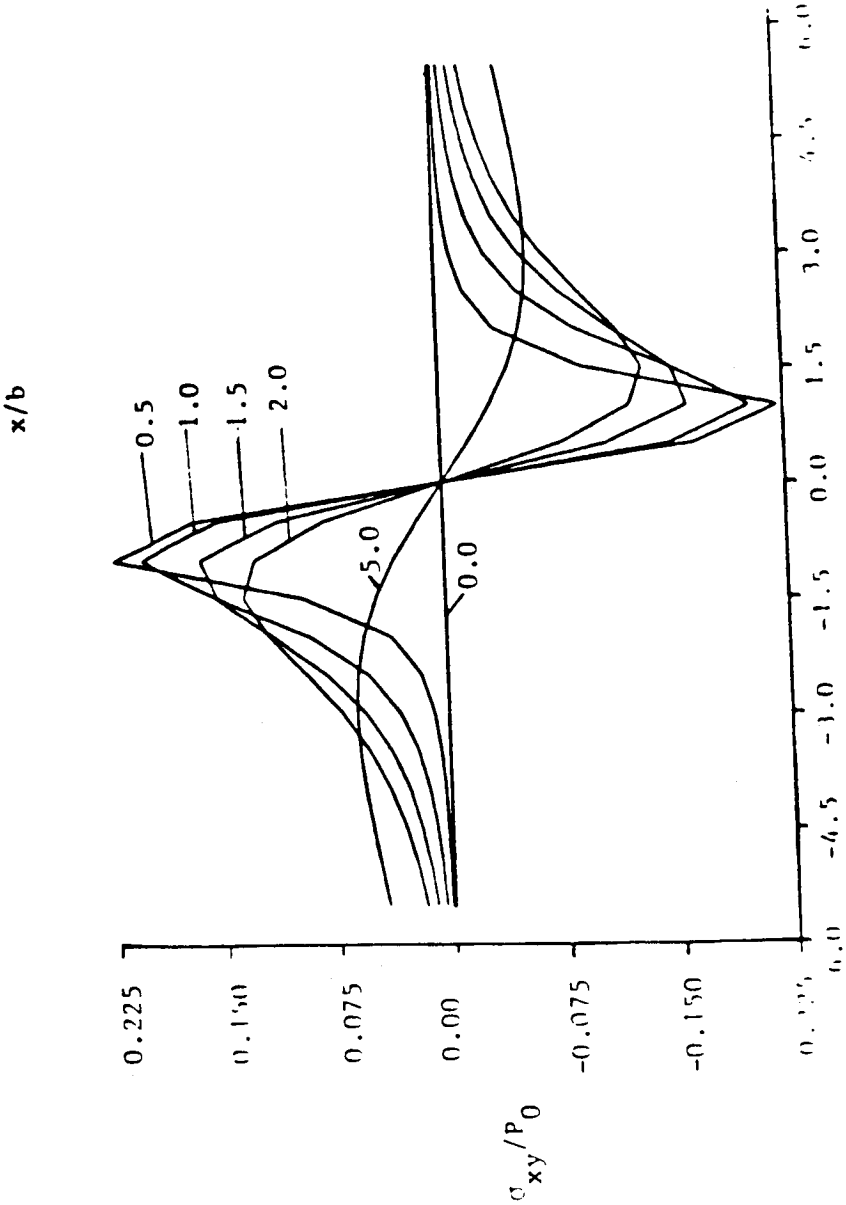

Fig. 4.8 Variation of σ_{xy} as a Function of the Roller Position for Different Depths x/b

stresses are highly compressive, and as the roller gets away the compressive stresses die out quickly. For a surface defect, this fast variations of the stress state superimposed on the tangential stresses due to the rotational speed and the press fit causes an alternating mode I stress intensity factor that can be a driving force for the fatigue crack growth.

The second crack propagation mode is the shear mode, as seen in Fig. 4.8. The shear stress increases as the roller gets closer to the line under considerations, reaches its maximum at the edge of the loading and then decreases quickly. While the normal stresses decay relatively fast for distances of x greater than 5b, the shear stresses still have some effect at greater depth.

Friction effect is sometimes superimposed on the normal Hertzian loadings for sliding contacts. The friction is usually represented as a fraction of the normal pressure acting in a direction opposite to the relative motion, given by Ref. [44]:

$$q = f\ p \qquad 4.16$$

where f is the coefficient of friction, and p in the normal Hertzian load. In general, in the absence of viscosity effects of the lubricant, friction changes little with speed. When viscosity effects comes into consideration, two types of behavior are observed; for mineral oils friction decrease with increasing

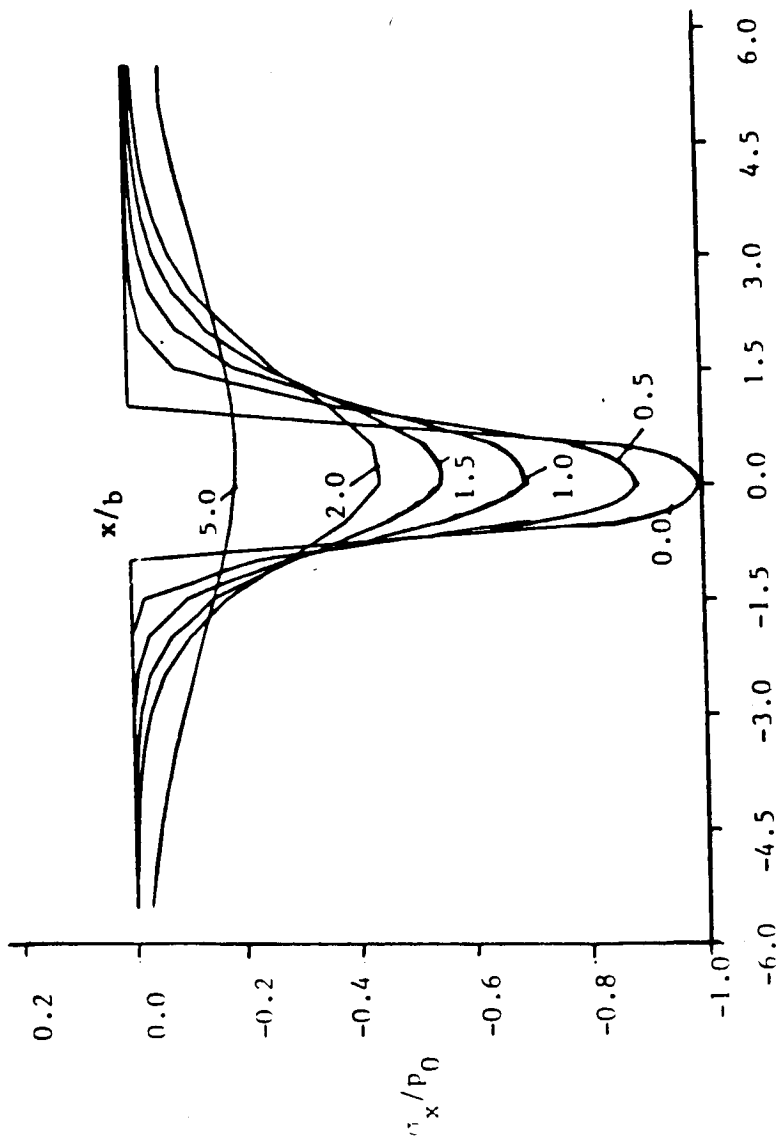

Fig. 4.9 Variation of σ_x as a Function of Roller Position for Different Depths x/b, when Friction is Present, (f=0.3)

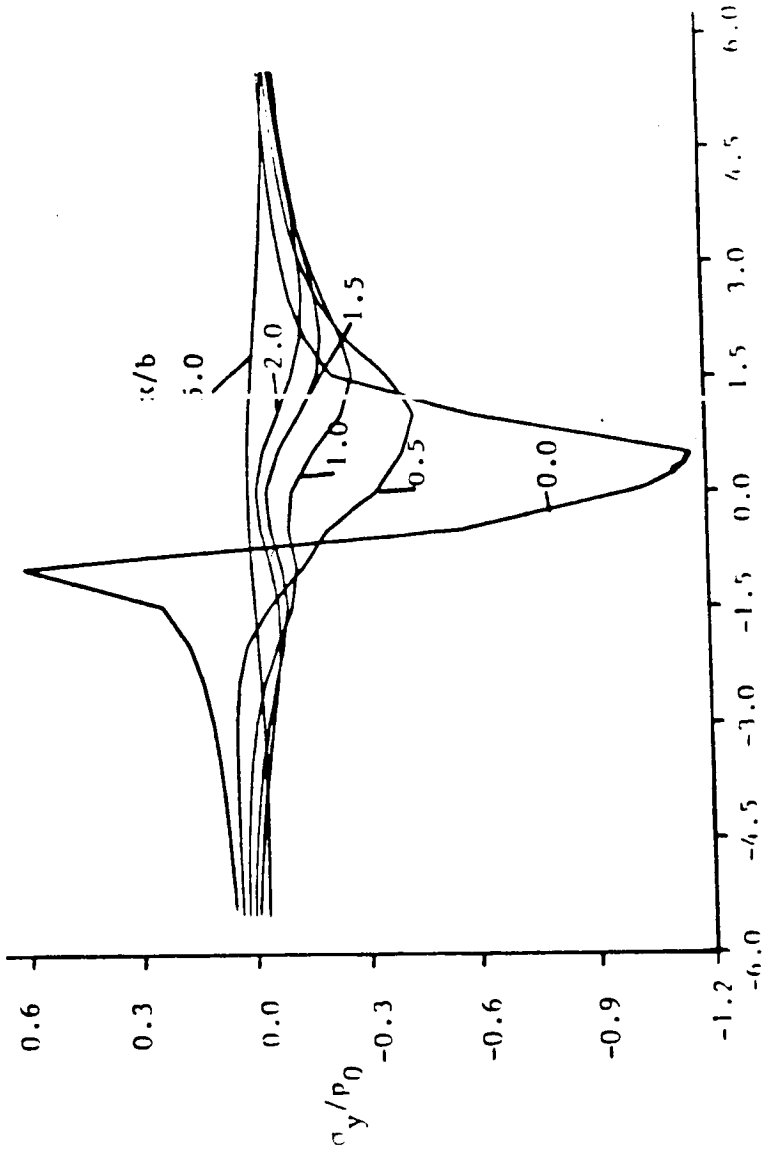

Fig. 4.10 Variation of σ_y as a Function of Roller Position for Different Depths x/b, when Friction is Present, (f=0.3)

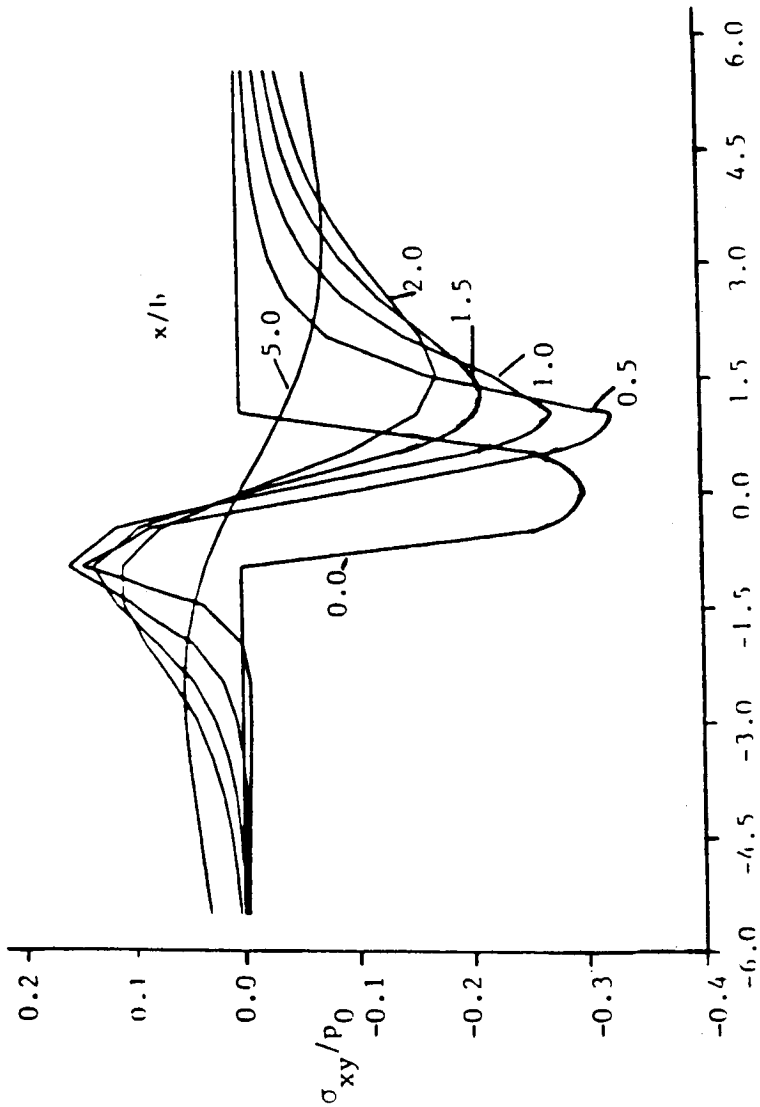

Fig. 4.11 Variation of σ_{xy} as a Function of Roller Position for Different Depths x/b, when Friction is Present, (f=0.3)

speed, while for fatty acids the opposite is observed. At high speed, increase in friction is normally observed, Ref. [45]. The variations of the stress distributions under the Hertzian pressure with friction are shown in Fig. 4.9, 4.10, 4.11, for σ_x, σ_y and σ_{xy} respectively. The friction coefficient, f, used in the calculation, equals 0.3. The net effect of the friction is to alter the symmetry of the normal Hertzian stress components; increasing the stress when the friction acts in the direction of the loadings and decreasing it for the other case. The most important change in the stress distribution is for σ_y, which becomes positive when the loading is on the left of the line under consideration. For the shear stress, the negative component of the stress distribution increases, while the positive component decreases, Fig. 4.11.

The next step in the analysis is to include the effect of the lubricating film since all high speed bearings are well lubricated.

4.3 Elastohydrodynamics Lubrication

For the completeness of the analysis the fluid film should be considered, in the presence of a surface defect or a surface furrow.

The governing equation for the elastohydrodynamic lubrication is based on Reynolds equation, which is a special case of

the Navier equation for fluid bodies. Assuming no side leakage, the two dimensional Reynolds equation is given by;

$$\frac{d}{dy}\left\{\frac{\rho h^3}{\eta}\frac{dp}{dy}\right\} = 12\, v\, \frac{d\rho h}{dy} \qquad 4.17$$

where ρ is the lubricant density

η is the lubricant viscosity

h is the film thickness

p is the pressure

v is the mean velocity of the lubricant $(v_1+v_2)/2$

The variation of the viscosity with pressure for liquids is:

$$\eta = \eta_0\, e^{\xi p} \qquad 4.18$$

where η_0 is the coefficient of the absolute viscosity at atmospheric pressure, and ξ is the pressure-viscosity coefficient of the fluid.

The density variation with pressure is:

$$\rho = \rho_0\, [\, 1 + ap/(1+bp)\,] \qquad 4.19$$

where ρ_0 is the density at atmospheric pressure, and where a and b are pressure-density coefficients.

The film thickness is given by:

$$h = h_0 + y^2/2 \quad (1/r_1+1/r_2) + u_x + d \qquad 4.20$$

where h_0 is the minimum film thickness, r_i are the radii of curvatures of the two bodies in contact, u_x is the total elastic deformation and d is the height of the surface defects in the contact region due to debris dents or surface furrows.

The solution to Reynolds equation, Eq. 4.17, with the given viscosity and density as functions of the pressure can only be obtained numerically. The numerical technique used here is the combination of the finite difference method for the solution of Reynolds equation and the boundary integral method for the displacement calculations.

Fig 4.12 shows the flow diagram for the numerical technique implimented. An initial pressure profile is assumed. Then, the displacements for the given pressure profile are solved for, using BIEM program. The film thickness h, from Eq. 4.20, is calculated next. The new pressure profile is now determined using the finite difference method. Due to the high gradients of dp/dy and d^2p/dy^2, a new smoother paramater, ϕ, is introduced, defined as:

$$\phi = p\, h^{3/2} \qquad 4.21$$

Note that p is small at large values of h and vice versa. This subsitution also has the advantage of eliminating all terms containing derivatives of h and p or h and ϕ. Therefore, the Reynolds equation in terms of the new paramter c will be:

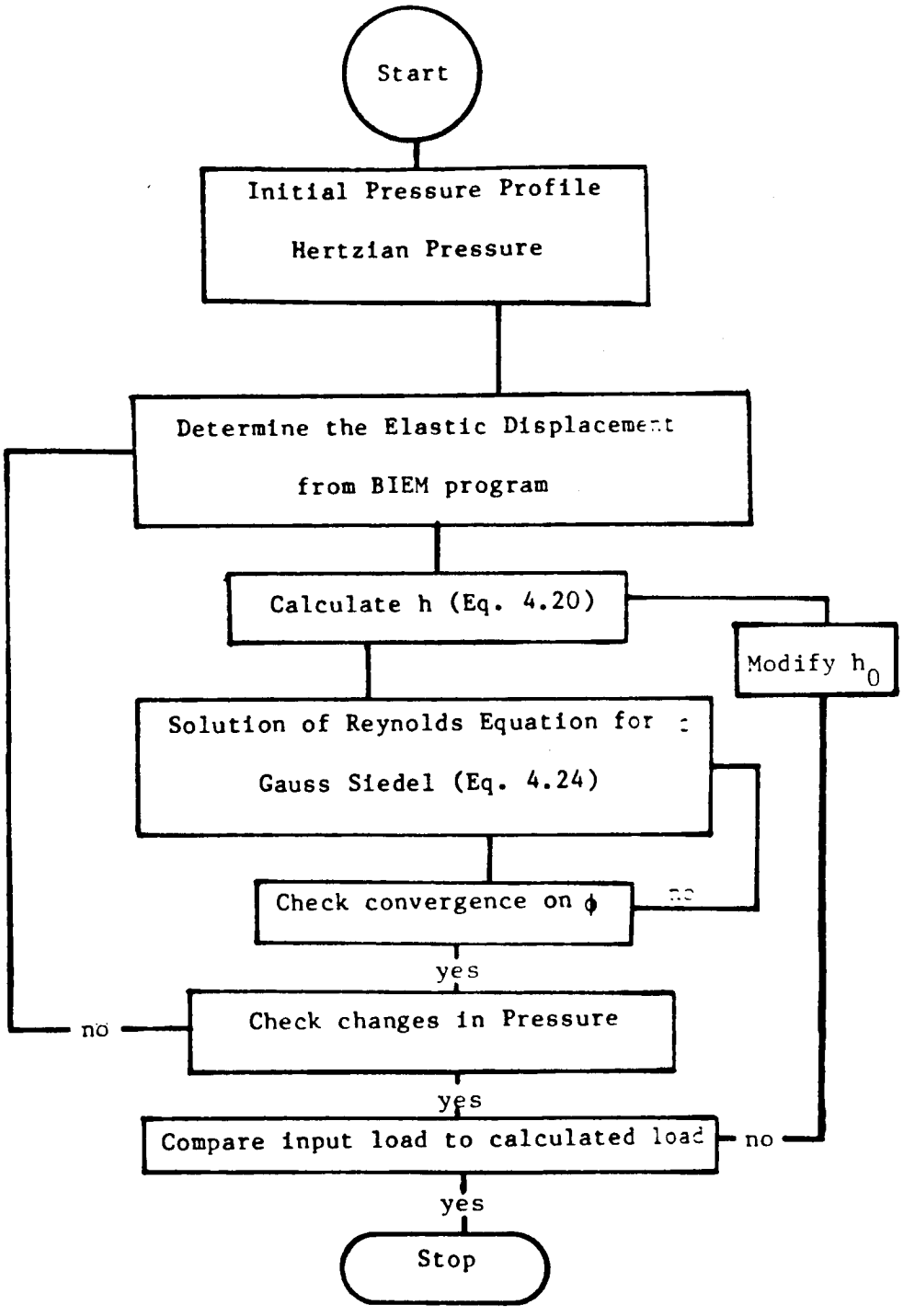

Fig. 4.12 Flow Diagram of the Elastohydrodynamic Lubrication Problem

$$h^{3/2}\frac{d}{dy}\left\{\frac{\rho}{\eta}\frac{d\phi}{dy}\right\} - \frac{3}{2}\phi\frac{d}{dy}\left\{\frac{\rho h^{1/2}}{\eta}\frac{dh}{dy}\right\} = 12\,u\,\frac{d\rho h}{dy} \qquad 4.22$$

Using standard finite difference representation, Eq. 4.22 can be rewritten as:

$$a_{1,i}\,\phi_{i-1} + a_{2,i}\,\phi_i + a_{3,i}\,\phi_{i+1} = b_i \qquad 4.23$$

where

$$a_{1,i} = \left.\frac{h_i^{3/2}}{d^2}\frac{\rho}{\eta}\right|_{i-1/2} \qquad a_{3,i} = \left.\frac{h_i^{3/2}}{d^2}\frac{\rho}{\eta}\right|_{i+1/2}$$

$$a_{2,i} = -\frac{h_i^{3/2}}{d^2}\left\{\left.\frac{\rho}{\eta}\right|_{i+1/2} + \left.\frac{\rho}{\eta}\right|_{i-1/2}\right\} - \frac{3}{2d}\left\{\left.\frac{\rho}{\eta}h^{1/2}\frac{dh}{dy}\right|_{i+1} - \left.\frac{\rho}{\eta}h^{1/2}\frac{dh}{dy}\right|_{i-1}\right\}$$

$$b_i = \frac{12\,u}{2\,d}\left\{\left.\rho h\right|_{i+1} - \left.\rho h\right|_{i-1}\right\} \qquad d = \text{nodal distance}$$

The system of equation of Eq. 4.23 is solved using the Gauss Siedel iteration method until ϕ does not vary. The relaxed Gauss Siedel method of iteration is given by:

$$(I + w\,a_2^{-1}\,a_1)\,\phi^{n+1} = \left\{(1-w)I - wa_2^{-1}\,a_3\right\}\phi^n + w\,a_2^{-1}\,b \qquad 4.24$$

where w is the relaxation coefficient. The Guass iteration will continue until ϕ does not vary.

The new pressure is calculated and compared with the

original pressure. If the difference is much bigger than a certain tolerance, a new displacement field will be calculated using the BIEM program. If not, the load generated from the pressure is measured and compared with the applied load required. If the two loads do not compare, a new film thickness h_0 is estimated and the calculation is repeated until convergence.

The boundary conditions for the Reynolds equation are:

1) $p = 0$, for regions far from the contact area

2) p is reset to zero at any position when the pressure is negative

The second condition is commonly known as the Reynolds condition, which is based on obervations that a negative pressure cannot exist in the contact region.

An initial run was performed using constant viscosity and density, with and without a surface furrow. The pressure profiles are shown in Fig. 4.13, for a defect depth equals 0.0030 in. and a Hertzian load of 1500lbs. The pressure distribution drecreases sharply at the tip of the defect and increases to the original pressure distribution after the defect. As the depth of the defect increases the pressure in the pocket decreases to zero. Therefore, one can assume that with the presence of the surface crack the pressure of the lubricant in the crack can be taken as zero.

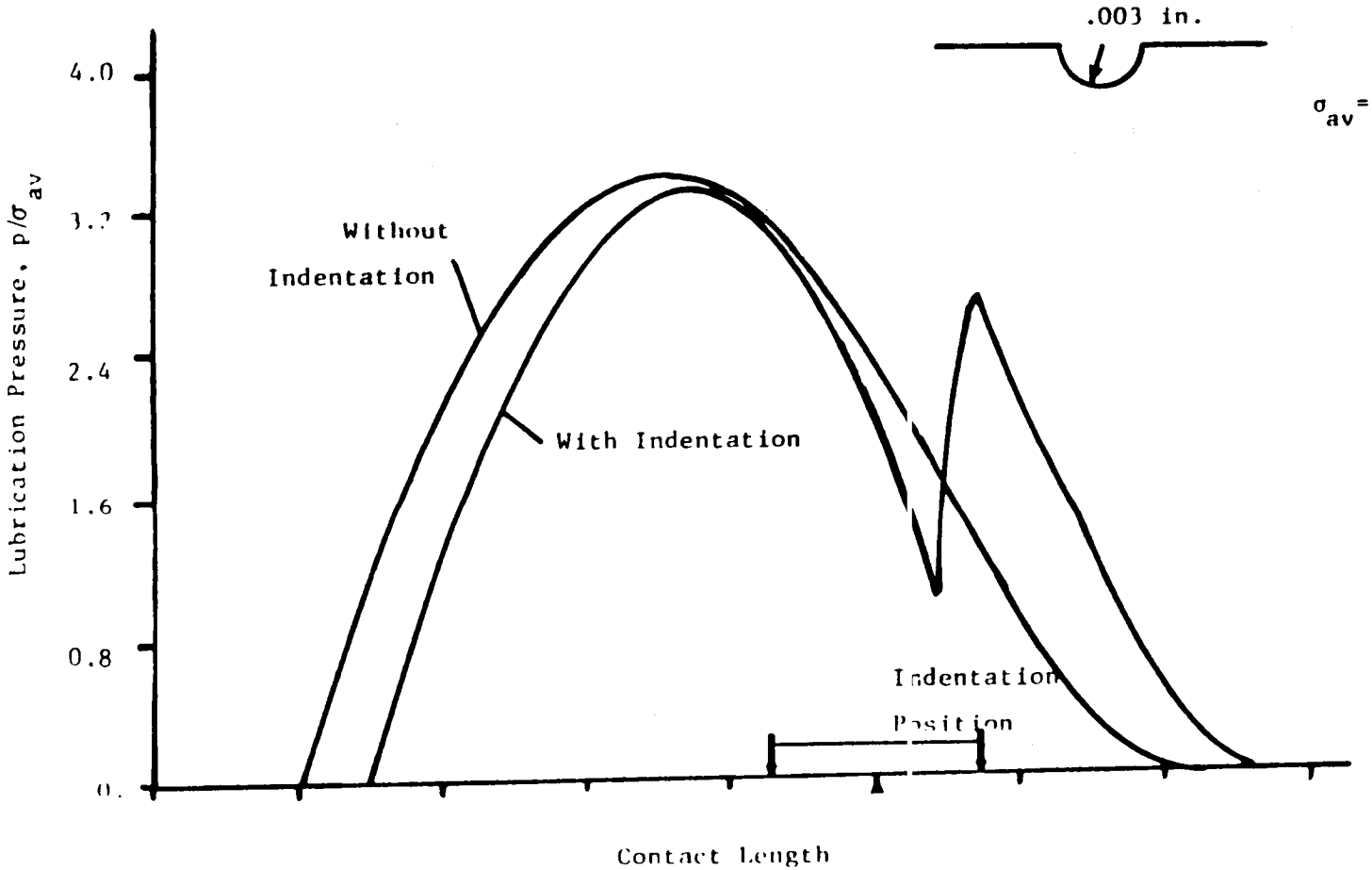

Fig. 4.13 Effect of a Semi-Circular Indentation of 0.003 in. Radius on the Hydrodynamic Pressure Profile

4.4 Initial Estimate of The Stress Intensity Factors

As a first estimate, the stress intensity factors, K_I and K_{II}, were evaluated using the superposition method. This method consists of evaluating the stresses in an uncracked body and then applying the negative of the stresses for the uncracked body along the crack faces of the cracked body to determine the stress intensity factors. Fig. 4.14 represents a schematic diagram of the superposition method used. Fig. 4.14.a shows a cracked plate with the tangential stresses and the Hertzian loading. This is equated to the sum of a plate with the same loading conditions but without a crack, Fig. 4.14.b. and a cracked plate loaded only along the crack faces with the negative stresses of the uncracked case. The stress intensity factors are then determined by summing the effect of every point load using available solutions. The stress intensity factors are given by:

$$K_I = 2/\sqrt{a\pi}\int \sigma_{xx}/\sqrt{(1-(x/a)^2)}\quad F(x/a)\,dx$$

$$K_{II} = 2/\sqrt{a\pi}\int \sigma_{xy}/\sqrt{(1-(x/a)^2)}\quad F(x/a)\,dx \qquad 4.25$$

where F(x/a) is given in Fig. 4.15 from Ref. [40], for a point load along the crack faces at distance x from the crack tip. The stresses used in this superposition method were the tangential stresses due to the press fit and the rotational speed combined

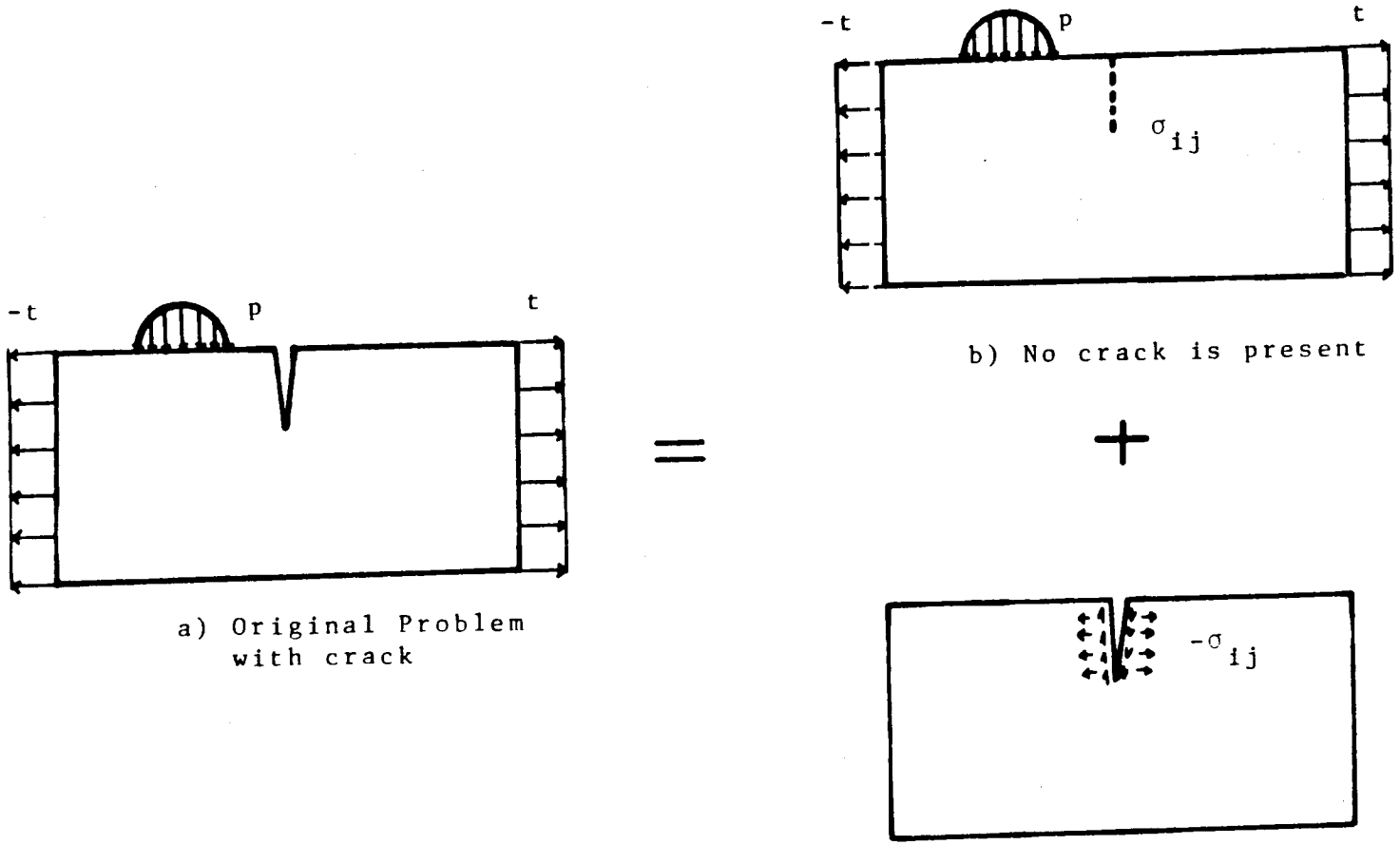

a) Original Problem with crack

b) No crack is present

c) Negative of the Stresses Applied along the crack

Fig. 4.14 Superposition Principal

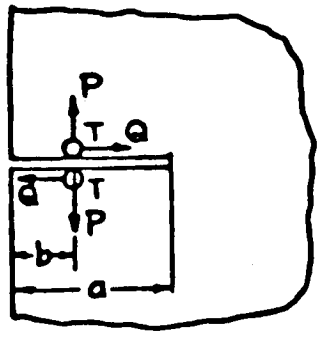

$$\begin{Bmatrix} K_I \\ K_{II} \\ K_{III} \end{Bmatrix} = \frac{2}{\sqrt{\pi a}} \begin{Bmatrix} P \\ Q \\ T \end{Bmatrix} \frac{1}{\sqrt{1-(b/a)^2}} \begin{Bmatrix} F(b/a) \\ F(b/a) \\ 1 \end{Bmatrix}$$

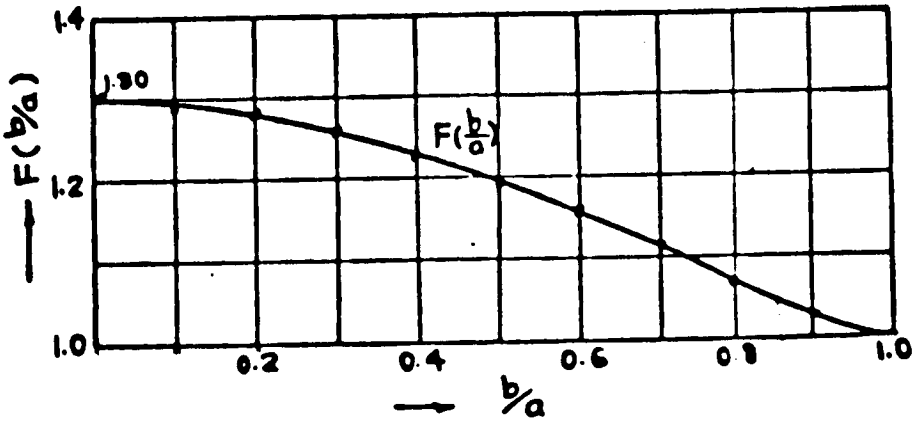

Fig. 4.15 Solution for the stress intensity factors for a point load on the crack face. Ref. [40].

with the Hertzian stresses for a given roller position and crack length.

Fig. 4.16 represents the variation of the mode I stress intensity factor as a function of the roller position for different crack lengths, a/b. The value of the maximum Hertzian pressure, p_0, used in this example, equals 180ksi, with a semi-major axis, b, equals 0.005 in. The change in the K_I stress intensity factor decreases with increasing crack depth a. For small crack depths K_I is negative, indicating crack closure, due to the high compressive Hertzian stresses. The variation of the mode II stress intensity factor with roller position is shown in Fig. 4.17 for different maximum Hertzian pressures p_0. The variation of the maximum K_{II} stress intensity factor with crack depth for p_0 equals 180ksi is shown in Fig. 4.18. The maximum mode II stress intensity factor increases sharply for small crack depths, reaches a maximum value, and then decreases slowly as the crack depth increases. These results show the variation of the stress intensity factors with each passage of a roller. As seen from the figure, the stress intensity factors are well below the critical stress intensity factor, K_{IC}, of M50 bearing steel, for a crack depth less than 0.06 in. Therefore, the only criteria for the failure of the inner ring from a very small surface defect is through a fatigue process due to the combined alternating stress intensity factors, ΔK_I and ΔK_{II}, as shown in the next chapter.

Although this method gives accurate solutions for the stress intensity factors for straight cracks, a more generalized method should be used to determine the complete stress and displacement distributions around any arbitrary branched crack. The generalized method that will be used to determine the stress and displacement fields as well as the stress intensity factors, for any arbitrary oriented crack, is the BIEM as will be seen in the next chapter.

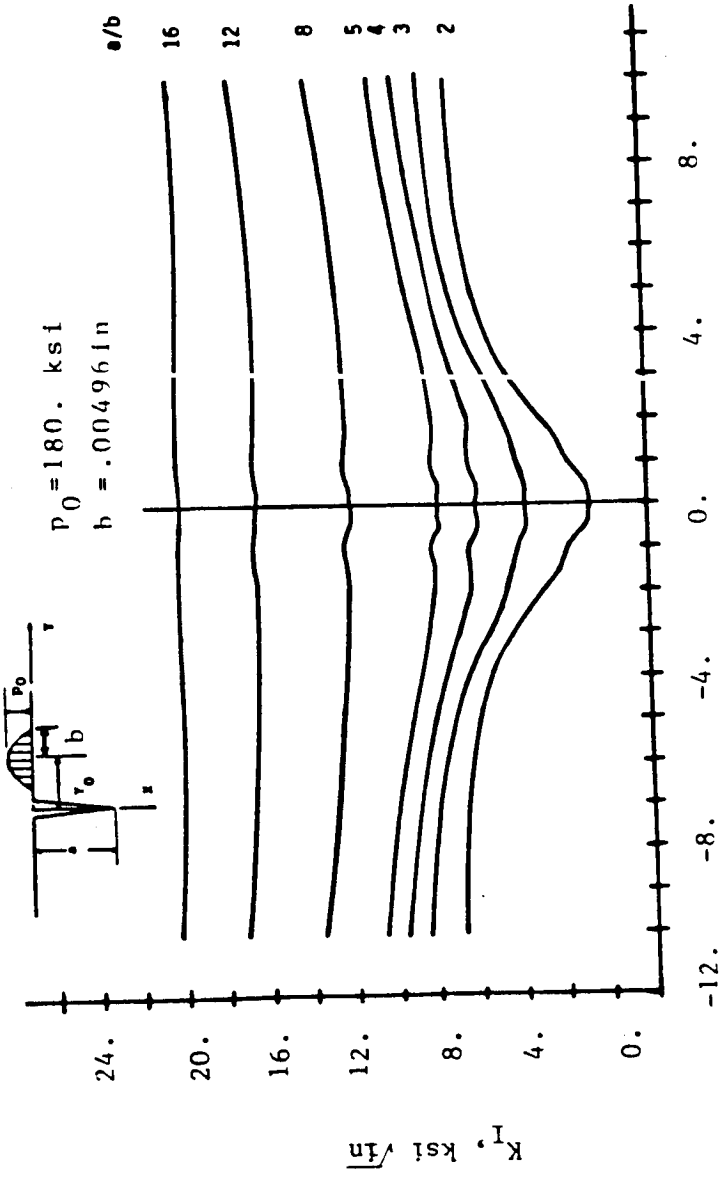

Fig. 4.16 Variation of K_I Stress Intensity Factor for Different Crack Lengths as a Function of Roller Position

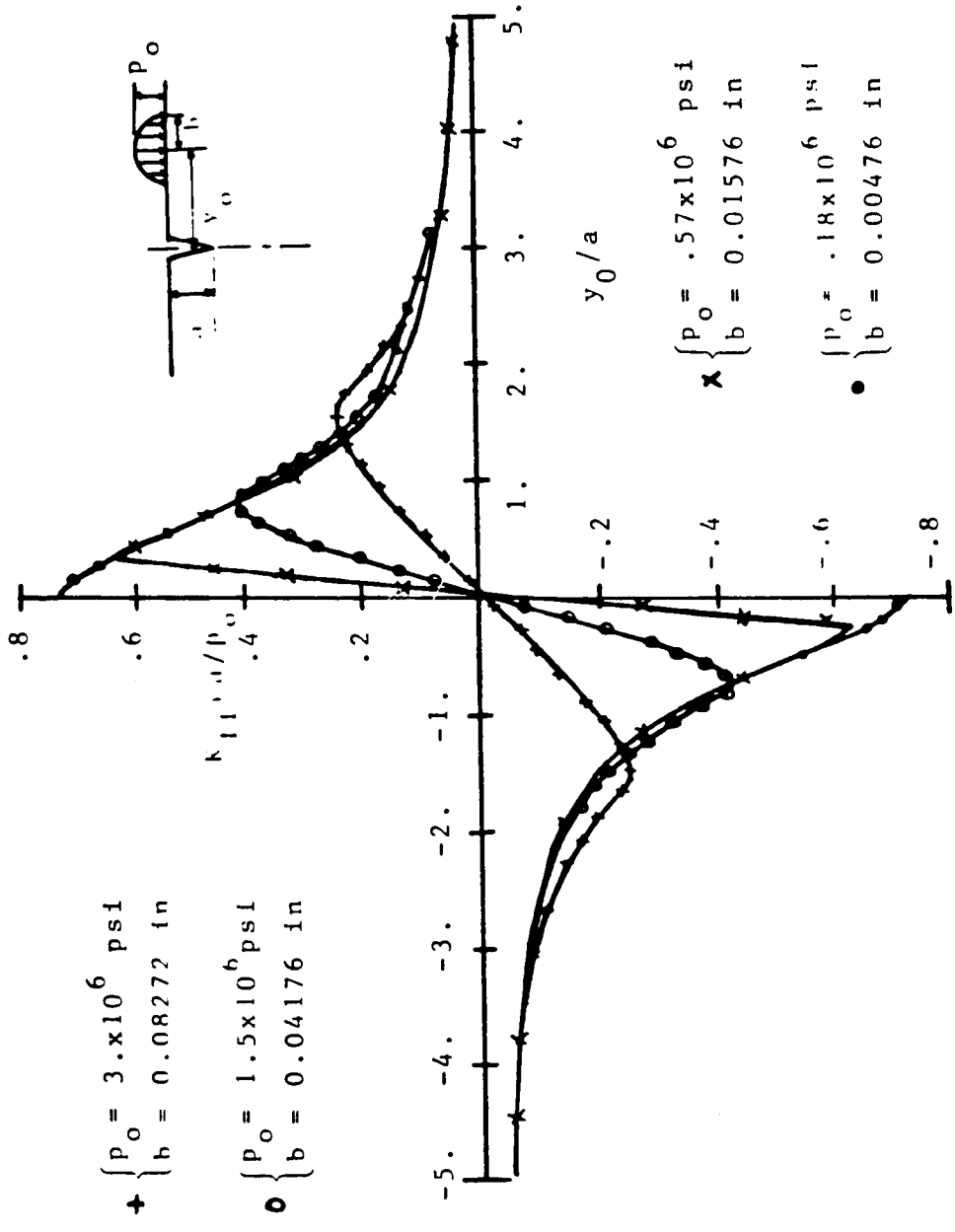

Fig. 4.17 Variation of the K_{II} Stress Intensity Factor for Different Values of the Hertzian Pressure as a Function of Roller Position

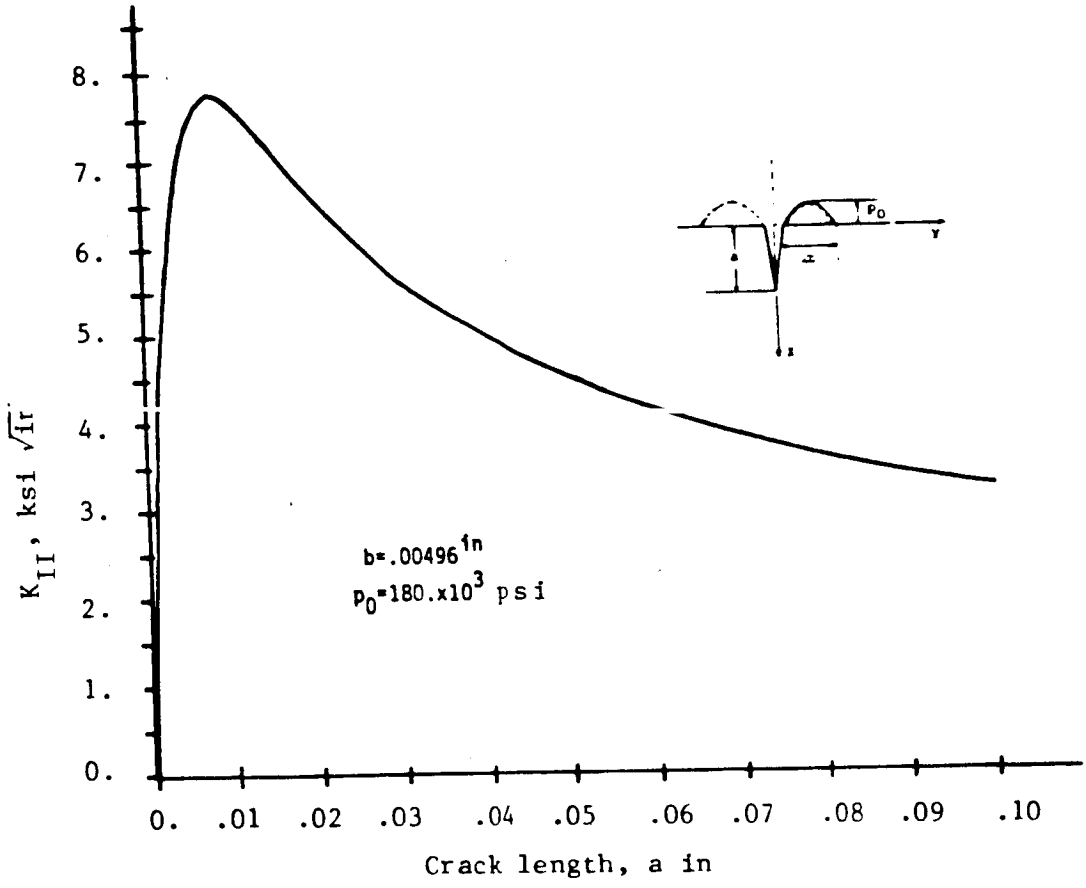

Fig. 4.18 Maximum K_{II} Stress Intensity Factor as a Function of Crack Length

CHAPTER FIVE

MIXED-MODE FAILURE ANALYSIS OF THE INNER RACEWAY OF HIGH SPEED BEARINGS

Chapter One described the different failures observed in the inner raceway of bearings, and especially the new catastrophic failure recently detected in test rigs for high speed aircraft engine bearings. This chapter utilizes the mixed-mode failure criteria of chapter Two to analyze the causes that lead to the brittle failure of high speed bearings, using the boundary integral method described in chapter Three and the major loading conditions summarized in chapter Four. The interaction of the Hertzian stresses and the tangential stresses due to the rotational speed and press fit, in the presence of a surface defect are first described in terms of the stress intensity factors, K_I and K_{II}. Then, the crack propagation direction is determined using the different crack growth criteria described in section 2.4. Finally, the time to failure is estimated using fatigue failure data of M50 bearing steel.

5.1 Stress Intensity Factors

The stress intensity factors are determined for a typical roller bearing used as a support for the main shaft of aircraft

Table 5.1 Typical Roller Bearings for Turbine Engine Main Shaft.

-Roller Diameter		0.5 in.
-Roller Length		0.57322 in.
-No. of Rollers		28
-Shaft	Inner Radius	2.0 in.
	Outer Radius	2.30233 in.
-Inner Raceway	Inner Radius	2.300 in.
	Outer Radius	2.600 in.
-Outer Raceway	Inner Radius	3.1 in.
	Outer Radius	3.35 in.
-Shaft Speed		25,500 RPM
-Load on most heavily loaded roller		500 lbs., 1,000 lbs., 1,500 lbs., 2,000 lbs.
-Interference fit of inner raceway onto the shaft at 0 RPM		0.00233 in.

engines. The dimensions of the bearing and the shaft are shown in Table 5.1. A two dimensional analysis is performed assuming a plane strain condition, representing the mid-section of the inner raceway. This approximation is assumed sufficiently good to identify some mechanisms that lead to the catastrophic failure of the inner raceway. The inner raceway was modelled as a plate with width equal to the inner raceway thickness and length twice the width, corresponding to the distance between two rollers. The curvature of the raceway was ignored since the ratio of the raceway thickness to the outer radius of the inner raceway is small.

The tangential stresses applied at the edge of the plate are calculated from the solution of a rotating disk at 25,500 RPM superimposed onto the tangential stresses of the press fit at the same rotational speed. The calculated tangential stress at the middle of the inner raceway was 42,300PSI. The variation of the tangential stress along the radius was approximated by a linear curve, decreasing to about 7% of the mid value.

A reaction pressure load was applied at the bottom of the plate to simulate the contact stresses transfered from the inner raceway to the shaft. The corresponding load of this pressure will be equated to the applied Hertzian load. Different Hertzian loading condition are assumed giving rise to different maximum pressures p_o and contact lengths b.

Table 5.2 summarizes the four Hertzian loading conditions

Table 5.2 The Geometry of the Hertzian Pressure distribution for different loads.

P lbs.	b in.	P_0 ksi.
500	0.00392	142.
1,000	0.00554	200.
1,500	0.00679	245.
2,000	0.00780	283.

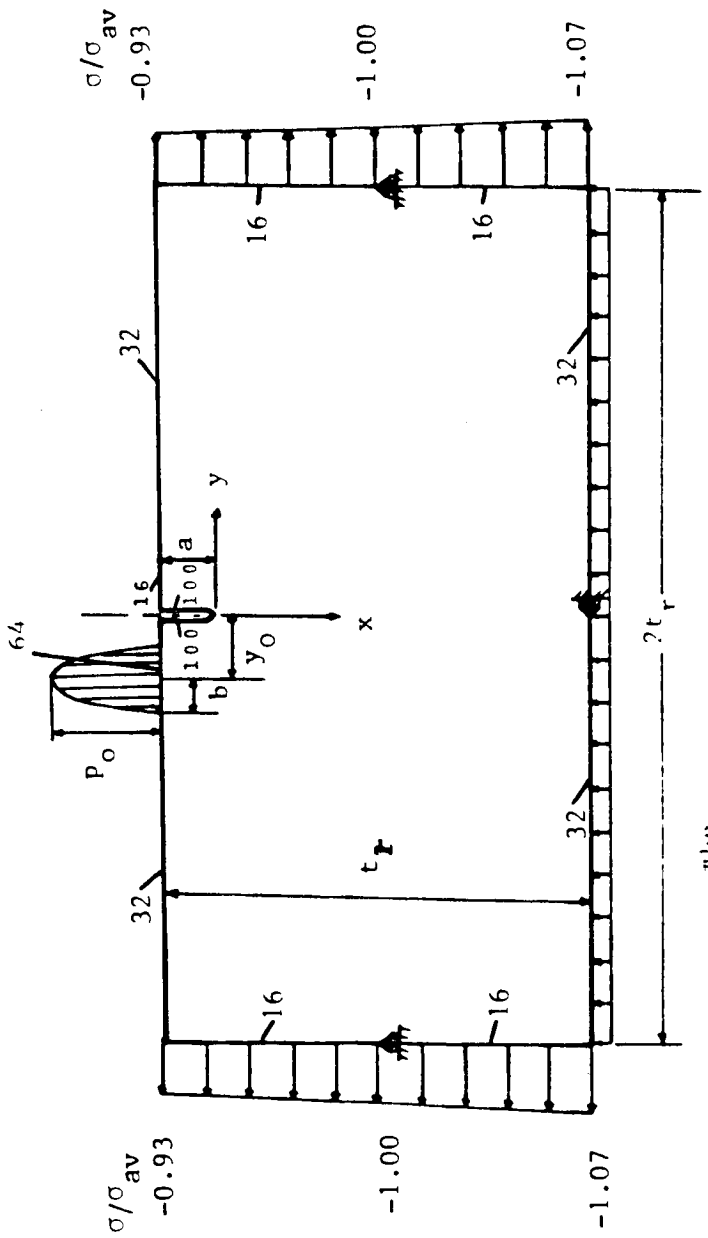

Fig. 5.1 Geometric Model and Applied Load of the Inner Raceway

used in the analysis. Fig. 5.1 shows the geometric modelling of the inner raceway and the number of nodes used in each subdivision for BIEM analysis.

The stress intensity factors are determined using the extrapolation method described in section 3.5. The shear stresses σ_{xy} and the normal stresses σ_y are multiplied by the square root of the distance to the crack tip and plotted versus that distance. Their intercepts with the axis at r equals zero, are proportional to the stress intensity factors K_{II} and K_I respectively. The stresses used in the extrapolation method were taken between 0.2a and 0.5a ahead of the crack tip.

To simulate the passage of each roller, the Hertzian loading is moved incrementally along the top face of the plate. The dynamic effect was ignored assuming steady state solution.

A typical variation of the mode I stress intensity factor with roller position and crack depth is shown in Fig. 5.2, for a Hertzian load equals 1,500 lbs. As seen from the figure, the compressive stresses of the Hertzian loading cause the decrease of the constant value of the mode I stress intensity factor due to the tangential stresses of the rotational speed and the press fit. For very small cracks, K_I is constant and then decreases rapidly as the roller approaches the crack and increases rapidly again after the roller moved away from the crack. The negative K_I values observed indicates crack closure. For large cracks the rapid decrease in K_I diminishes and practically disappears since

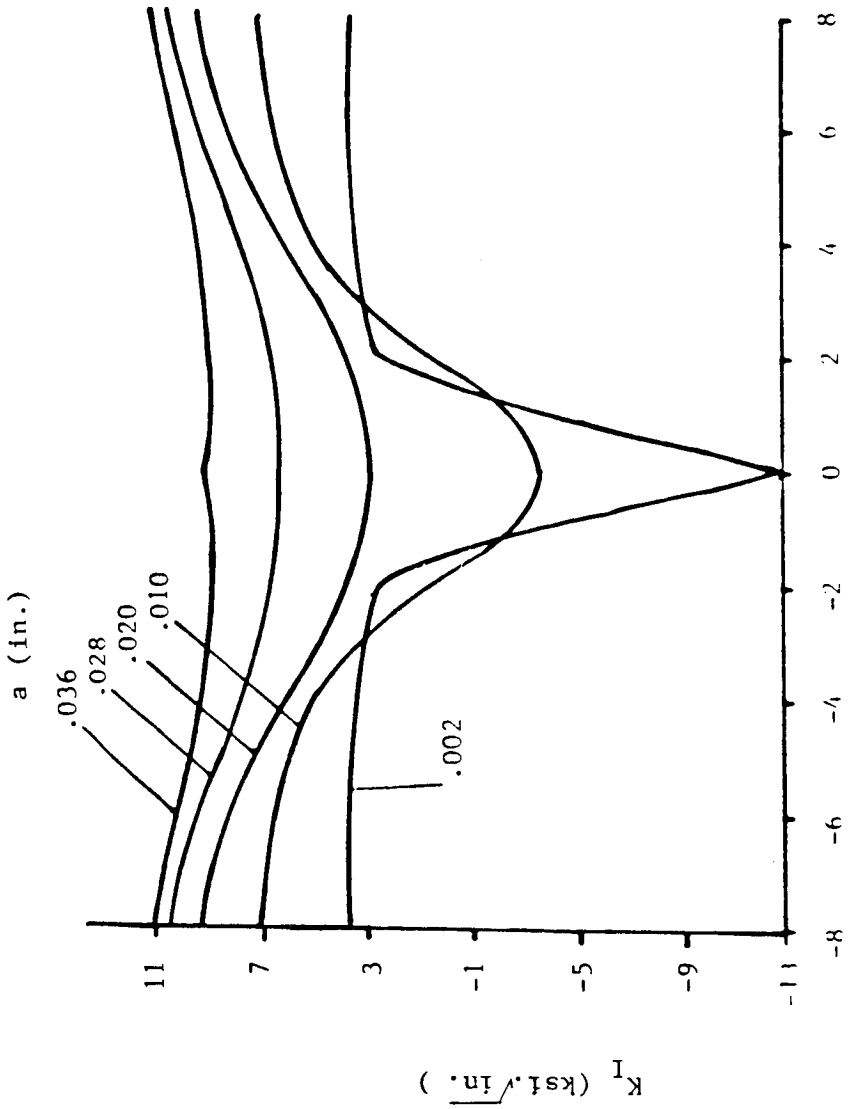

Fig. 5.2 Variation of K_I Stress Intensity Factor with Roller Position as a Function of Crack Length, a.

the crack tip at these lengths has passed outside the highly compressive Hertzian stress field.

These variations in K_I can result in crack growth for small cracks. However, there is another stress intensity factor namely the shear mode or mode II, which may play a more important role in crack propagation. The variation of the mode II stress intensity factor is shown in Fig. 5.3 for the same Hertzian loading condition as above. The value of K_{II} starts at zero when the roller is far from the crack tip. As the roller approaches the crack, K_{II} starts to decrease until it reaches a minimum, as the Hertzian pressure distribution reaches the crack, then increases rapidly back to zero. When the roller starts to move to the other side of the crack it changes sign and starts to increase to the maximum value and then decreases back to zero. For small cracks the change in K_{II} is very abrupt, but for deeper cracks, the change in K_{II} is more gradual. The change in K_{II} persists at greater depths than K_I.

The variations of the stress intensity factors with roller position for different Hertzian loading are shown in Fig. 5.4 and 5.5 for K_I and K_{II}, respectively, for a crack length equals 0.008in. As seen in the plots, the greater the Hertzian load the greater the change in the stress intensity factors.

Fig. 5.6 represents the maximum absolute value of K_{II} for different applied Hertzian loads. The values of K_{II} increase until reaching a maximum at depths which correspond to the

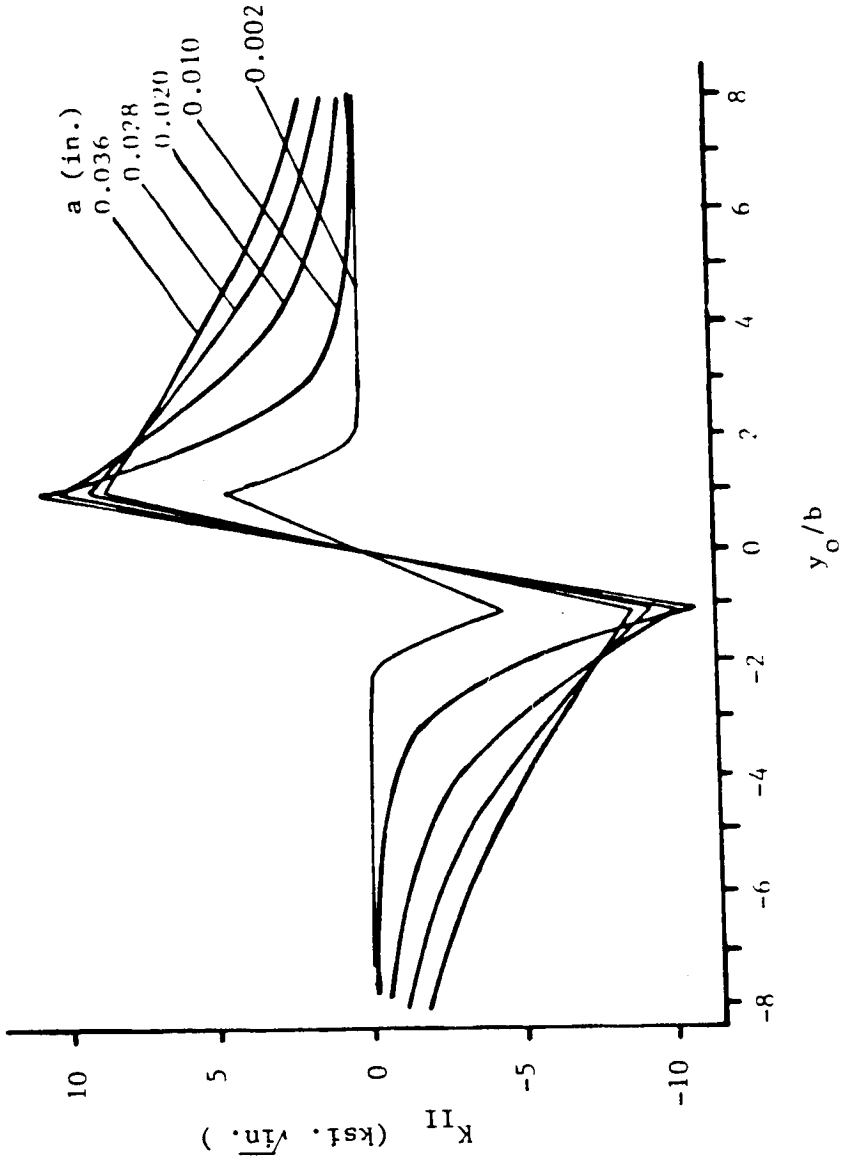

Fig. 5.3 Variation of K_{II} Stress Intensity Factor with Roller Position as a Function of Crack Length, a.

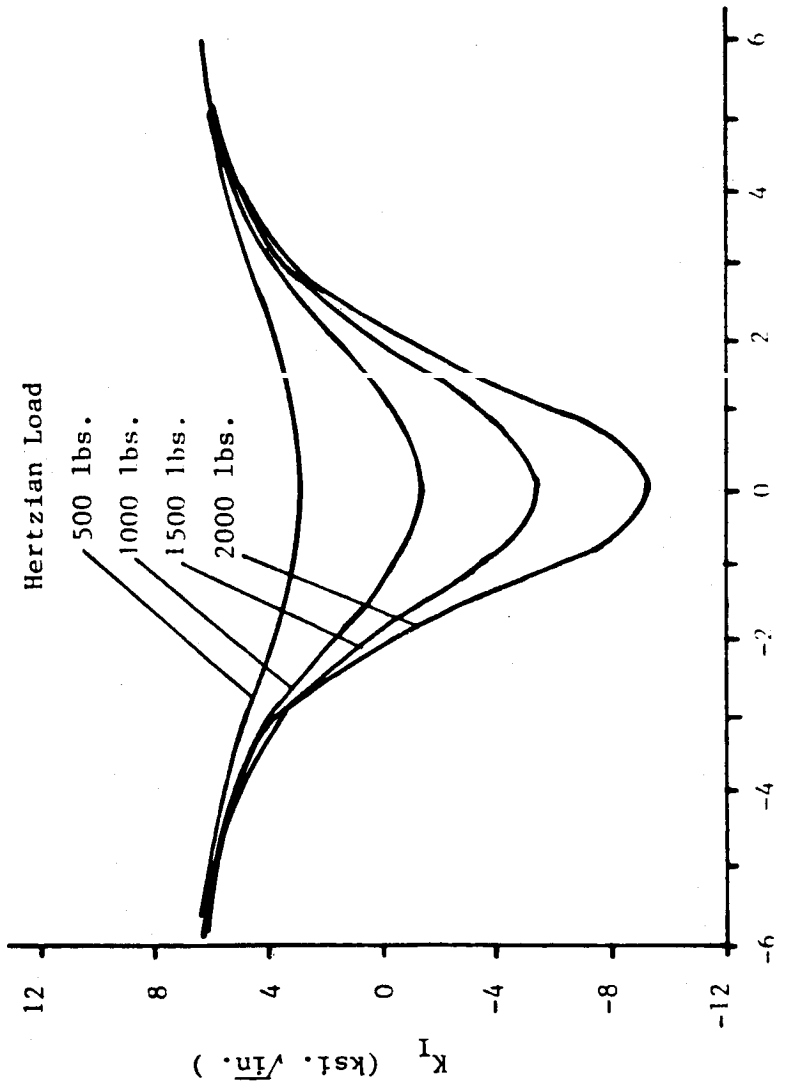

Fig. 5.4 Variation of K_I Stress Intensity Factor with Roller Position as a Function of the Hertzian loads, (a=0.008in.)

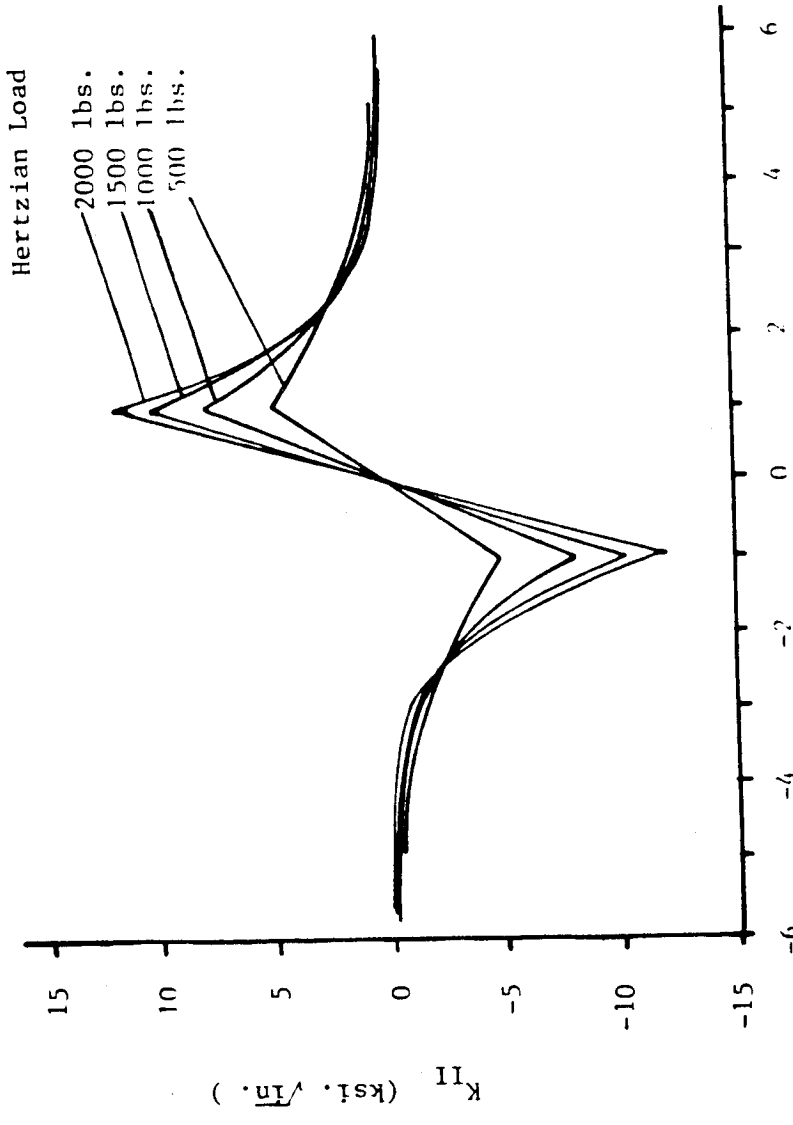

Fig. 5.5 Variation of K_{II} Stress Intensity Factor with Roller Position as a Function of the Hertzian Loads, (a=.008in)

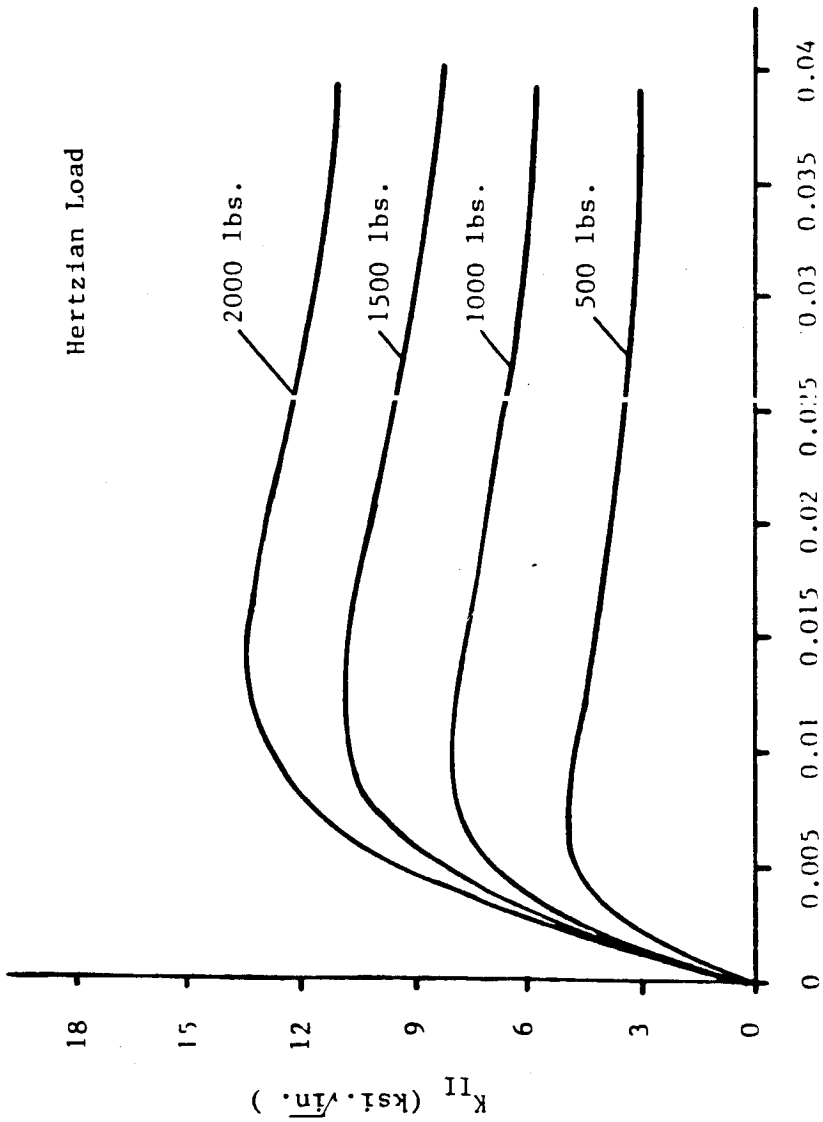

Fig. 5.6 Maximum Absolute Value of K_{II} Stress Intensity Factor for Different Hertzian Loads as a Function of Crack Length

maximum shear stress and then decrease slowly. This is due to the fact that although the shear stress decreases as we move down from the surface causing K_{II} to decrease, the increase in crack length causes K_{II} to increase.

When friction is added the stress intensity factors are modified as shown by the stress distributions given in section 4.4. The variation of the stress intensity factors K_I and K_{II} for different friction factors, f, (f = 0.0, 0.05, 0.1, 0.2, 0.3), are plotted in Fig. 5.7 and 5.8, for a crack length equals 0.002in. As the roller approaches the crack the friction forces act in a direction to close the crack, causing K_I to decrease even more, but as soon as the roller passes the crack, the friction forces act now to open the crack, causing an increase in K_I. As the roller moves further out, the effect of friction disappears. As for mode II, as shown in Fig. 5.8, K_{II} increases in absolute value as the roller approaches the crack, and then decreases as the roller moves to the other side of the crack since at that point the shear stresses are positive while the friction forces are still causing a negative shear.

Note that the stress intensity factors for the crack length considered are below the critical value, K_{Ic}, and when K_I is maximum K_{II} is zero and when K_{II} is maximum, K_I is almost minimum. This lower than critical stress intensity factor and phase shift causes a complex fatigue mixed-mode loading condition that can only be analysed using the crack propagation criteria

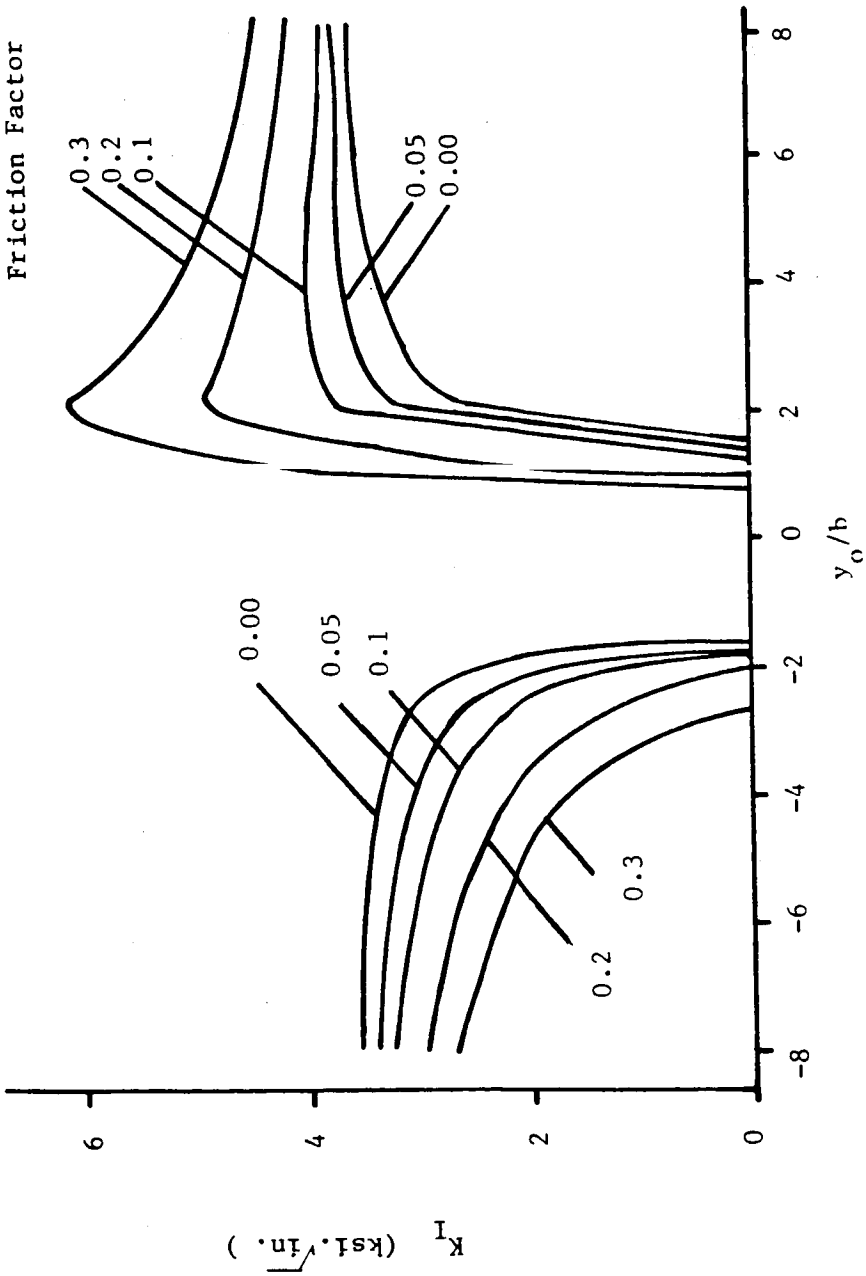

Fig. 5.7 Variation of K_I Stress Intensity Factor as a Function of Roller Position for Different Sliding Friction Factors, f, (a=0.002in.)

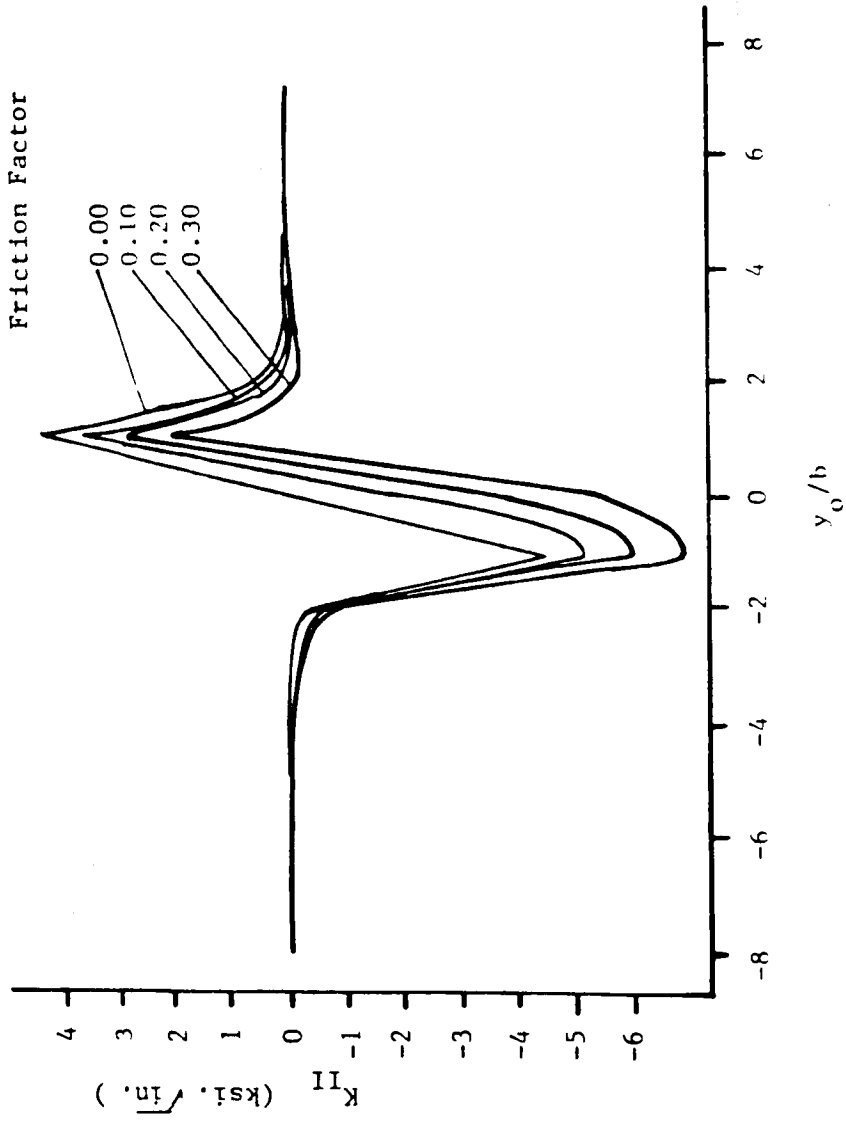

Fig. 5.8 Variation of K_{II} Stress Intensity Factor as a Function of Roller Position for Different Sliding Friction Factors, f, (a=0.002in.)

discussed in chapter Two.

5.2 Crack Propagation Directions

a) Static Crack Growth

To determine the crack propagation direction, an effective stress intensity factor should be considered to combine the mixed-mode loading effect observed with each passage of the roller. The criterion, that will be mainly emphasized, is the crack extension force criterion, also known as the "Energy Release Rate", as discussed in section 2.2. Therefore, the stress intensity factors for every roller position, will be used to determine the crack extension forces due to the tangential stresses, $G_{\theta\theta}$, and due to shear, $G_{r\theta}$, for every angle θ around the crack tip, using Eq. 2.10.

A typical variation of the maximum crack extension forces, $G_{\theta\theta}$ and $G_{r\theta}$, with roller position, are shown in Fig. 5.9 and Fig. 5.10, respectively, for a crack length equals 0.004in. The crack extension forces due to the tangential stresses have a constant value when the roller is far from the crack, (y_0/b is large). $G_{\theta\theta}$ starts to decrease with the approach of the highly compressive Hertzian stresses, then starts to increase to a new maximum due to the sharp increase in the mode II stress intensity factors present when the Hertzian pressure is at the edge of the

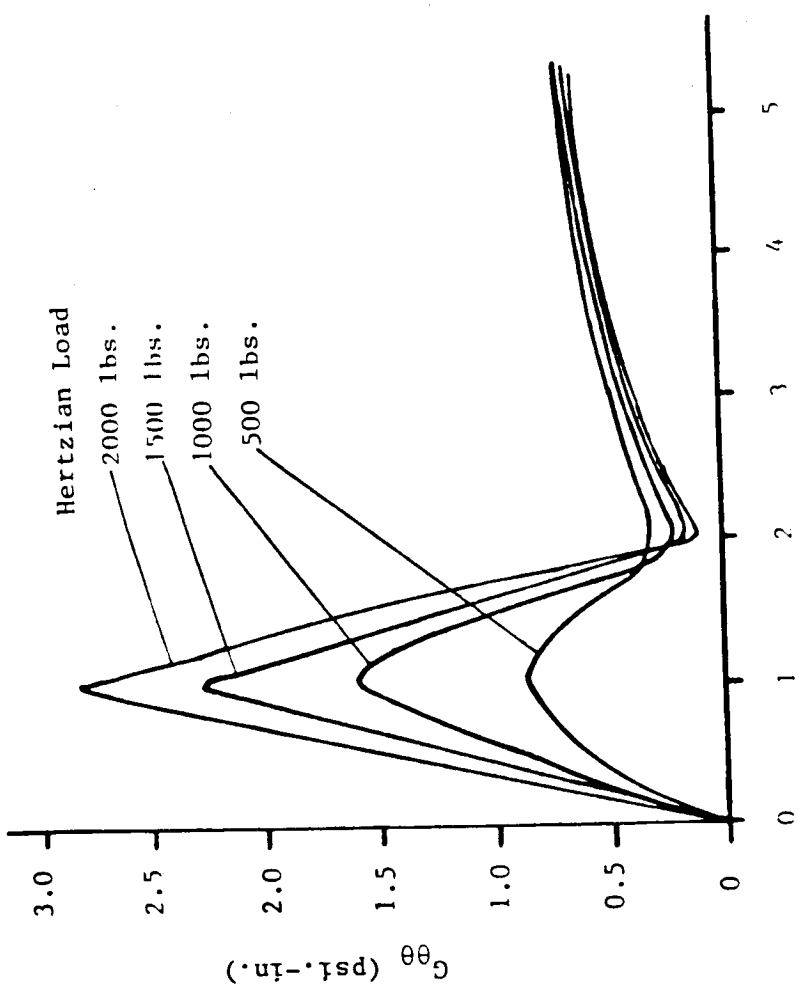

Fig. 5.9 Variation of the Maximum Tangential Crack Extension Forces as a function of Roller Position for Different Hertzian Loads (a=0.004in)

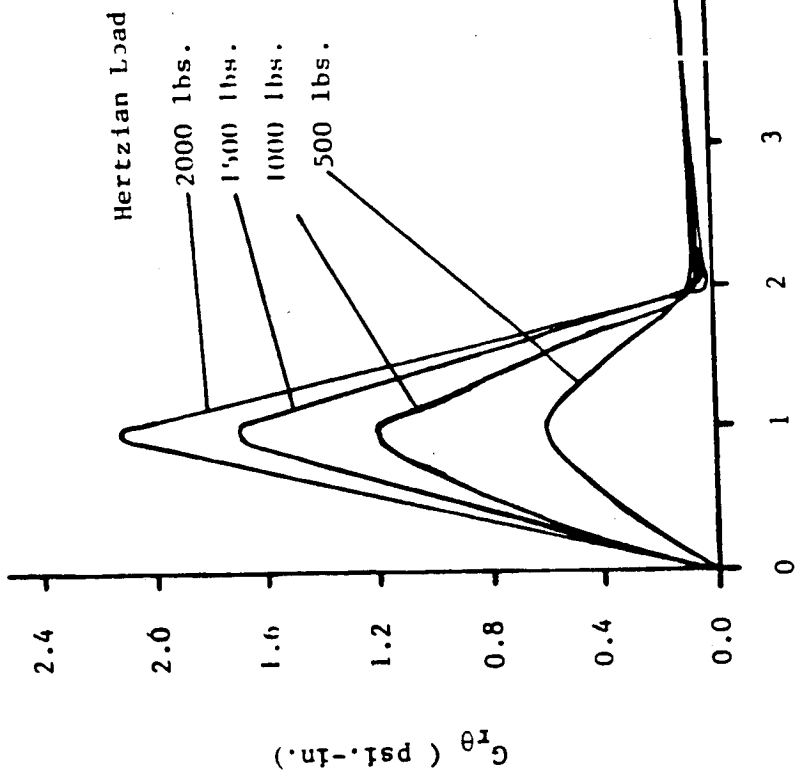

Fig. 5.10 Variation of the Maximum Shear Crack Extension Forces as a Function of Roller Position for Different Hertzian Loads, (a= 0.004 in.)

crack, ($y_0/b=1.0$). When the roller is positioned on top of the crack tip, ($y_0/b=0.0$), the shear effect goes to zero, and the crack is completely closed, causing the crack extension forces to be zero, assuming no lubricant had leacked in the crack. The same behavior is observed for the crack extension forces due to shear, as in Fig. 5.10.

With the presence of the Hertzian loading, two competing mechanism exist; 1) due to the compressive Hertzian stresses, the crack extension forces are decreased, and 2) due to the shear stresses, the crack extension forces are increased.

The angle along which the maximum tangential crack extension force acts, as a function of the roller position is shown in Fig. 5.11 and 5.12, for the maximum direction of $G_{\theta\theta}$ and $G_{r\theta}$, respectively. The angle starts at zero for the direction along which the maximum tangential crack extension forces acts, implying K_I is dominant, then starts to increase as the roller approaches, until reaching a maximum value of 70.53 degrees, indicating a pure shear mode, at $y_0/b=1.0$. The maximum shear crack extension force acts in the opposite direction; acts along 70 degrees for the pure mode I case, for large y_0/b, and at zero degrees for the pure mode II case, at $y_0/b=0.0$.

Fig. 5.13 shows a comparison of the values of the different mixed-mode crack propagation criteria; the maximum tangential stress, the minimum strain energy density factor, and the J integral approach as defined in section 2.4. The tangential

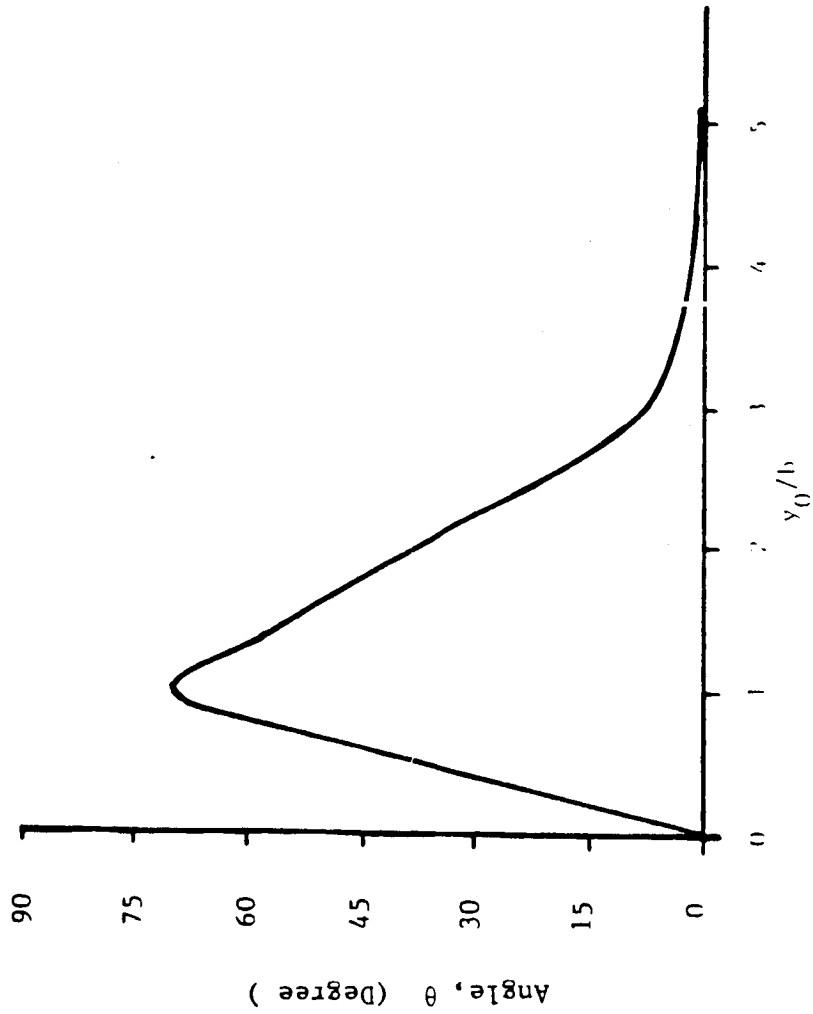

Fig. 5.11 Variation of Direction, θ, of the Maximum Tangential Crack Extension Forces as a Function of Roller Position, (a=0.004in., p=1500.1bs.)

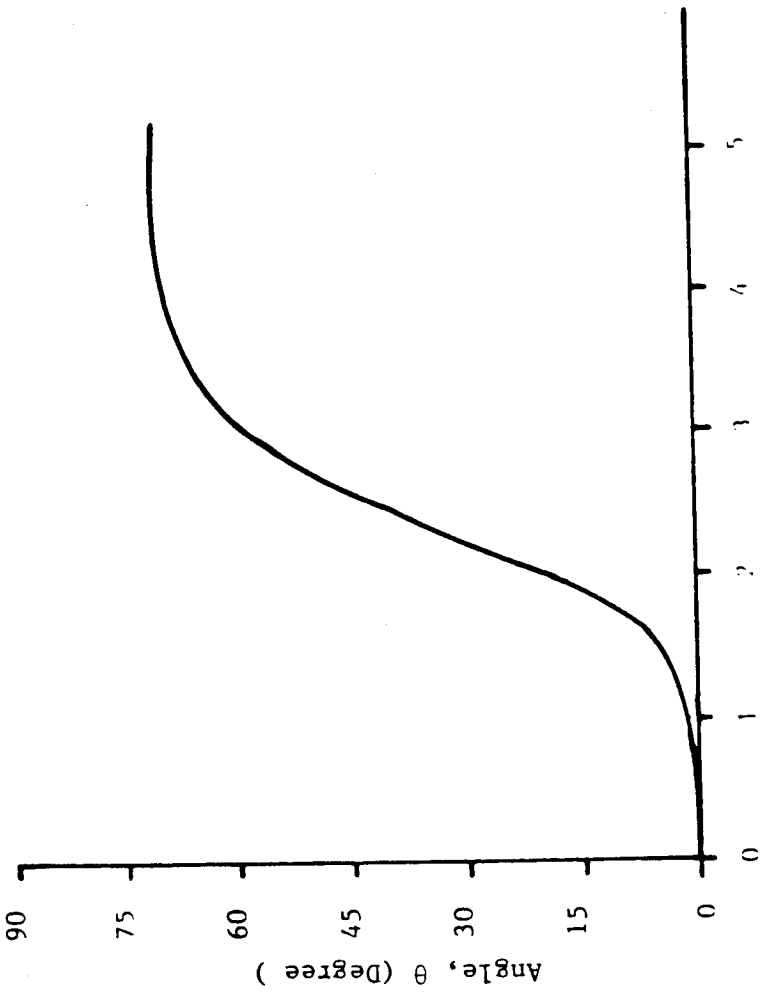

Fig. 5.12 Variation of the Direction, θ, of the Maximum Shear Crack Extension Forces as a Function of Roller Position, (a=0.004in., P=1500. lbs.)

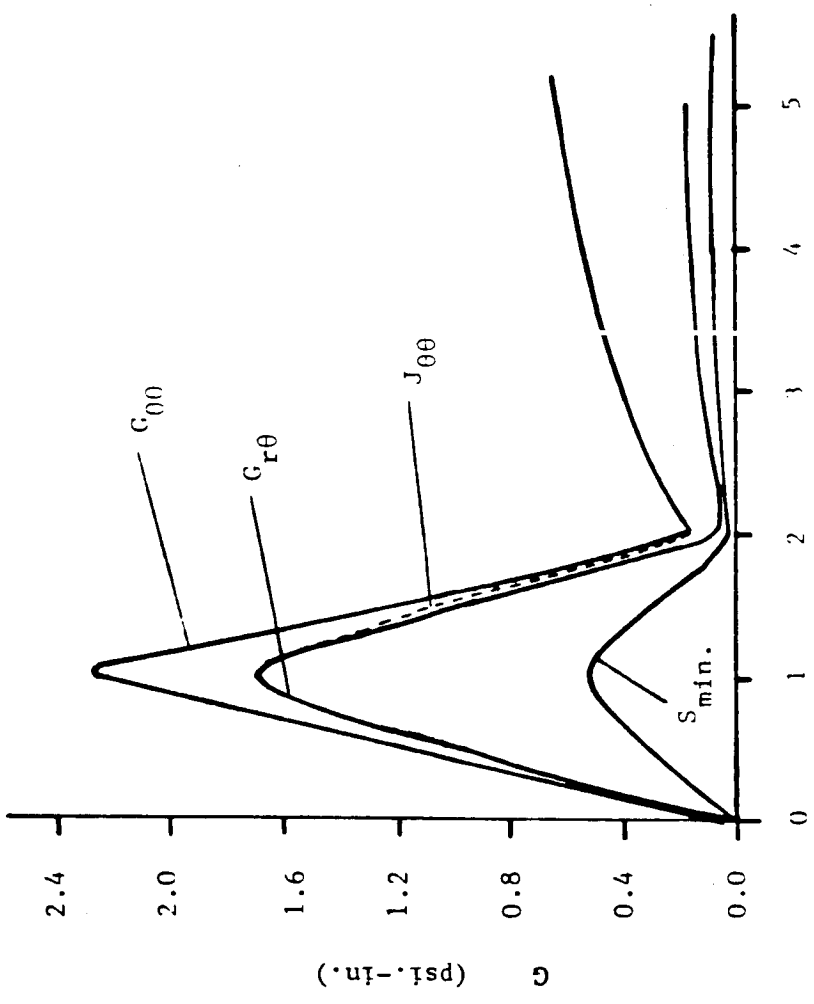

Fig. 5.13 Comparison between Crack Growth Criteria as a Function of Roller Position, (a=0.004in., P=1500. lbs.)

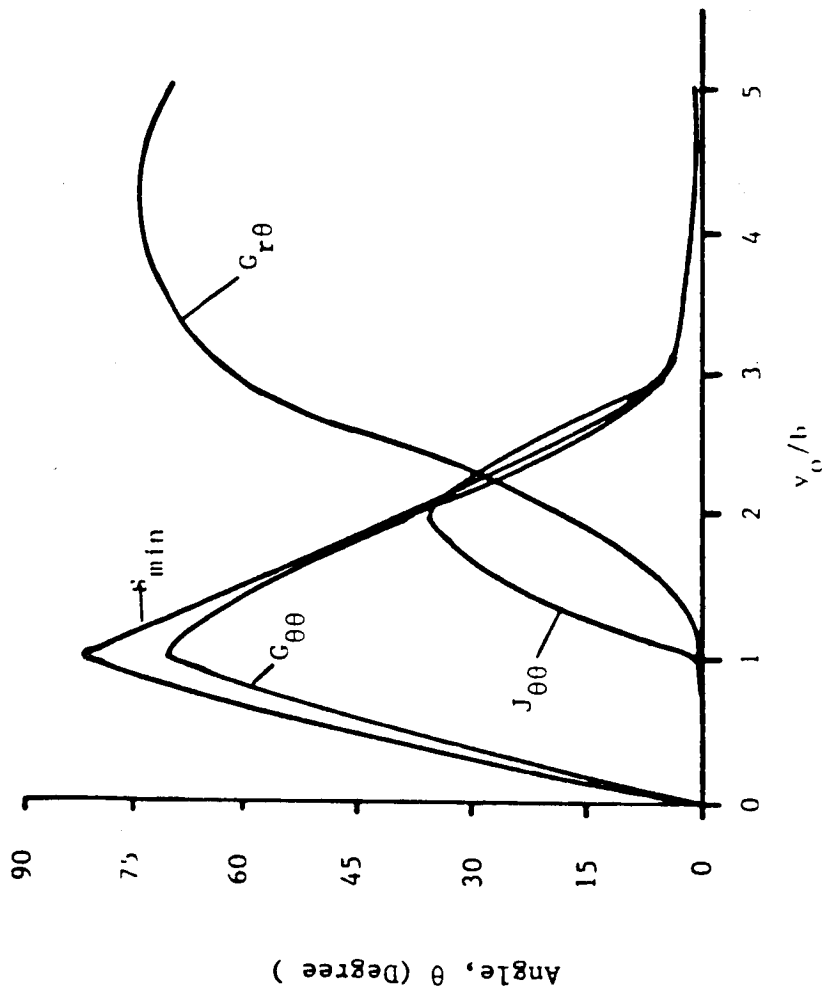

Fig. 5.14 Comparison between the Orientation of Crack Growth for Different Crack Extension Criteria, (a=0.004in., P=1500. lbs.)

stress criterion corresponds exactly to the tangential crack extension forces, $G_{\theta\theta}$. All the criteria show the same trend of decreasing in value as the Hertzian stress approaches and increase sharpely due to the shear effect. The main difference lies in the angle along which the maximum values act, as seen in Fig. 5.14. The minimum strain energy criterion shows a maximum at 83.61 degrees while the J integral at 0 degree, and the tangential stress at an angle of 70.53 degrees, at $y_0/b=1.0$.

Note that the maximum mode II stress intensity factor occurs with negative K_I values for small cracks, indicating crack closure. It had been observed that when mode II is associated with compressive normal stresses, friction occurs along the contact crack faces, thus reducing the effective mode II stress intensity factors, Ref. [47]. Swedlow, Ref. [48], proposed a simple coulomb friction along the contacting faces of the crack, acting in the opposite direction of the shear and proportional to the normal compressive stresses. Since the crack modelled in the BIEM mesh has a finite width, the compressive normal stresses on the crack faces are absent. As a result, the effective mode II stress intensity factor, K_{IIeff} was approximated by:

$$K_{IIeff} = K_{II} + f\ K_I \qquad \text{if } K_I < 0 \text{ and } K_{II} \neq 0$$

$$K_{IIeff} = K_{II} \qquad \text{if } k_I > 0 \qquad 5.1$$

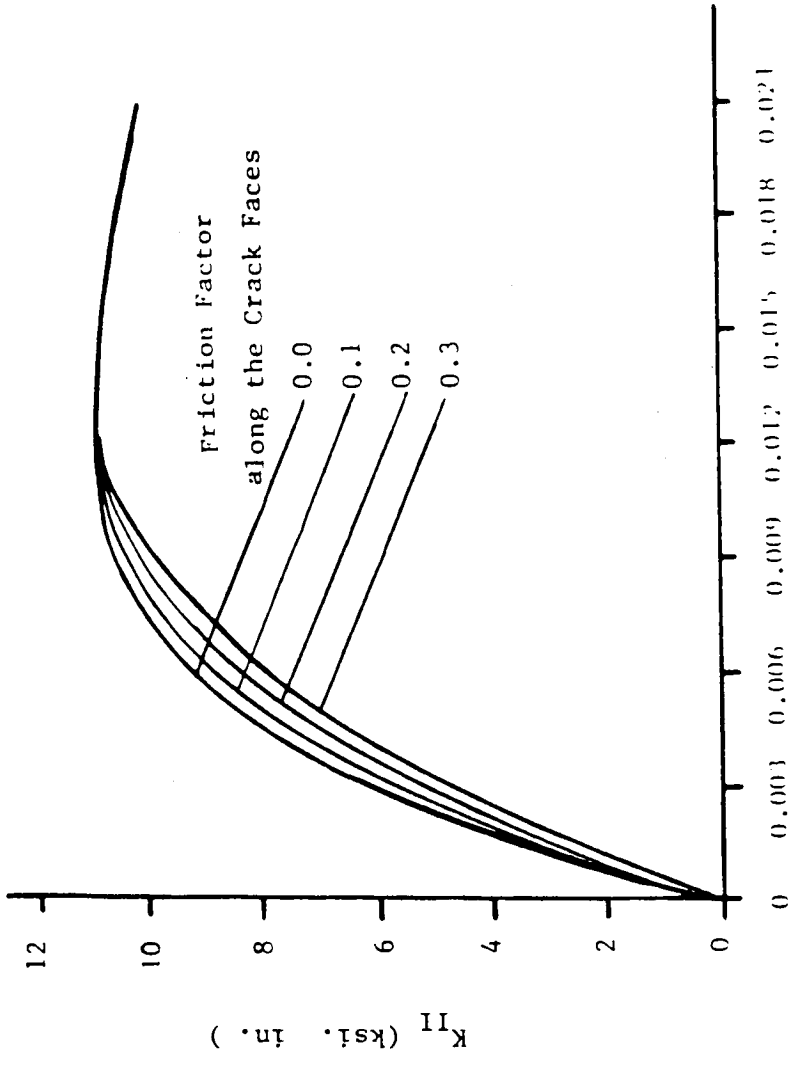

Fig. 5.15 Variation of the Maximum K_{II} for Different Friction values along the Crack Faces as a Function of Crack Length.

where f takes the opposite sign of K_{II}, since the friction acts to the decrease the shear. Although this model is crude, it is a good first approximation of the friction effect. The effect of the friction model used on the maximum mode II stress intensity factor is shown in Fig. 5.15 as a function of the crack length for different friction coefficients. K_{II} decreases with increasing friction factor until the crack length reaches 0.012in where K_I becomes positive, and no variation in K_{II} is observed.

The effect of the sliding friction, (friction between the roller and the inner raceway), on the crack extension forces is shown in Fig. 5.16 and 5.17. Fig. 5.16 represents the variation of the tangential crack extension forces as function of the roller position, for a crack length equals 0.01-in. For y_0/b less than zero the crack extension forces increase with increasing frictions, while decreasing with increasing friction for y_0/b greater than zero. This behavior is due to the friction forces which act to open the crack on one side of the crack and to close it when it is on the other side. The crack extension forces due to shear behave in almost the same manner, as seen in Fig. 5.18.

The third mechanism that also alter the variation of the crack extension forces, is the lubrication effect when the roller is on top of the crack, causing a normal stress distribution along the crack faces. This mechanism can modify the crack extension forces if the lubricant can penetrate into the crack

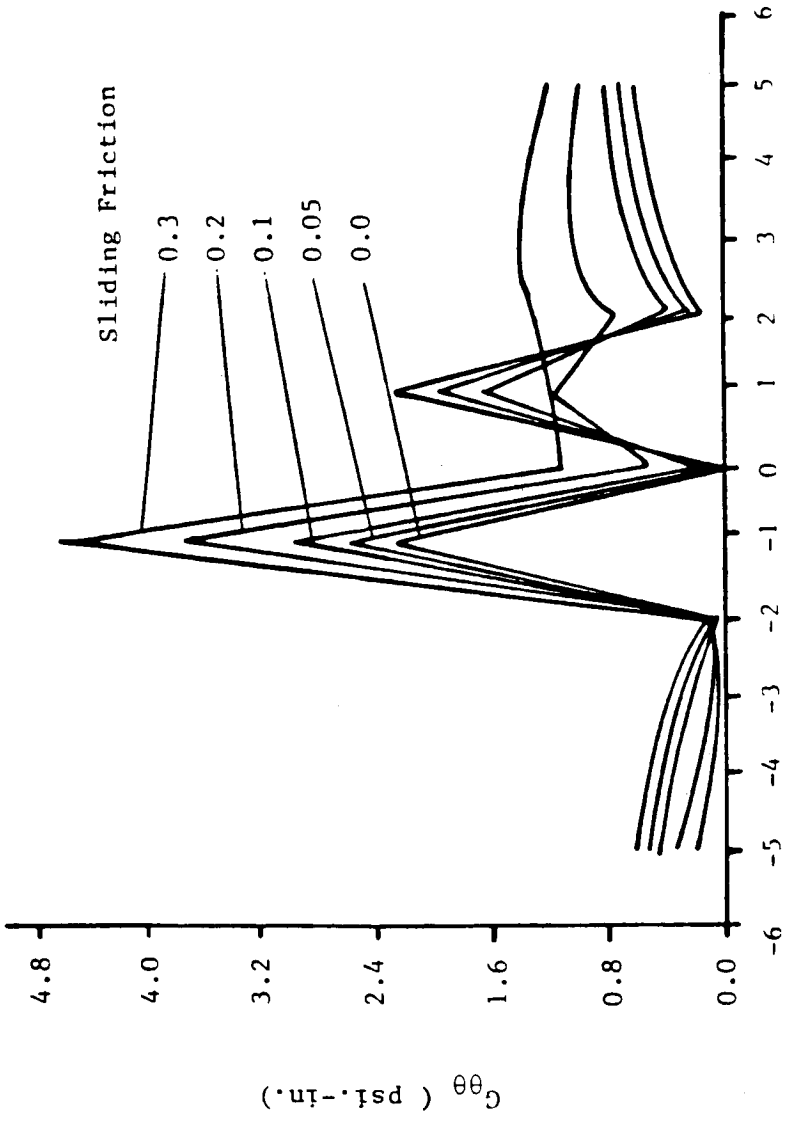

Fig. 5.16 Variation of the Maximum Tangential Crack Extension Forces for Different Sliding Friction Factors, as a Function of Roller Position, (a=0.004in., P=1500. lbs.)

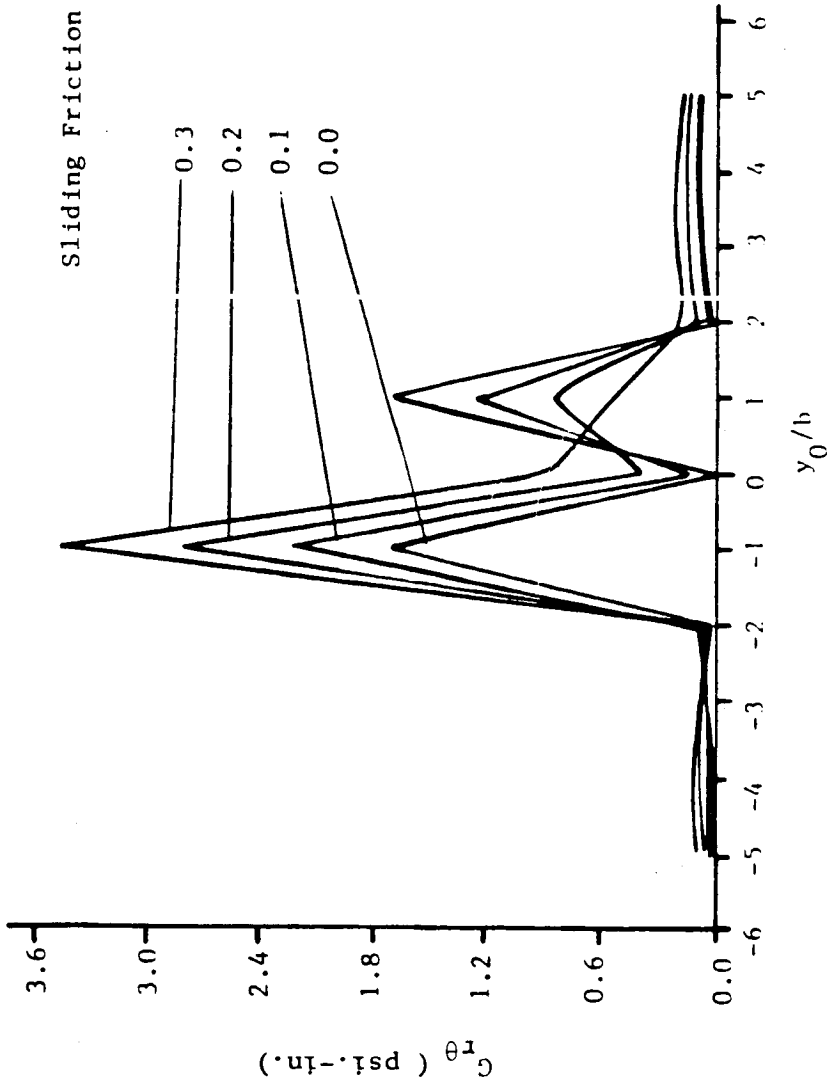

Fig. 5.17 Variation of the Maximum Shear Crack Extension Forces for Different Sliding Friction Factors, as a Function of Roller Position, (a=0.004in., P=1500. lbs.)

when the roller is on top of the crack tip. This mechanism involves a complex fluid-solid interaction problem, which has to include the viscous-drag and the surface tension forces to determine how far the lubricant can penetrate into the crack.

But as the roller approaches the crack, the normal compressive stresses, σ_y, try to close the crack and push the lubricant out, before the roller gets on top of the crack. For longer cracks, the commpressive stresses are limited to a small distance close to the surface, and at greater depths the stresses, σ_y, are in tension, due to the tensile stresses of the rotational speed. This effect causes the lubricant to be caught inside the crack and to pressurize it.

A uniform pressure was applied along the crack faces, when the roller is on top of the crack line, ($y_0/b=0.0$). The pressure assumed equals the maximum Hertzian pressure, p_0. The variation of the mode I stress intensity factor as function of crack depth is shown in Fig. 5.18, for $y_0/b=0.0$. The values of K_I are now positive, due to the high pressure applied along the crack faces, as compared to the negative values when no lubricant is assumed leaked inside the crack. The values of K_I increase rapidly with increasing crack length, and reache the critical stress intensity factor K_{Ic} at a crack depth equals 0.007in. This model is not realistic since the crack is closed as the roller approaches the crack line. If the crack is filled with lubricant, the high σy stresses will push the fluid outside. So assuming that there is

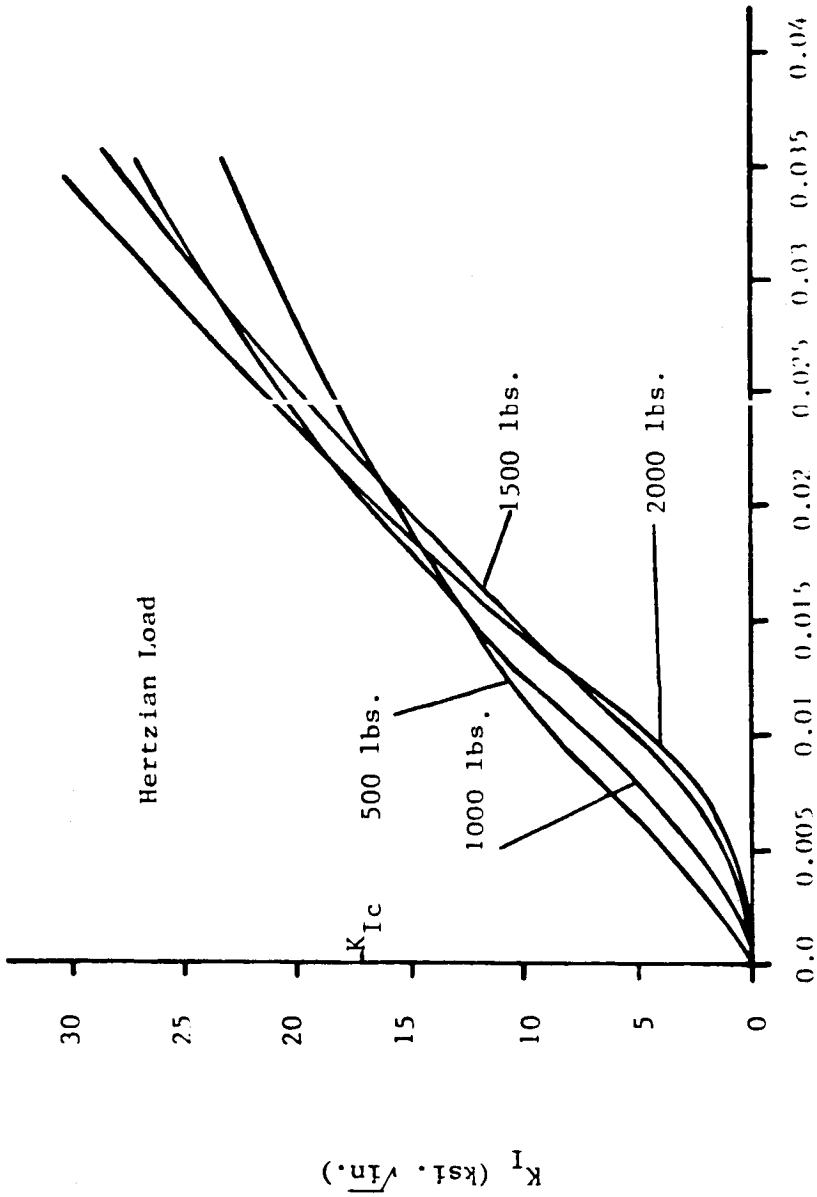

Fig. 5.18 Variation of K_I Stress Intensity Factor as a Function of Crack Length when Pressure is Applied Along the Crack Faces, (y_0/b=0.0)

no lubricant leakage, is a good approximation for very thin cracks.

Note that the results for the crack extension forces and the crack growth directions are for static loadings at one particular roller position. The crack extension forces given above are well below the critical value for unstable crack growth, for crack length below 0.05 in. assuming no-lubricant leakage. Thus, a fatigue process has to take place for a small crack to grow from the surface to the critical crack length.

b) Fatigue Crack Growth

The fatigue process is governed by the maximum changes in the crack extension forces, ΔG_{ij}, and the mean value $\bar{G}_{ij}$, as seen in section 2.5. For a given crack length, a, the maximum and minimum values of the crack extension forces are monitored for every angle θ, around the crack tip, as the roller approaches the crack and moves away from it. The direction, θ_{max}, which has the maximum change in the crack extension force, will be the direction of the crack growth. This model is based on the assumption that an element oriented in the direction of the maximum change in ΔG_{ij}, accumulates the largest amount of damage with each passage of the roller, making this element the first to open up and join the main crack.

Fig. 5.19 and 5.20 show the values of the maximum changes in

the crack extension forces, $\Delta G_{r\theta}$ and $\Delta G_{\theta\theta}$, as functions of crack depth. The maximum change in the tangential crack extension forces keeps on increasing with increasing crack length, Fig.5.19, while the change in the shear crack extension force increases sharply until reaching a maximum value then decreases, gradually, Fig. 5.20.

The actual directions of the crack growth could be plus or minus the presented values since we have complete reversal of the stress intensity factors when the roller cross from one side of the crack to the other. This symmetry will break down only when sliding friction is present.

The angle along which the maximum $\Delta G_{\theta\theta}$ acts, starts at a constant value of 70.53 degrees for very small cracks and high Hertzian loads, and then starts to decrease gradually with increasing crack length, Fig. 5.21. This constant value of the direction of the maximum $\Delta G_{\theta\theta}$ is due to the pure mode II stress intensity factor associated with negative K_I. For very small cracks and low Hertzian loadings, the change in K_{II} is negligible compared to the change in K_I, due to the high compressive Hertzian stresses and low shear stresses, causing the maximum change to occur along zero degrees (as seen in Fig. 5.21 with a Hertzian load of 500lb. and a crack length less than 0.004 in.).

The angle along which the maximum change in the shear crack extension forces acts, starts at zero and increases gradually with increasing crack lengths, Fig. 5.22. The crack length where

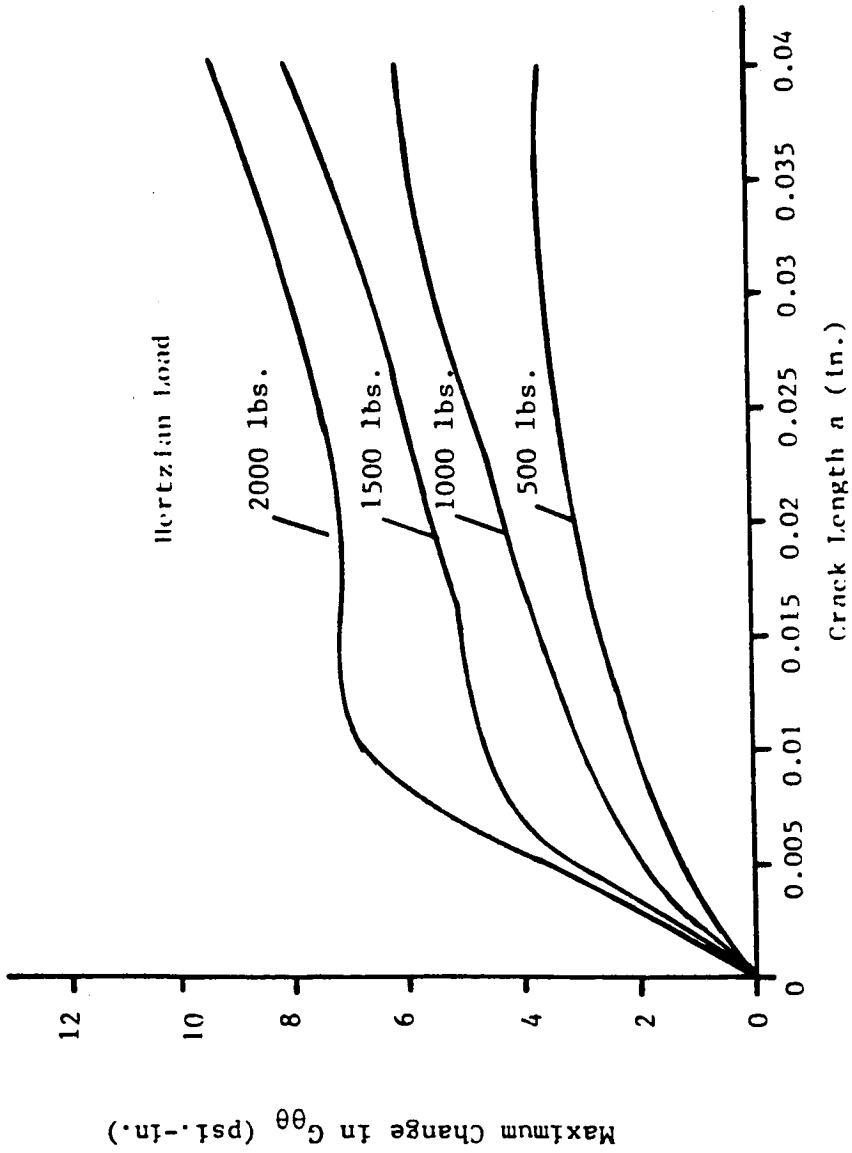

Fig. 5.19 Variation of the Maximum Change in the Tangential Crack Extension Forces as a Function of Crack Length, for Different Hertzian Loads.

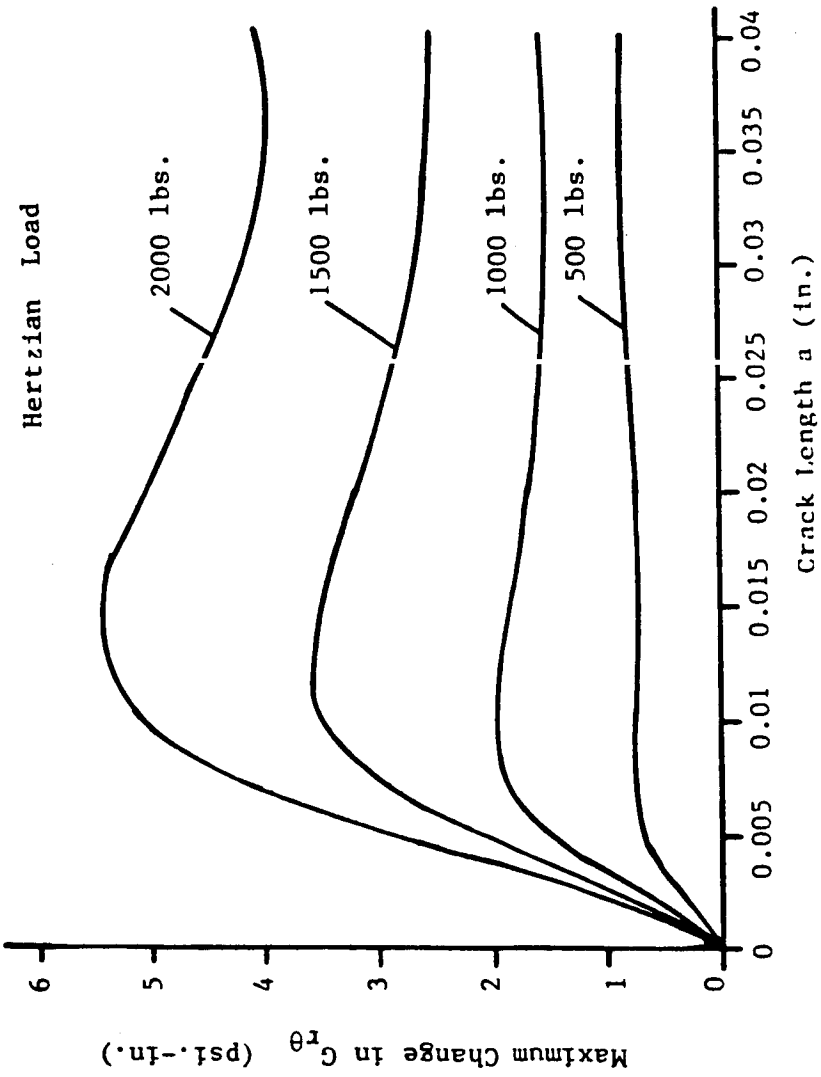

Fig. 5.20 Variation of the Maximum Change in the Shear Crack Extension Forces as a Function of Crack Length, for Different Hertzian Loads.

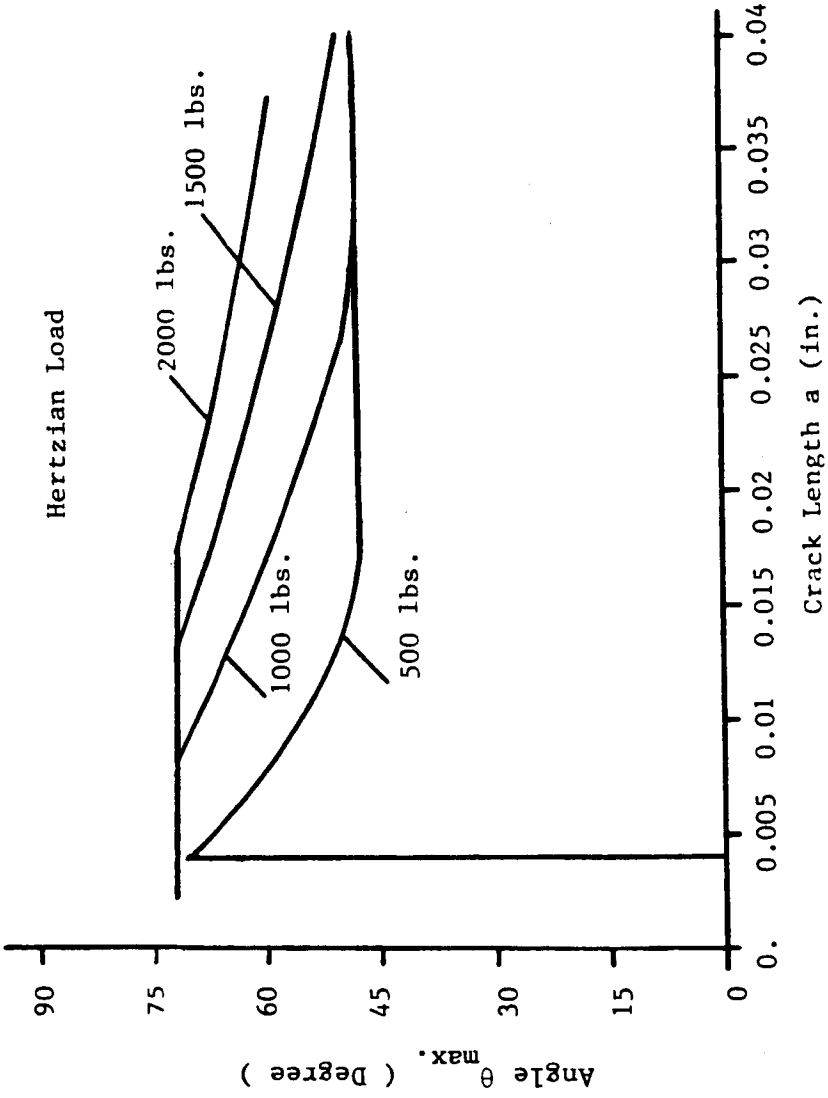

Fig. 5.21 Variation of the Direction along which the Maximum Change in $G_{\theta\theta}$ occurs, as a Function of Crack Length.

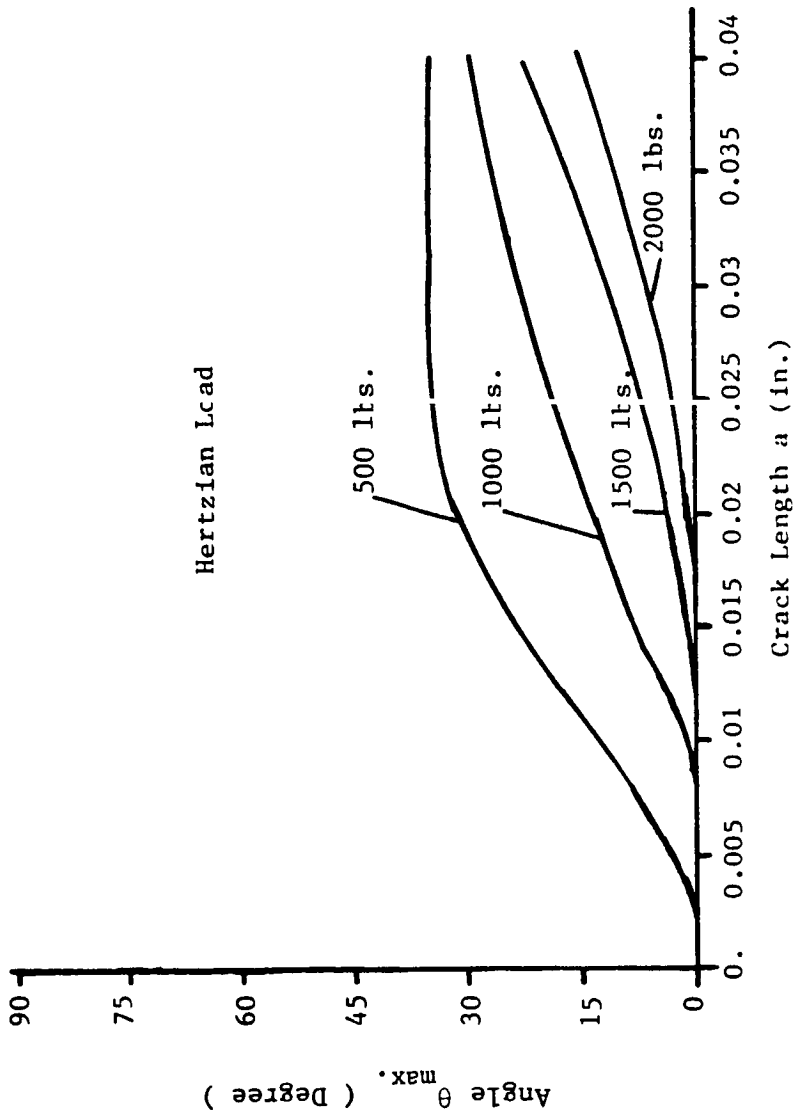

Fig. 5.22 Variation of the Direction along which the Maximum Change in $G_{r\theta}$ occurs, as a Function of Crack Length.

the angle starts to deviate from zero increase with the increase in the Hertzian load.

To determine which mode is the crack driving force, (shear growth or tensile growth), the values of $\Delta G_{\theta\theta}$ and $\Delta G_{r\theta}$ are compared with the threshold values for the material under consideration. Fig. 5.23 gives the regions for different crack growth modes. For values of $\Delta G_{\theta\theta}$ greater than 0.49 psi-in, Ref. [49], the tensile mode is dominant and will control the crack growth direction and rate. For value of $\Delta G_{\theta\theta}$ less than $\Delta G_{\theta\theta th}$, two regions are considered depending on the value of $\Delta G_{r\theta}$. For values of $\Delta G_{r\theta}$ less than $\Delta G_{r\theta th}$ there is no crack growth, while for values above $\Delta G_{r\theta th}$, the shear mode is the crack driving force.

Taking into consideration the above crack growth regimes, it is obvious that for crack depths less than 0.002in, the crack growth is governed by shear, while for a crack depth equal and above 0.002in the tensile crack growth is dominant.

When sliding friction is present, (friction between the roller and the inner raceway), the change in the crack extension forces increases with the increase of the friction factor. The main effect of friction is to make the crack extension forces non-symmetric, causing the crack to grow mainly in the direction opposite to the rolling direction, as observed experimentally, Ref. [50]. Table 5.3 presents the variation of the crack extension forces and the directions they act on and a Hertzian

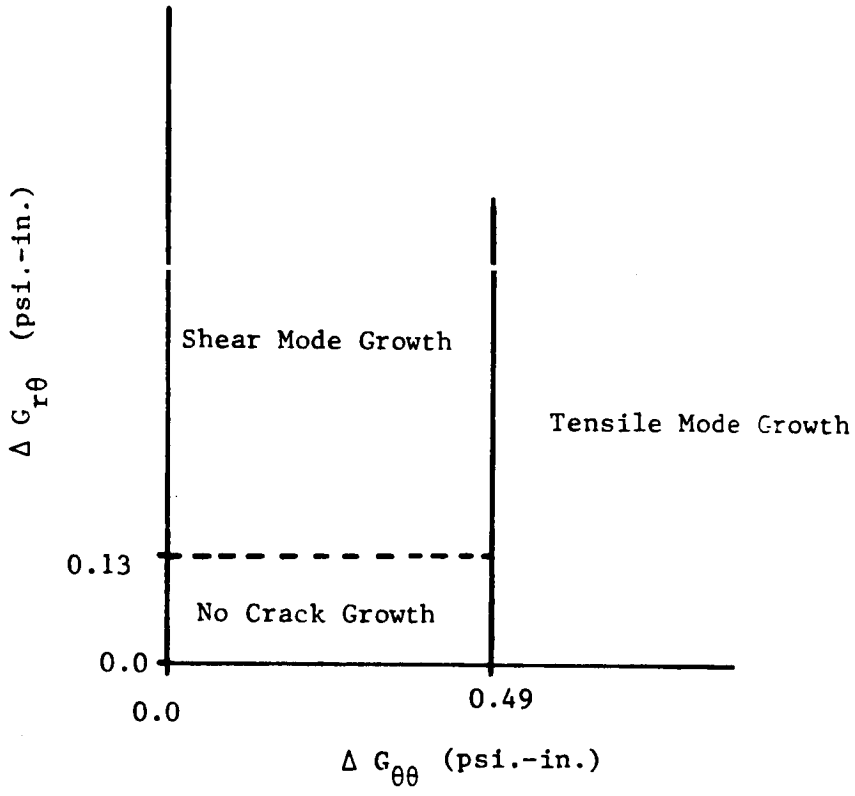

Fig. 5.23 Crack Growth Mode for M50 Steel.

Table 5.3 Variation of the Maximum Changes in $G_{\theta\theta}$, $G_{r\theta}$ and their corresponding angles, for Different Friction Coefficient for two crack Lengths, P = 1,500 lbs.

	a = 0.002 in.				a = 0.004 in.			
f	$\Delta G_{\theta\theta}$	θ	$\Delta G_{r\theta}$	θ	$\Delta G_{\theta\theta}$	θ	$\Delta G_{r\theta}$	θ
0.00	0.81528	71.	0.61152	0.	2.2626	71.	1.69716	0.
0.05	0.97454	71.	0.73098	0.	2.5972	71.	1.94813	0.
.1	1.1424	71.	0.85689	0.	2.9604	71.	2.22055	0.
.2	1.5231	71.	1.14247	0.	3.7565	71.	2.81766	0.
.3	1.9567	71.	1.46769	0.	4.6473	71.	3.48578	0.

Table 5.4 Variations of the Maximum Change in $G_{\theta\theta}$ and $G_{r\theta}$, Assuming a Coulomb Friction Along the Crack Faces, a = 0.004 in. and P = 1,500 lbs.

f	$\Delta G_{\theta\theta}$	θ	$\Delta G_{r\theta}$	θ
0.000	2.2626	71.	1.69716	0.
0.005	2.2484	71.	1.68649	0.
0.010	2.2342	71.	1.67585	0.
0.030	2.1780	71.	1.63365	0.
0.050	2.1224	71.	1.59198	0.
0.100	1.9867	71.	1.49016	0.
0.200	1.7286	71.	1.29661	0.
0.300	1.4885	71.	1.11652	0.
0.500	1.0622	71.	0.79672	0.
0.800	0.6758	0.	0.41796	0.

loading equal to 1,500 lbs., for different friction coefficients. The effect of friction is to increase the maximum change of the crack extension forces with the increase in the friction value. The direction, where the maximum changes in the crack extension forces occurs, does not change with friction.

Table 5.4 shows the variations of the maximum change, of the crack extension forces for a crack length of 0.004in. when friction along the crack faces are considered, as modelled in Eq. 5.1. The effect of friction is to reduce the mode II stress intensity factor when the crack is closed. The crack extension forces decrease with increasing friction, but the crack growth direction does not change, until large friction is assumed, causing the shear to stop. This vanishing effect of the shear mode is observed at a friction factor of 0.8 for a Hertzian load of 1,500lbs, and a crack length equal to 0.004in.

c) Crack Kinking

As seen from the above calculations, the crack tries to change the direction of growth. To simulate this effect, an original crack, a_1, of 0.004in., is extended in the direction of the maximum change of the crack extension forces for three different new crack ligament lengths, a_2, as seen in Fig. 5.24. The new stress intensity variations are determined along the new crack ligament, for different roller positions.

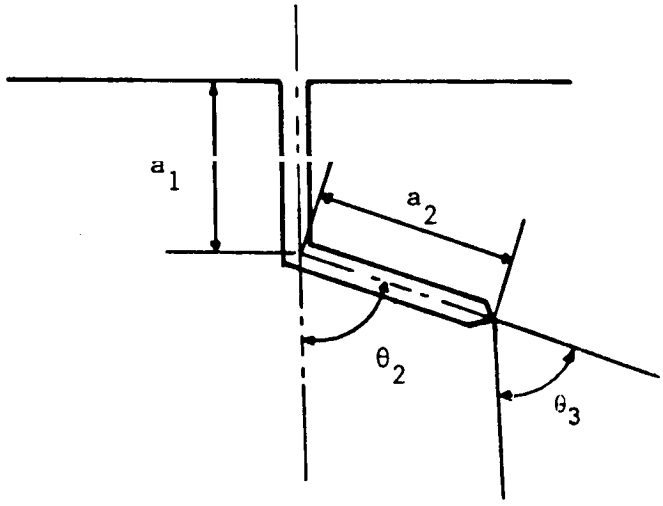

Fig. 5.24 Crack Kinking Geometry.

Table 5.5 Variation of the Maximum Crack Extension Forces for Different Hertzian Load and Kinked Ligament Length.

P lbs.	θ_2	a_1 in	a_2 in	$\Delta G_{\theta\theta}$	θ_3
500	69	0.004	0.001	0.61261	20.
			0.002	0.65259	18.
			0.003	0.94323	-3.
1500	71	0.004	0.001	0.57596	21.
			0.002	0.62055	19.
			0.003	1.20560	0.

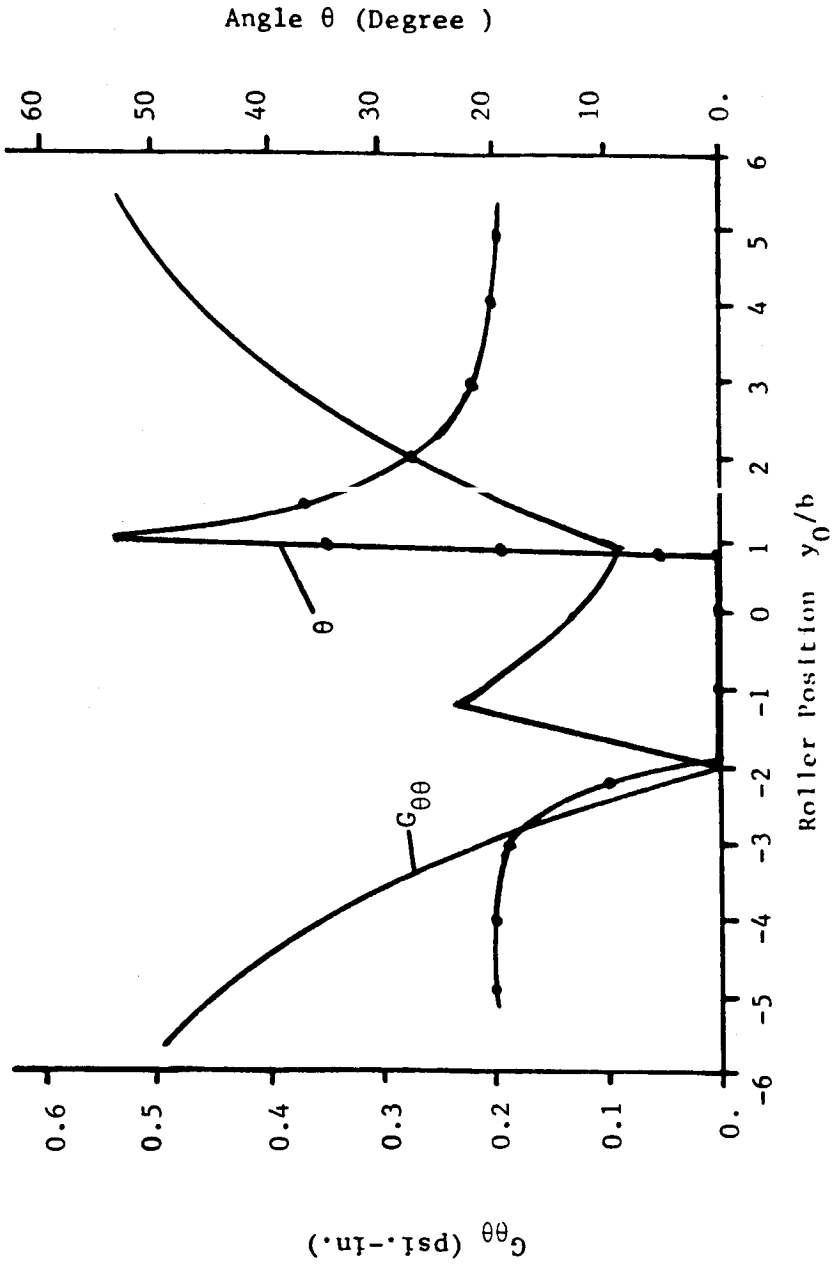

Fig. 5.25 Variation of the Maximum Tangential Crack Extension Forces and the Angle they act on as a Function of Roller Position, (a_1 = 0.004in., a_2 = 0.002in., $\theta_2 = 71^0$, P=1500 lbs.)

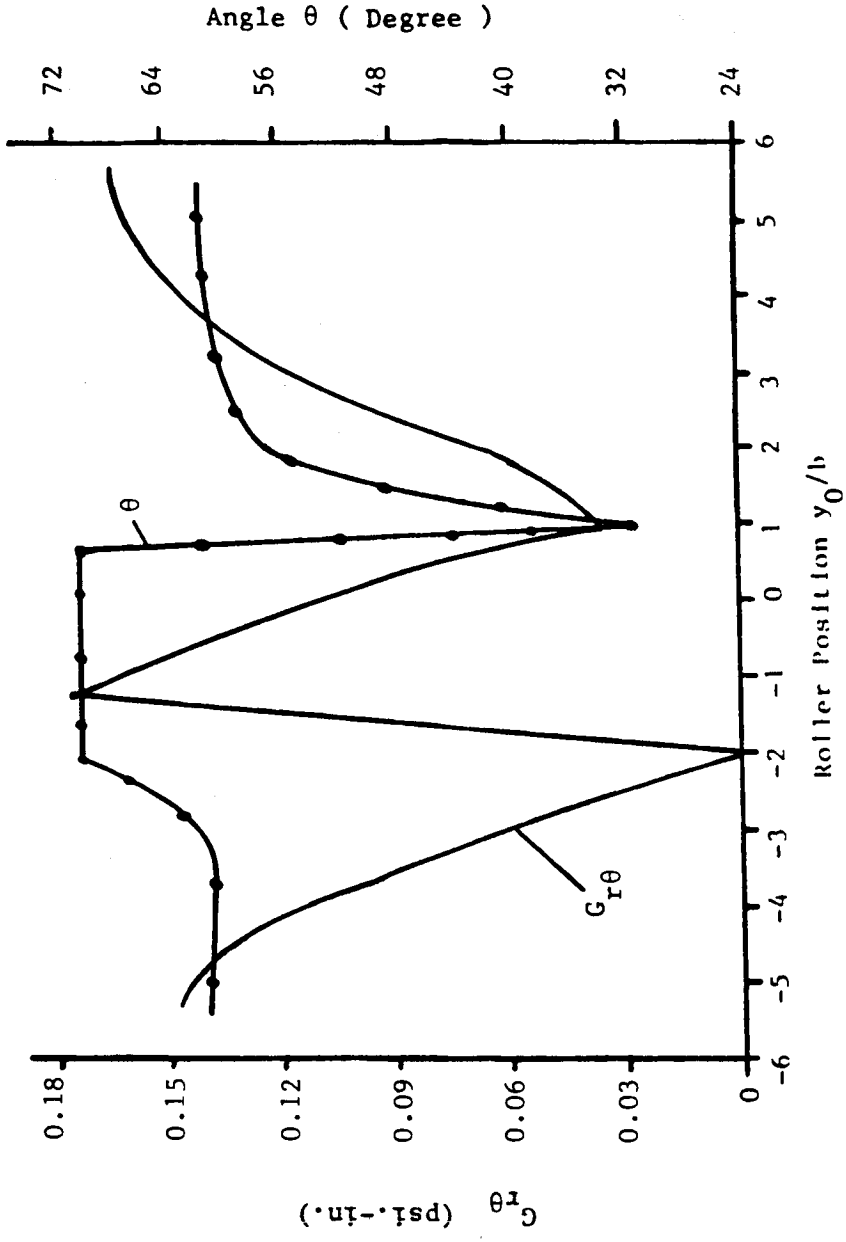

Fig. 5.26 Variation of the Maximum Shear Crack Extension Forces and the Angle they act on as a Function of Roller Position, (a_1=0.004in., a_2=0.002in., $\theta_2 = 71^0$, P=1500 lbs.)

Table 5.5 summarizes the loading conditions and crack geometries for the kinked crack for different Hertzian loads. The new crack increment was extended in the direction of the maximum change in the tangential crack extension forces, $\Delta G_{\theta\theta}$. Three different crack increments were used,(i.e. a_2 = 0.001 in., 0.002 in. and 0.003 in.), to determine if the crack increment length will affect the direction of crack propagation. Figs. 5.25 and 5.26 show the variations of the crack extension forces as a function of roller position for a Hertzian load of 1,500 lbs. and a kinked ligament of 0.002in., for $G_{\theta\theta}$ and $G_{r\theta}$ respectively. When the roller is far from the crack line, the tangential crack extension force starts out around 0.6 psi-in., and decreases to zero when y_0/b reaches -2. Due to the high shear stresses, the value of $G_{\theta\theta}$ increases sharply to 0.24 psi-in. and then decreases to 0.11 psi-in and then increases back up to a value of 0.6 psi-in.

The direction of the maximum $G_{\theta\theta}$ starts at 19 degrees then decreases to 0 degrees. As soon as the roller is on the other side, y_0/b is greater than 0., the maximum $G_{\theta\theta}$ occurs almost in the original direction then starts to decrease back to 19 degrees.

The maximum changes in the crack extension forces and the angles they act on are shown in Table 5.5. All the changes of $G_{\theta\theta}$ are above $\Delta G_{\theta\theta\,th}$ of 0.49 psi-in. for M50 steel, indicating a tensile mode growth. As seen from the results the crack tries

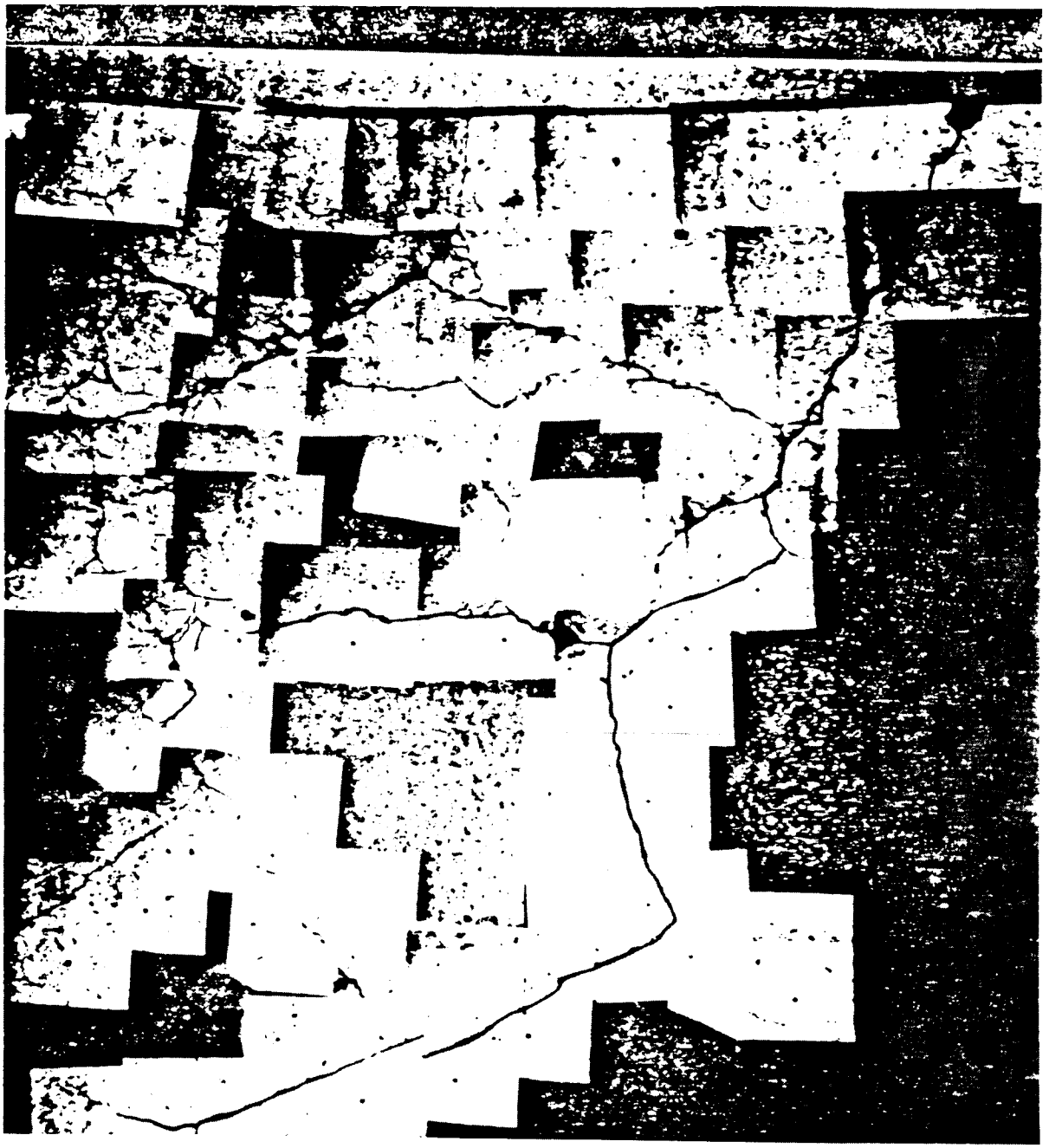

Fig. 5.27 Experimental Crack Profile, Ref. [51]

Table 5.6 Variation of the Direction of Crack Growth with Every Crack Extension Ligament, P=1,500lbs.

i	a_i	$\Delta G_{\theta\theta}$	θ_{i+1}
1	0.004	2.2626	71.
2	0.002	0.62055	19.
3	0.002	9.1371	65.
4	0.002	2.2293	14.
5	0.002	8.8994	45.

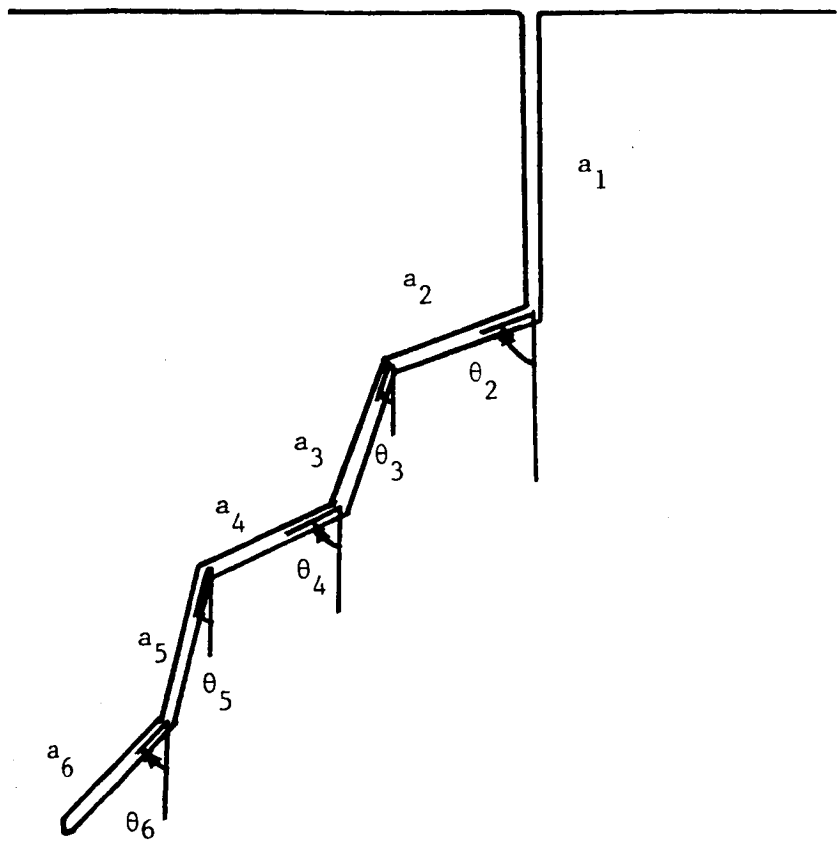

Fig. 5.28 Simulated Crack Growth Profile for a Roller Bearing with a Hertzian equal to 1500. lbs.

to realign itself in the original direction, going back halfway. If the crack is extend further (a_2 = 0.003in.), the angle of crack propagation return to zero. We can state that: as soon as the crack grows from the vertical direction along the maximum angle of $\Delta G_{\theta\theta}$, the loading cycle changes causing the crack to turn back to its original direction. This may explain the step like crack growth observed in the experiment of Bamberger at DN value of three million, see Fig. 5.26 from Ref. [51].

To simulate the experimental crack profile, the crack geometry was extended along the new maximum change of $G_{\theta\theta}$, for a constant ligament length, a_1 equal to 0.002 in. This constant ligament length is arbitrary.

Table 5.6 shows the values of the maximum change in $G_{\theta\theta}$ and the angles where they act on, measured from the vertical, assuming equal crack increments of 0.002 in. Fig. 5.27 is a plot of the crack profile from the boundary integral simulation. One can observe some similarity between the actual crack profile of Fig. 5.26 and the simulation in Fig. 5.27. Qualitatively, one can observe the step-like variation of crack orientation with crack depth.

The next step is to determine the time to failure of a small induced crack on the surface of the inner raceway of a high speed bearing, as will be discussed in the next section.

5.3 Time to Failure

The time to failure of the inner raceway is estimated using the experimental results on the crack propagation rate for M50 steel. Fig. 5.29 shows the crack growth rate as a function of the stress intensity factor range. The slope equals approximatly 3. The shape of the curve is similar to the last segment of the da/dN verus ΔK_I curve, or the last stage in the crack growth rate, (Fig. 1.4).

The time is estimated using Eq. 2.27 for tensile mode growth. The different contants, n_1 and c, for different values of n_2 are shown in Table 5.7, since no exact value of n_2 is available. The life is estimated at 25,500 RPM starting with an initial crack of 0.002 in. N is determined by integrating Eq. 2.27 with respect to da:

$$N = \int \frac{da}{f(\Delta G_{\theta\theta}, R)} \qquad 5.2$$

The function $f(\Delta G_{\theta\theta}, R)$ is approximated using least square of the values of $\Delta G_{\theta\theta}$ as function of crack length a from Fig. 5.19.

The variation of the crack length as function of the number of cycles is shown in Fig. 5.30. The main characteristic of the curve is the slow propagation phase for small crack length followed by rapid growth to failure.

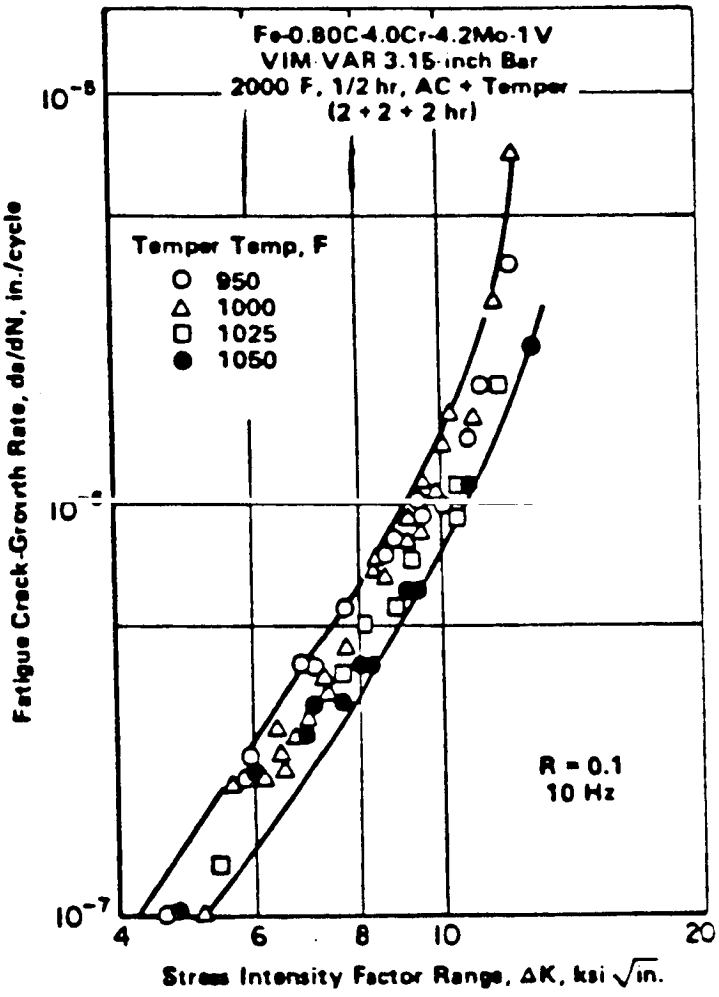

Fig. 5.29 Crack Propagation Rate as a Function of the Stress Intensity Factor Range for M50 Steel, Ref. [49]

Table 5.7 Constant used in Eq. 2.27 for M50 Steel

case	n_1	n_2	c
1	1.433	0.0	1.5×10^{-7}
2	0.82	0.5	8.4×10^{-7}
3	0.76	1.0	2.3×10^{-6}

The variations of the number of cycles necessary to propagate a crack to failure as a function of the applied Hertzian load are shown in Table 5.8 with and without friction along the crack faces. The effect of friction along the crack faces is to increase the life to failure due to the decrease of the change in the crack extension forces with an increase in the friction factor. Fig. 5.31 shows the Hertzian load versus number of cycles to failure for an original crack length of 0.002 in. The behavior of the curve, which shows an increase in life for decrease the Hertzian load on bearings, is similar to standardized S-N curves.

A direct comparison with the experimental fatigue life of bearings at DN value of three million was not possible since the crack growth rate data available are for M50 steel tempered once while the bearings actualy tested were tempered five times. It is well known that the crack growth rate changes with the number of temperings. The second variable that affected the comparison is the lack of crack growth rate data of the shear crack growth mode. For very small cracks, the crack driving force, as seen earlier, is the the shear crack extension force, ΔG_{r_θ}. Nevertheless, one can observe the very fast time to failure of the inner raceway which is in the order of 10 minutes for a original crack length of 0.002 in. with a Hertzian load of 1500 lbs. and a rotational speed of 25,500 RPM. This estimate is found assuming that the maximum loaded roller passes over the

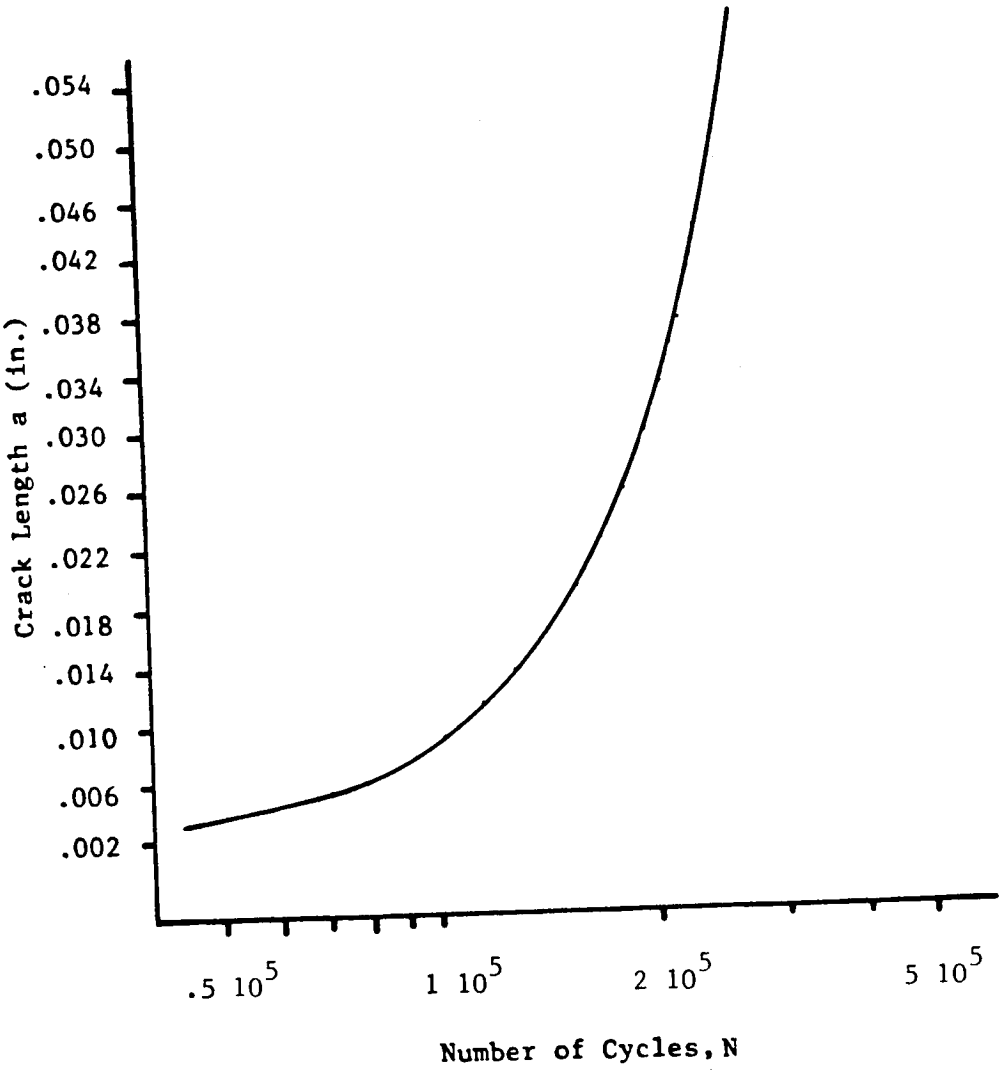

Fig. 5.30 Variation of Crack Length versus Number of Cycles, using Eq. 2.27 with $n_1 = 0.764$, $n_2 = 1.$ and $c = 2.2856 \times 10^{-6}$, for a Hertzian load of 1500 lbs.

Table 5.8 Number of Cycle to Failure for Different Hertzian loads and friction values, f, along the crack faces.

		P lbs.			
		500	1000	1500	2000
	case				
	1	0.946×10^5	0.500×10^5	0.296×10^5	0.199×10^5
f=0.0	2	0.796×10^5	0.475×10^5	0.287x105	0.176×10^5
	3	0.991×10^5	0.435×10^5	0.215×10^5	0.098×10^5
	1		0.509×10^5	0.306×10^5	0.208×10^5
f=0.05	2		0.482×10^5	0.295×10^5	0.177×10^5
	3		0.443×10^5	0.226×10^5	0.107×10^5
	1		0.518×10^5	0.318×10^5	0.220×10^5
f=0.1	2		0.490×10^5	0.304×10^5	0.187×10^5
	3		0.451×10^5	0.235×10^5	0.117×10^5

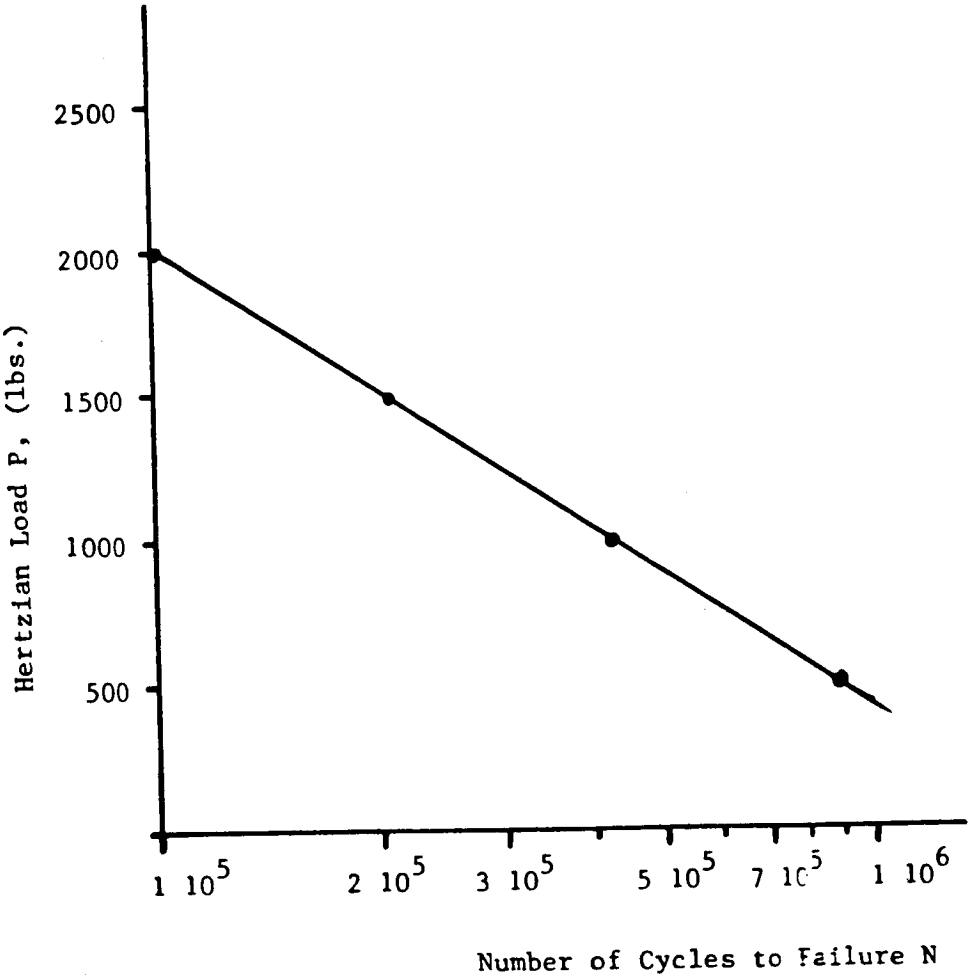

Fig. 5.31 Hertzian Load Versus Number of Cycles to Failure for M50 Steel Using Eq. 2.27 with $n_1 = 0.764$, $n_2 = 1.$ and $c = 2.2856 \times 10^{-6}$

crack only once every cycle. This results can explain the fast crack propagation of an induced surface crack on the inner raceway of bearing with a DN value of three million.

5.4 Conclusion

The main conclusion to be drawn from the preceeding analysis is that the alternating mixed-mode loading is the driving force behind the fast growing crack in high speed bearings. This alternating mixed-mode is due to the superposition of the Hertzian stress field onto the tangential stresses due to the rotation and press fit. The crack growth direction is shown to propagate in a step like fashion alternating between the vertical and an angle approaching 80 degrees as observed experimentally in Ref. [51].

The maximum change of the crack extension force components, $\Delta G_{\theta\theta}$ and $\Delta G_{r\theta}$ are good measures of the crack propagation driving forces and direction of crack growth.

The time to failure of a surface defect was determined to be very short, in the order of 10 minutes, which did not compare well with the experimental values of 2 hours for ball bearings.

Crack growth rate in the shear mode growth region, (region where $\Delta G_{r\theta}$ is dominant) should be available to better predict the fatigue life of the inner raceway and any other component under a general mixed-mode loading condition.

It should be emphasized that many simplifications were made in the present analysis. In particular the three-dimensional effects, thermal effects, residual stresses, dynamics, damage accumulation ahead of the crack tip, and finally the randomness inherent in the system, were not included. Although the results may not be the final answer to the fast failure of the inner raceway of high speed bearings at DN values above three million, some more understanding on the mechanism that leads to this new catastrophic failure was obtained.

CHAPTER SIX

CONCLUSIONS

6.1 Summary

The goal of this study was to analyze the causes that lead to the brittle failure of the inner raceway of high speed bearings. The analysis has shown the following conclusions:

- The critical crack length required for unstable crack growth is inversely proportional to the fourth power of DN.

- A mixed-mode fatigue crack growth is the cause that leads a small surface defect to propagate inward until reaching the critical crack length.

- The mixed-mode loading is associated with the interaction of the compressive normal stresses and the shear stresses with the passage of the Hertzian pressure, and is superimposed on the tensile stresses of the rotational speed and the press fit of the inner raceway onto the shaft.

- The maximum changes in the crack extension forces ($\Delta G_{\theta\theta}$, $\Delta G_{r\theta}$) are good measures of the mixed-mode fatigue driving forces.

- Improvement in the fatigue properties of the bearing materials are needed to increase the threshold values of the crack extension forces in shear as well as in tension, (increase the values of $\Delta G_{r\theta th}$, and $\Delta G_{\theta\theta th}$).

- For very small cracks the shear crack growth is the dominant crack extension driving force ($\Delta G_{r\theta}$).

- The crack was shown to grow in a step like fashion as observed experimentally.

- The effect of sliding friction is to make the crack grow in the direction opposite to the rolling direction.

- The effect of friction along the crack faces is to decrease the shear mode stress intensity factor in the presence of high compressive normal stresses.

- The time to failure was estimated to be very short in the order of 10 minutes.

6.2 Further work

- A three dimensional analysis for roller bearing as well as ball bearings should be considered.

- The effect of the lubricant should be considered in greater details with viscosity pressure and temperature variations.

- Residual stresses and material nonlinearity can be the cause of crack arrest and slower crack propagation rate as observed experimentally rather than the very fast growth measured from the elastic analysis.

- More understanding of the crack growth behavior in shear growth mode region, where $\Delta G_{r\theta}$ is dominant, is required.

- Dynamic effect with each passage of the roller should be considered.

- The randomness of the surfaces in contact and the loads and the material propreties should be incorporated in the analytical modelling.

REFERENCES

1. Tallian, T.E., "On Competing Failure Modes in Rolling Contact," ASLE Transactions, vol. 10, (1967), pp. 418-439.

2. Way, S., "Pitting Due to Rolling Contact," Journal of Applied Mechanics, Transaction of ASME, vol. 2, (1935), pp. A49-A58.

3. Fleming, J.R. and Suh, N.P., "Mechanics of Crack Propagation in Delamination Wear," Wear, vol. 44, (1977), pp. 39-56.

4. Rosenfield, A.R., "A fracture Mechanics Approach to Wear," Wear, vol. 61, (1980), pp. 125-132.

5. Keer, L.M., Bryant, M.D. and Haritos, G.H., "Subsurface and Surface Cracking Due to Hertzian Contact," Journal of Lubrication Technology, vol. 104, (1982), pp. 347-351.

6. Keer, L.M. and Bryant, M.D., "A Pitting Model for Rolling Contact Fatigue," Journal of Lubrication Technology, vol. 105, (1983), pp. 198-205.

7. Miller, G.R., Keer, L.M. and Cheng, H.S., "On the Mechanics of Fatigue Crack Growth Due to Contact Loading," Proc. R. Soc. Lond., vol. A397, (1985), pp. 197-209.

8. Murakami, Y., Kaneta, M. and Yatsuzuka, H., "Analysis of Surface Crack Propagation in Lubricated Rolling Contact," ASLE Transactions, vol. 28, (1985), pp. 60-68.

9. Clark, J.C., "Fracture Failure Modes in Light Weight Bearings," J. Aircraft, vol. 12, (1975), pp. 383-387.

10. Bamberger, E.N., Zaretsky, E.V. and Signer, H., "Endurance and Failure Charteristic of Main-Shaft Jet Engine Bearing at 3×10^6 D.N.," Journal of Lubrication Technology, vol. 98, (1976), pp. 580-585.

11. Sih, G.C. and Barthelemy, B.M., "Mixed Mode Fatigue Crack Growth Predictions," Engineering Fracture Mechanics, vol. 13, (1980), pp. 439-451.

12. Fisher, K.F., "Review of Brittle Fracture Criteria in Case of Static and Cyclic Mixed Mode Loading," Theoretical and Applied Fracture Mechanics, vol. 1, (1984), pp. 117-131.

13. Forman, R.G., Kearney, V.E. and Engle, R.M., "Numerical Analysis of Crack Propagation in Cyclic Loaded Structures," Journal of Basic Engineering, vol. 89, (1967), pp. 885.

14. Lawn, B.R. and Wilson, T.R., Fracture of Brittle Solids, Cambridge University Press, 1975.

15. Hussain, M.A., Pu, S.l. and Underwood, J., "Strain Energy Release Rate for a Crack Under Combined Mode I and Mode II," Fracture Analysis, ASTM STP 560, American Society for Testing and Materials, (1974), pp. 2-28.

16. Wu, C.-H., "Fracture Under Combined Loads by Maximum-Energy-Release-Rate Criterion," Journal of Applied Mechanics, vol. 45, (1978), pp. 553-558.

17. Hayashi, K. and Nemat-Nasser, S., "Energy Release Rate and Crack Kinking," Int. J. Solids Structure, vol. 17, (1981), pp. 107-114.

18. Erdogan, F. and Sih, G.C., "On the Crack Extension in Plates Under Plane Loading and Transverse Shear," Journal of Basic Engineering, vol. 85, (1963), pp. 519-527.

19. Otsuka, A., Mori, K. and Miyata, T., "The Condition of Fatigue Crack Growth in Mixed Mode Condition, Engineering Fracture Mechanics, vol. 7, (1975), pp. 429-439.

20. Budiansky, B. and Rice, J.R., "Conservation Laws and Energy-Release Rates," Trans. ASME, J. Appl. Mech., vol. 40., (1973), pp. 201-203.

21. Knowles, J.K. and Sternberg, E., "On a Class of Conservation Laws in Linearized and Finite Elastostatic," Arch. For Rational Mechanics and Analysis, vol. 44, (1972), pp. 187-211.

22. Bui, H.D., "Associated Path Independent J-Integrals for Separating Mixed Modes," J. Mech. Phys. Solids, vol. 31, (1983), pp. 439-448.

23. Sih, G.C., "Strain-Energy-density Factor Applied to Mixed Mode Crack Problem," International Journal of Fracture, vol. 10, No. 3, (1974), pp. 305-321.

24. Strifors, H.C., "A Generalized Force measure of conditions at crack tip," International Journal Of Solids and Structures, vol. 10, (1974), pp. 1389-1404.

25. Goldstein, R.V. and Salganik, R.L., "Brittle Fracture of Solids With Arbitrary Cracks," Int. J. Fract., vol. 10, (1974), pp. 507-523.

26. Broek, D., Elementary Engineering Fracture Mechanics, The Hague, 1982.

27. Fischer, K.-F., "review of Brittle Fracture Criteria in Case of Static and Cyclic Mixed Mode Loadings," Theoretical and Applied Fracture Mechanics, vol. 1, (1984), pp.117-131.

28. Paris, P.C. and Erdogan, F., "A Critical Analysis of Crack Propagation Laws," Journal of Basic Engineering, vol. 85, (1963), pp. 528-534.

29. Roberts, R. and Erdogan, F., "The Effect of Mean Stress in Plates under Extension and Bending," Journal of Basic Engineering, vol. 89, (1967), pp. 885-891.

30. Pook, L.P., "A Failure Mechanism Map For Mixed Mode I and II Fatigue Crack Growth Threshold," International Journal of Fracture, vol. 28, (1985), pp. R21-R23.

31. Rizzo, F.J., "An Integral Equation Approach to Boundary Value Problems of Classical Elastostatics," Quarterly of Applied Mathematics, vol. 25, (1967), pp. 83-95.

32. Mendelson, A., "Boundary-Integral Methods in Elasticity and Plasticity," NASA TNO-7418, National Aeronautics and Space Administration, Washington, D.C., November, 1973.

33. Banerjee, P.K. and Butterfield, R., Boundary Element Methods in Engineering Science, McGraw-Hill, London, 1981.

34. Ghosn, L.J., "Three-Dimensional Analysis of Chevron-Notched Specimens by Boundary Integral Method," M.S. Thesis, Case Western Reserve University, Aug. 1983.

35. Sokolinikoff, I.S., Mathematical Theory of Elasticity, McGraw-Hill, New York, 1956.

36. Love, A.E.H., A Treatise on the Mathematical Theory of Elasticity, Dover, New York, 1944.

37. Cook, R., Concepts and Applications of Finite Element Analysis, John Wiley and Sons, New York, 1974.

38. Cruse, T.A., "An Improved Boundary-Integral Equation Method for Three Dimensional Elastic Stress Analysis," Computers and Structures, vol. 4, (1974), pp. 741-754.

39. Blandford, G.E., Ingraffea, A.R., and Liggett, J.A., "Two-Dimensional Stress Intensity Factor Computations Using The Boundary Element Method," International Journal for Numerical Methods in Engineering, vol. 17, (1981), pp. 387-404.

40. Tada, H., Paris, P.C., and Irwin, G.R., The Stress Analysis of Cracks Handbook, DEL Research Corporation, Hellertown, Pennsylvania, 1973.

41. Saada, A.S., Elasticity Theory and Applications, Krieger Publishing Company, Malabar, Florida, 1983.

42. Private Communications with Dr. R. Parker At NASA Lewis Research Center.

43. Hertz, H., "Uber Die Beruhrung Fester Elastischer Korper," (On the Contact of Elastic Solids), J. Reine Und Angewandte Mathematik, vol. 92, (1882), pp. 156-171.

44. Smith, J.O. and Liu, G.-K., "Stresses Due to Tangential and Normal Loads on an Elastic Solid with Application to Some Contact Stress Problems," Journal of Applied Mechanics, vol. 20, no. 2, 1953, pp. 157-166.

45. Hamrock, B.J. "Lubrication of Machine Elements," NASA Reference Publication 1126, August, 1984.

46. Hamrock, B.J. and Tripp, J.H., "Numerical Methods and Computers Used in Elastohydrodynamic Lubrication," NASA Technical Memorandum 83524, 1983.

47. Shieh, W.T., "Compessive Maximum Shear Crack Initiation and Propagation," Eng. Fracture Mechanics, vol. 9, (1977), pp. 37-54.

48. Swedlow, J.L., "Criteria for Growth of the Angled Crack," In Cracks and Fracture, ASTM STP 601, American Society For Testing and Materials, 1976, pp.506-521.

49. Rescalvo, J.A. and Averbach, B.L., "Fracture and Fatigue in M-50 and 18-4-1 High speed Steels," A.S.M. Metallurgical Transaction, vol. 10, (1979), pp. 1265-1271.

50. Yamamoto, T., "Crack Growth in Lubricated Rollers," In Solid Contact and Lubrication, AMD vol 39, The Winter Annual Meeting of the American Society of Mechanical Engineers, Chicago, Illinois, November 16-21, 1980.

51. Bamberger, E.N., Averbach, B.L., and Pearson, P.K., "Impoved Fracture Toughness Bearings," AFWAL-TR-84-2103, Air Force Wright Aeronautical Laboratories, January, 1985.

52. Buzzard, R.J., Gross, B., and Srawley, J.E., "Mode II Fatigue Crack Growth Specimen Development," Presented at The Seventeenth National Symposium on Fracture Mechanics, ASTM Committee E-24, 7-9 August, 1984, Albany, New York.

APPENDIX A

Derivation of the Singular Integral

Because of the singular nature of Kelvin's solution a cut is made in the body to exclude the point P from the region (where U_{ij} and $T_{ij} \rightarrow \infty$), in a Cauchy sense.

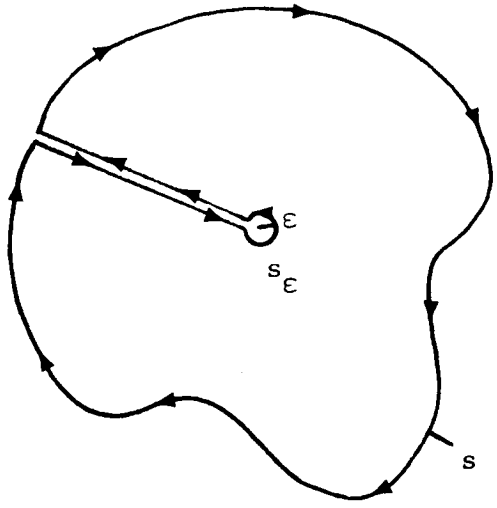

The line integral going from the surface boundary to the singularity point P is cancelled by the integral coming back since it can be considered that the same path is being integrated over but in opposite direction, therefore Eq. 3.7 will be:

$$\int_s t_j \, U_{ij} \, ds + \int_{s_\varepsilon} t_j \, U_{ij} \, ds_\varepsilon = \int_s u_j \, T_{ij} \, ds + \int_{s_\varepsilon} u_j \, T_{ij} \, ds_\varepsilon \qquad \text{A.1}$$

where s is the boundary surface of the body and s_ε is the a circle centered at the singularity point P of radius ε.

Considering the value of the integral at point P as the radius of s_ε goes to zero ($\varepsilon \to 0$), and noting that :

$$ds_\varepsilon = \varepsilon \, d\theta$$

$$r_{,i} = n_i$$

$$n_1 = -\cos\theta$$

$$n_2 = -\sin\theta$$

$$dr/dn = \cos\theta \; n_1 + \sin\theta \; n_2 = -1$$

$$r_{,i} \, n_j - r_{,j} \, n_i = 0$$

$$\varepsilon \ln\varepsilon \to 0 \qquad \text{if } \varepsilon \to 0$$

The values of the integrals around s_ε can be evaluated as follows:

Substituting the value of U_{ij} from Eq. 3.2

$$\int_{s_\varepsilon} t_j \, U_{ij} \, ds_\varepsilon = \int_0^\theta \frac{-1}{8\pi G(1-\nu)} \left\{ (3-4\nu)\ln\varepsilon \; \delta_{ij} - n_i n_j \right\} t_j \, \varepsilon \, d\theta \qquad \text{A.2}$$

Placing ε outside the integral:

$$= \frac{-1}{8\pi G(1-\nu)} \left\{ \varepsilon\ln\varepsilon \int_0^\theta \delta_{ij} \, t_j \, d\theta - \varepsilon \int_0^\theta n_i n_j \, t_j \, d\theta \right\} \qquad \text{A.3}$$

and taking the limit as $\varepsilon \to 0$,

$$\int_{s_\varepsilon} t_j \, U_{ij} \, ds_\varepsilon = 0 \qquad \text{A.4}$$

By substituting Eq. 3.6 for T_{ij}, the second integral becomes:

$$\int_{s_\varepsilon} u_j \, T_{ij} \, ds_\varepsilon = \int_0^\theta \frac{(1-2\nu)}{\varepsilon \, 4\pi(1-\nu)} \left\{ \delta_{ij} + \frac{2}{(1-2\nu)} \, n_i n_j \right\} \varepsilon \, d\theta \qquad \text{A.5}$$

$$= \frac{(1-2\nu)}{4\pi(1-\nu)} \int_0^\theta \left\{ \delta_{ij} + \frac{2}{(1-2\nu)} \, n_i n_j \right\} d\theta$$

Evaluating the function in matrix form:

$$= \frac{(1-2\nu)}{4\pi(1-\nu)} \begin{bmatrix} \int_0^\theta 1 + \frac{2}{(1-2\nu)} \cos^2\theta \; d\theta & \int_0^\theta - \frac{2}{(1-2\nu)} \sin\theta \cos\theta \; d\theta \\ \int_0^\theta - \frac{2}{(1-2\nu)} \sin\theta \cos\theta \; d\theta & \int_0^\theta 1 + \frac{2}{(1-2\nu)} \sin^2\theta \; d\theta \end{bmatrix} \qquad \text{A.6}$$

Integrating each term of the matrix, the above equation

$$= \frac{1}{4\pi(1-\nu)} \begin{bmatrix} 2\theta(1-\nu)+\sin\theta\cos\theta & -\sin^2\theta \\ -\sin^2\theta & 2\theta(1-\nu)-\sin\theta\cos\theta \end{bmatrix} \qquad \text{A.7}$$

By substituting relations A.4 and A.7 in Eq. A.1 one gets the boundary integral equations :

$$\int_s t_j \, U_{ij} \, ds = \int_s u_j \, T_{ij} \, ds + \qquad \text{A.8}$$

$$\frac{u_j}{\pi} \begin{bmatrix} \frac{\theta}{2} + \frac{\sin\theta\cos\theta}{4(1-\nu)} & -\frac{\sin^2\theta}{4(1-\nu)} \\ -\frac{\sin^2\theta}{4(1-\nu)} & \frac{\theta}{2} - \frac{\sin\theta\cos\theta}{4(1-\nu)} \end{bmatrix}$$

If the point P is at the interior of the body, θ will be equal to 2π, if P is a point at a smooth surface, θ will be equal to π. The integral equation will have the following general form:

$$C_{ij}\, u_j + \int_S u_j\, T_{ij}\, ds = \int_S t_j\, U_{ij}\, ds \qquad \text{A.9}$$

where

$$C_{ij} = \begin{bmatrix} \frac{\theta}{2\pi} + \frac{\sin\theta\cos\theta}{4\pi\,(1-\nu)} & \frac{-\sin^2\theta}{4\pi\,(1-\nu)} \\ \frac{-\sin^2\theta}{4\pi\,(1-\nu)} & \frac{\theta}{2\pi} - \frac{\sin\theta\cos\theta}{4\pi\,(1-\nu)} \end{bmatrix} \qquad \text{A.10}$$

where $C_{ij} = \delta_{ij}$ for internal points, and $C_{ij} = 1/2\ \delta_{ij}$ for surface points, with smooth boundary.

1. Report No.	2. Government Accession No.	3. Recipient's Catalog No.
NASA CR-179518		

4. Title and Subtitle	5. Report Date
Analysis of Mixed-Mode Crack Propagation Using the Boundary Integral Method	September 1986
	6. Performing Organization Code

7. Author(s)	8. Performing Organization Report No.
Alexander Mendelson and Louis J. Ghosn	None
	10. Work Unit No. 505-83-11

9. Performing Organization Name and Address	11. Contract or Grant No.
Case Western Reserve University Department of Civil Engineering Cleveland, Ohio 44106	NAG3-396
	13. Type of Report and Period Covered Contractor Report Final

12. Sponsoring Agency Name and Address	14. Sponsoring Agency Code
National Aeronautics and Space Administration Washington, D.C. 20546	

15. Supplementary Notes

Project Manger, John L. Shannon, Jr., Structures Division, NASA Lewis Research Center.

16. Abstract

Crack propagation in a rotating inner raceway of a high speed roller bearing is analyzed using the boundary integral equation method. The model consists of an edge crack in a plate under tension, upon which varying Hertzian stress fields are superimposed. A computer program for the boundary integral equation method was written using quadratic elements to determine the stress and displacement fields for discrete roller positions. Mode I and Mode II stress intensity factors and crack extension forces $G_{\theta\theta}$ (energy release rate due to tensile opening mode) and $G_{r\theta}$ (energy release rate due to shear displacement mode) were computed. These calculations permit determination of that crack growth angle for which the change in the crack extension forces is maximum. The crack driving force was found to be the alternating mixed-mode loading that occurs with each passage of the most heavily loaded roller. This alternating mixed-mode loading is due to the superposition of the Hertzian stress fields on the tangential stresses due to rotation and press fit. The crack is predicted to propagate in a step-like fashion alternating between radial and inclined segments, and this pattern was observed experimentally. The maximum changes $\Delta G_{\theta\theta}$ and $\Delta G_{r\theta}$ of the crack extension forces are found to be good measures of the crack propagation rate and direction. The time-to-failure of the inner raceway of the high speed bearing was estimated to be very short for a DN value of three million, where D is the bearing bore diameter in mm and N is the speed in RPM. The predicted short lifetime was confirmed by limited testing of a ball bearing of similar load capabilities. A modified Forman type crack propagation law as a function of the crack extension forces was used in calculating the time-to-failure.

17. Key Words (Suggested by Author(s))	18. Distribution Statement
Hertz stresses; Contact stresses; Mixed mode; Stress intensity factors; Fracture mechanics; Crack stress fields; Aircraft engine bearings	Unclassified - unlimited STAR Category 39

19. Security Classif. (of this report)	20. Security Classif. (of this page)	21. No. of pages	22. Price*
Unclassified	Unclassified	192	A09

*For sale by the National Technical Information Service, Springfield, Virginia 22161